EDTA Functionalized Fe-Mn Binary Oxide/Hydrochar from Green Tea Waste Composite

Septian Perwira Yudha

A Thesis Submitted in Partial Fulfillment of the Requirements for the

Degree of Master of Science in Chemistry

(International Program)

Prince of Songkla University

2019

Copyright of Prince of Songkla University

EDTA Functionalized Fe-Mn Binary Oxide/Hydrochar from Green Tea Waste Composite

Septian Perwira Yudha

A Thesis Submitted in Partial Fulfillment of the Requirements for the

Degree of Master of Science in Chemistry

(International Program)

Prince of Songkla University

2019

Copyright of Prince of Songkla University

Thesis Title	EDTA Functionalized Fe-Mn Binary Oxide/Hydrochar from Green Tea Waste Composite
Author	Mr. Septian Perwira Yudha
Major Program	Chemistry (International Program)

Major Advisor

.....
(Asst. Prof. Dr.Surajit Tekasakul)

Co-advisor

.....
(Dr.Khamphe Phoungthong)

Examining Committee:

.....Chairperson
(Asst. Prof. Dr.Cheewita Suwanchawalit)

.....Committee
(Dr.Laemthong Chuenchom)

.....Committee
(Assoc. Prof. Dr.Pongsaton Amornpitoksuk)

.....Committee
(Asst. Prof. Dr.Surajit Tekasakul)

.....Committee
(Dr.Khamphe Phoungthong)

The Graduate School, Prince of Songkla University, has approved this thesis as partial fulfillment of the requirements for the Master of Science Degree in Chemistry (International Program).

.....
(Prof. Dr. Damrongsak Faroongsarng)
Dean of Graduate School

This is to certify that the work here submitted is the result of the candidate's own investigations. Due acknowledgement has been made of any assistance received.

.....Signature
(Asst. Prof. Dr. Surajit Tekasakul)
Major Advisor

.....Signature
(Dr. Khamphe Phoungthong)
Co-advisor

.....Signature
(Mr. Septian Perwira Yudha)
Candidate

I hereby certify that this work has not been accepted in substance for any degree, and is not being currently submitted in candidature for any degree.

.....Signature
(Mr. Septian Perwira Yudha)
Candidate

Thesis Title	EDTA Functionalized Fe-Mn Binary Oxide/Hydrochar from Green Tea Waste Composite
Author	Mr. Septian Perwira Yudha
Major Program	Chemistry (International Program)
Academic Year	2018

ABSTRACT

In this study, a novel ethylenediaminetetraacetic acid (EDTA) functionalized hydrochar from green tea (*Camellia sinensis*) waste, doped with manganese ferrite, was synthesized by hydrothermal carbonization (HTC) coupled with the activation process. This adsorbent was applied to remove Rhodamine B (RhB) and copper ions (Cu^{2+}) from aqueous solutions. The characterization of adsorbent was carried out using Field Emission Scanning Electron Microscopy-Electron Dispersive X-ray Spectroscopy, CHNO analyzer, BET gas sorption analyzer, X-ray Diffraction, Zeta Potential Analyzer, Vibrating Sample Magnetometer, Fourier Transform Infrared Spectroscopy and X-ray Photoelectron Spectroscopy. Some parameters such as adsorbent weight, contact time and initial concentration, temperature and pH were investigated in the adsorption experiment. The Langmuir isotherm and pseudo-second-order kinetic model fitted well with the obtained data with the maximum adsorption capacities (q_{max}) for RhB and copper ions (Cu^{2+}) of 21.41 and 9.49 $mg.g^{-1}$ at natural pH, respectively. The adsorption mechanism of RhB and copper ions (Cu^{2+}) were facilitated *via* hydrogen bonding and the complexation process between the adsorbates and the adsorbent surface, respectively Furthermore, the regeneration studies of EDTA FMHC-700 exhibits a good reusability, high stability and fast separation within 4 successive cycles. The use of EDTA-FMHC-700 as a low-cost adsorbent with good separation performance can be developed for industrial applications and environmental remediation.

Keywords: EDTA, Manganese ferrite, Green tea waste, Adsorption, Hydrothermal carbonization

ACKNOWLEDGEMENT

I would like to grateful to my god, Allah, from my deepest heart for His blessing and mercy so that I can finish my study master's Degree program in Thailand. I also would like express my sincere guidance to my advisor, Asst. Prof. Dr. Surajit Tekasakul, for her guidance, kindness, encourage and support during my research. I would like to express my special gratitude to my co-advisor, Dr. Khamphe Phoungthong, for his valuable advice and guidance to study. I would like also to express my special gratefulness to Dr. Laemthong Chuenchom, for his encourage, motivation and valuable advice during my research.

I would like to thank to chairperson of the thesis examination, Asst. Prof. Dr. Cheewita Suwanchawalit, for her comments and correction of this thesis. I am also grateful to members of committee, Dr. Khamphe Phoungthong, Dr. Laemthong Chuenchom and Assoc. Prof. Dr. Pongsaton Amornpitoksuk for their valuable comments and recommendations for my thesis.

I would like to express my thanks to the Department of Chemistry staff, Faculty of Science staff and especially members of laboratory of Ch 316 and Ch 314 for their help during my study.

I would like to express my thanks to Graduate School, Prince of Songkla University for the financial support during my study in Master Degree program through The Higher Education Research Promotion and The Thailand's Education Hub for Southern Region of ASEAN Countries Project Office of The Higher Education Commission scholarship. This research was also supported by PSU Graduate School Financial Support.

Finally, my greatest thanks for my beloved father and mother, my fiancé and all my family for their support and encouragement to finish my study. Their strong love strengthened me to complete my study.

Septian Perwira Yudha

CONTENTS

CONTENTS (Continued)

LIST OF FIGURES

LIST OF FIGURES (Continued)

LIST OF TABLES

CHAPTER 1

INTRODUCTION

1.1 General Introduction

Currently, many studies that pay attention to the process of dye removal in industrial waste because it is very dangerous and toxic. The dye can be toxic, carcinogenic or mutagenic to human and destruct the aquatic life with enhanced biochemical oxygen demand (Attallah et al., 2016). Among the various dyes, Rhodamine B (RhB) is a positively charged dye and water-soluble (amphoteric). This dye is widely used in the printing, dyeing, textile, leather, wood, silk, fiber, soap, toothpaste and lipstick industries (Das et al., 2018). When compared to other organic compounds, the size of the Rhodamine B molecule (1.44 nm) is much larger than the size of the phenol molecule (0.58 nm) (Jiang and Huang, 2016). Water systems contaminated with Rhodamine B can be detrimental to living things such as causing eye and skin irritation, gastrointestinal disorders, thyroid and liver damage, neurotoxic, carcinogens, mutagens to death (Khamparia and Jaspal, 2017). It is known that Rhodamine B (RhB) with LC50 of 83.9 $mg.L^{-1}$ can kill a large population of *Cyprinodon variegatus* (sheepshead minnow) (Kooh et al., 2016). Therefore, it is very important to remove this dye from wastewater before disposal into the environment.

In addition, the presence of pharmaceutical compounds in the aquatic environment such as the class of non-steroidal anti-inflammatory drugs (NSAIDs) is the focus of several research because it can cause very adverse effects on humans and the environment even in low concentrations such as reduction of human embryos, gram-positive bacteria inhibition, as well as malfunction in fish organs (Essandoh et al., 2015). One of the non-steroidal anti-inflammatory drug found in many wastewater is 2-[3-(2-methylpropyl)phenyl] propanoic acid, or known as ibuprofen. In some developed countries in Europe has been detected the presence of ibuprofen in the wastewater with concentrations of 60-3400 $ng.L^{-1}$, of course this could potentially a danger to human. Water can be contaminated by ibuprofen obtained from

pharmaceutical industrial waste as well as human or animal who are given medical treatment, because the metabolism of these compound only partial in the body and its presence is secreted in the form of urine and feces (Dubey et al., 2010, Iovino et al., 2015). Failure of conventional wastewater treatment methods, lead to the discovery of appropriate and effective wastewater treatment methods to solve this problem.

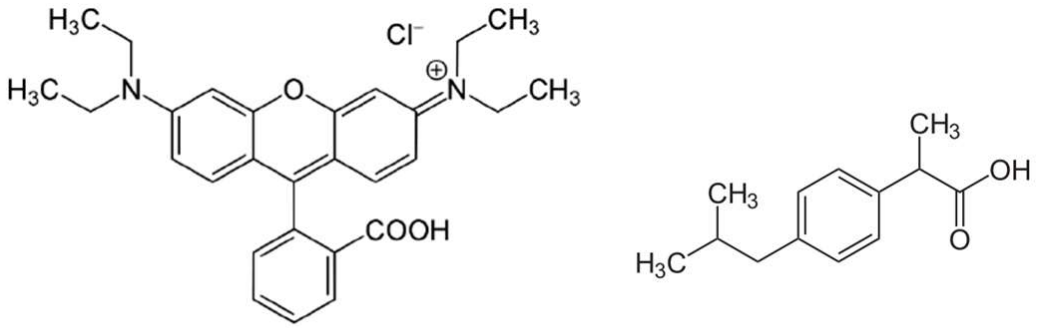

Fig. 1.1 (a) Chemical structure of Rhodamine B and (b) ibuprofen (Lin et al., 2017, Wang et al., 2017).

The presence of heavy metals in drinking water or industrial waste greatly threaten human health and the environment when the concentration of metals exceed the permitted level. One example of heavy metals which is highly toxic and carcinogenic is copper ion (Cu^{2+}) (Inyang et al., 2012, Mahmoud et al., 2018, Regmi et al., 2012). Indiscriminate industrial waste disposal is the largest source of contamination of Cu^{2+} in the environment. Contaminated wastewater by copper metal is usually obtained from electroplating and jewelry industry (Koottatep et al., 2017). In the human body, Cu^{2+} plays a role in enzymatic reactions, development of bone and nerve tissue. However, excessive concentration can lead to respiratory problems, abdominal pain, kidney failure, liver, to mutagenesis (Semerciöz et al., 2017). Also known that contamination of Cu^{2+} cause damage to soil biota and plants endemic Australia (*Acacia holosericea* and *Eucalyptus crebra*). The maximum level of Cu^{2+} in drinking water has set by the US Environmental Protection Agency (EPA) is less than 1.3 $mg.L^{-1}$ (Bilal et al., 2013). Therefore, it is necessary to find a cheap, easy and

effective method that can be applied to solve environmental problems related to contamination from dyes, pharmaceutical and heavy metal waste such as Rhodamine B, Ibuprofen and copper (Cu^{2+}).

The adsorption method has been used to overcome contamination caused by organic or inorganic contaminants. The advantages of this method is cheap, simple, high selectivity and environmental friendly. Lately, many of the adsorbent development from cheap materials based on activated carbon such as green tea waste (Ahmaruzzaman and Gayatri, 2010). Green Tea (*Camellia sinensis*) is one of the favorite drinks consumed throughout the world where its production through the drying process of the tea leaves. This tea plant originating from Southeast Asia that belong to the genus *Camelia* family *Theaceae*. Increased consumption of tea is accompanied by increased production of tea waste as a by-product, which feared would be an environmental problem later. The green tea waste contains about 93% organic matter (cellulose, hemicellulose, tannin, lignin and phenolic) and about 7% inorganic material (Mahmood et al., 2017, Weng et al., 2013). Therefore, it still needs a process to convert green tea waste into more useful products. One way that can be done is to convert green tea waste into hydrochar (carbon) through hydrothermal carbonization process which will be used as an adsorbent (Indolean et al., 2017). It can increase the economic value and the prospective of tea waste as the raw material of the adsorbent.

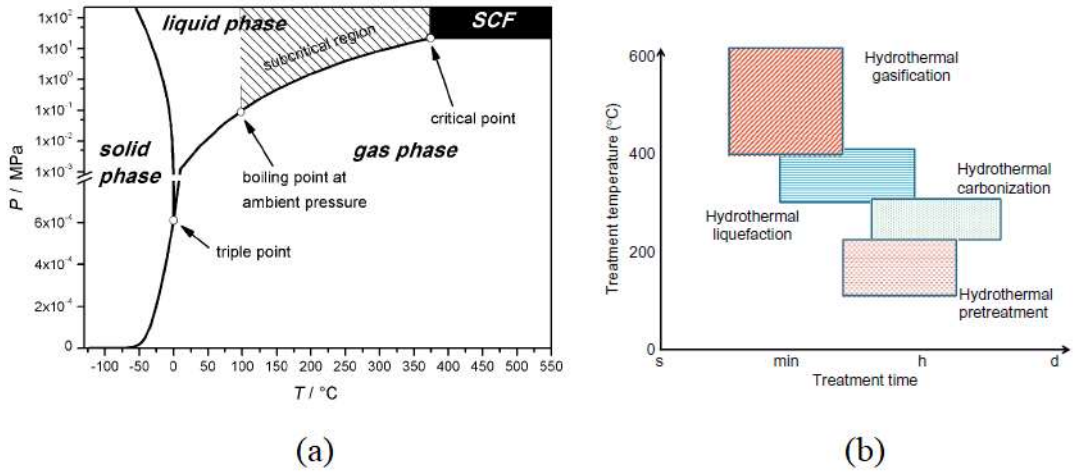

Fig. 1.2 (a) Phase diagram for the change in water properties at different temperatures, including sub- and super-critical regions and (b) effect of time and temperature on various hydrothermal processes (Matsumura, 2015, Möller et al., 2011).

The hydrothermal carbonization process is the conversion of biomass waste into carbon materials (hydrochar) as well as alternative fuels using high pressure and subcritical temperature of water (Elaigwu et al., 2014). This can happen because the biomass waste contains of carbohydrate derivatives such as cellulose or hemicellulose which undergo hydrolysis, condensation, dehydration, decarboxylation, polymerization and aromatization processes. The decomposition process of hemicellulose, cellulose and lignin occurs at temperatures of 200-300ºC, 300-400ºC and 600ºC, respectively (Kambo and Dutta, 2015). Moreover, the criteria of biomass waste that can be converted to hydrocarbons are non-toxic, low emissions and abundant (Lei et al., 2016). Biomass waste can be used in raw material form (Burca et al., 2016) as well as after chemically or physically modified (Mahmood et al., 2017, Yang et al., 2016).

In recent years, some studies have used binary oxide nanomaterial as an adsorbent such as ferromanganese (Fe-Mn) (Hou et al., 2010). One type of ferromanganese is manganese ferrite ($MnFe_2O_4$) where its application are used in water treatment (Yang et al., 2018a, Zhu et al., 2015), catalysis and degradation processes (Mishra et al., 2016, Nawaz et al., 2016). Lately, the functionalization of magnetic nanoparticle-based adsorbents by inorganic species as well as organic is more desirable because it can improve the adsorption capacity and stability of these nanoparticles

especially in acidic environments (Keyvani et al., 2018). Ethylenediaminetetraacetic acid (EDTA) is an inorganic compound containing two amino acid groups and four carboxylic acid groups which can act as chelating agent, oxidation inhibitor and stabilizer for metal ions (Aeenjan and Javanbakht, 2018, Liu et al., 2016, Lv et al., 2018, Zhao et al., 2017). Aside as an active sites provider with the abundant of amino-functional groups, EDTA is also used to avoid the agglomeration of nanoparticles on magnetic nanoparticle-based adsorbents during the solvothermal process (Liu et al., 2017).

In this work, the functionalization of EDTA on the adsorbent is synthesized by the facile hydrothermal carbonization combined with the activation process, then innovatively used to remove Rhodamine B, copper ion (Cu^{2+}) and ibuprofen from aqueous solution where as far as we know never reported before. Several factors that may affect to the adsorption process such as initial concentration and contact time, adsorbent weight, solution pH and temperature will be used to study the kinetic and isotherm of adsorption. Furthermore, the reusability of the adsorbent is studied through several successive cycle the adsorption-desorption processes.

1.2 Preliminary Knowledge and Theoretical Section

1.2.1 Activated Carbon

Activated carbon is defined by carbonaceous materials with graphite-like structure produced from a heating process at high temperatures which has physical properties such as a large surface area in excess of 2500 m^2/g with a very regular and well-developed microcrystalline structure (Smisek and Cerny, 1970). Large surface areas are usually produced through a chemical activation process that can increase the adsorption ability of the material. The production of activated carbon from various raw materials such as coffee shell (Sun et al., 2019), coconut shell (Freitas et al., 2019), corn cob (Nethaji et al., 2013) and rice husk (Pedroso et al., 2019) has been used as an adsorbent applied to the industrial sector and environmental remediation.

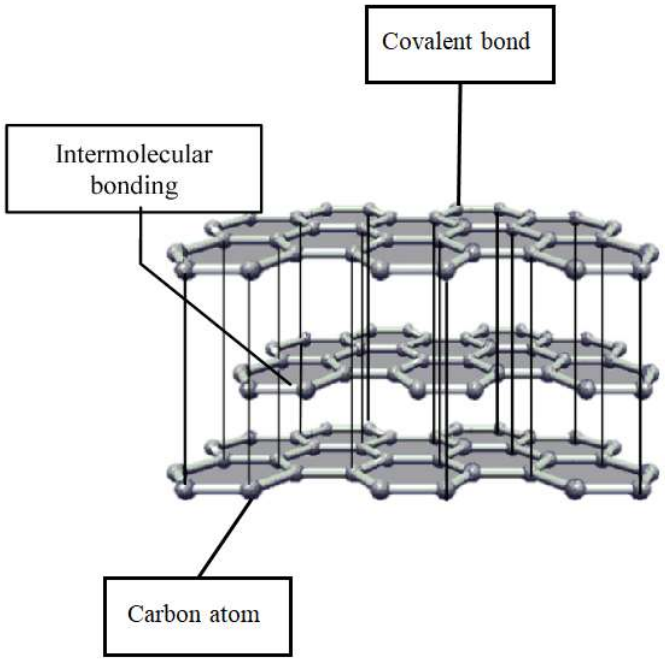

Fig. 1.3 Activated carbon structure with the intermolecular bonding on microcrystalline carbon layers (CHAEMSANIT et al., 2017).

The classification of activated carbon is divided based on its uses and physical properties such as:

(a) Powdered Activated Carbon

The raw material for making PACs is organic material that contain of high carbon content such as wood, coal and lignite. Generally, PAC has a diameter of about 0.1 mm with a specific density between 23-43 lb/ft^3 and its characterization is based on the number of iodine and molasses to describe the amount of pore volume in the PAC. The minimum iodine number in the PAC is 500.

(b) Granular Activated Carbon

The raw material for making GAC is relatively similar with PAC. When compared with PAC, GAC has a larger particle size with a diameter between 1.2-1.6 nm with the density between 25-31 lb/ft^3. For its characterization, the minimum number of iodine and molasses from GAC is relatively the same as PAC.

(c) Extruded Activated Carbon (EAC)

EAC is a mixture of PAC with a binder through a fusion and extrusion processes into a cylindrical activated carbon with a diameter of 0.8-130 mm. To get a certain pore structure, chemical activation is usually done by mixing of KOH before the extrusion process. Generally, the use of EAC is for gas adsorption due to low dust content and great mechanical strength.

(d) Impregnated Carbon

Carbon material that has a good distribution of chemicals as impregnation on the surface of the material. Optimization of activated carbon through impregnation provides a synergy between impregnant and carbon. Some impregnants have been used in several previous works such as Fe, Al, Zn, Ag, K, Ca and Li for several applications such as catalyst, gas purification, coating materials and environmental treatment (Henning and Schäfer, 1993).

(e) Polymers Coated Carbon

For this type, the coating process of porous carbon with polymers provides several advantages, one of which is a smooth surface structure without blocking the carbon pores (Marsh and Rodríguez-Reinoso, 2006).

1.2.2 Preparation of Activated Carbon

In the process of activating activated carbon, both types of chemical and physical activation have been widely used. The difference in the process and the used of activation agent become the parameter to distinguish those processes (Ahmadpour and Do, 1996).

(a) Chemical Activation

In chemical activation, the impregnation process is strongly influenced by activation agents which are typically a strong acid or base. Where the carbon content of the obtained products increases with the minimum production of tar as a by-product. Compared to physical activation, the used temperature is lower so that it is capable to form porous structures (micropores). Some of the activation agents that are often used

include zinc chloride ($ZnCl_2$), phosphoric acid (H_3PO_4), sodium hydroxide (NaOH) and potassium hydroxide (KOH). The weight ratio between activation agents and raw materials plays an important role in the impregnation process. The greater the activation agent ratio, the greater the obtained diameter of the pore volume (Basso et al., 2002). Chemical activation offers several benefits compared to physical activation, such as lower energy consumption, one step process and higher yield. On the other hand, chemical activation also has some disadvantages such as the addition of washing process after the heat treatment and increase the environmental corrosion due to the use of toxic and corrosive chemicals such as $ZnCl_2$ and H_3PO_4 (Ozdemir et al., 2014).

(b) Physical Activation

The combination of carbonization and activation/oxidation processes are generally used in the physical activation process. For the carbonization process, the aim is to change the properties of the source material by reducing the volatile content during the activation process so that the obtained final product contain with around 80 percent of carbon. Elements removal of hydrogen and oxygen occur in the initial stage of pyrolytic decomposition which cause the formation of organized crystallization of the released carbon atoms. The activation process is usually carried out at temperature of 600-900^{o}C with the presence of inert gases such as nitrogen and argon.

While, for the activation/oxidation process, this process is carried out at temperature between 800-1100^{o}C using several gases as activation agents such as carbon dioxide, steam and oxygen. The choice of the reaction temperature must be careful because it determines the reaction rate between gas and carbon. The use of oxygen gas as an activating agent is basically more reactive for a carbon skeleton consisting of carbon dioxide and carbon monoxide in the carbonization process. Furthermore, the very aggressive nature of oxygen gas also cause the combustion on the carbon surface which affect to a large loss.

1.2.3 Hydrothermal Carbonization (HTC)

Hydrothermal carbonization, also called as a wet pyrolysis, is a converting process of biomass using water medium at subcritical temperature and pressure of water. On the HTC process, the conversion occurs in a closed system at temperature

around 180-250ºC and the pressure of 20-60 bar for 5-240 min (Kambo and Dutta, 2015). In other hand, the liquefaction and gasification hydrothermal tend to be more dominant at temperatures above 250ºC. In hydrothermal carbonization, the biomass will be converted in three types of product, namely solid phase (hydrochar), liquid phase (bio-oil) and gas phase (especially CO_2) (Kambo and Dutta, 2015). Compare to natural coal, the similarity of the chemical structure and energy content of the hydrochar can make it suitable as a fuel. The application of hydrochar has been applied in several fields such as water purification, energy storage and catalyst processes (Titirici et al., 2007). The HTC process provides several benefits which are presented below.

(a) The use of relatively low reaction temperature (180-250ºC).
(b) Cheap process, due to the carbonization in water occurs under autogenous pressure.
(c) The formation of spherical micro particles with "core-shell structure) which can improve the surface area and to protect inner particles.
(d) Easy to control porosity of materials by natural template, nanocasting and activation treatments.
(e) Easily facilitate the formation of carbon composites with typical physicochemical properties.
(f) It is easy to control surface functional groups and the electrical properties of the produced carbon particles.

1.2.4 Spinel Ferrite

Spinel ferrite are a class of iron-based materials that has a spinel structure with trivalent ions. There are tetrahedral and octahedral cationic sites created by the *face center cubic* (FCC) phase of oxygen atoms. There are 8 tetrahedral sites filled from a total of 64 interstitial tetrahedral sites, and 16 octahedral sites filled from 32 octahedral interstitial sites. In general, spinel ferrite has a typical structure such as $(A^{2+})(B^{3+})_2O_4$ with A is a tetrahedral cationic sites and B is an octahedral cationic sites (Paufler, 2006).

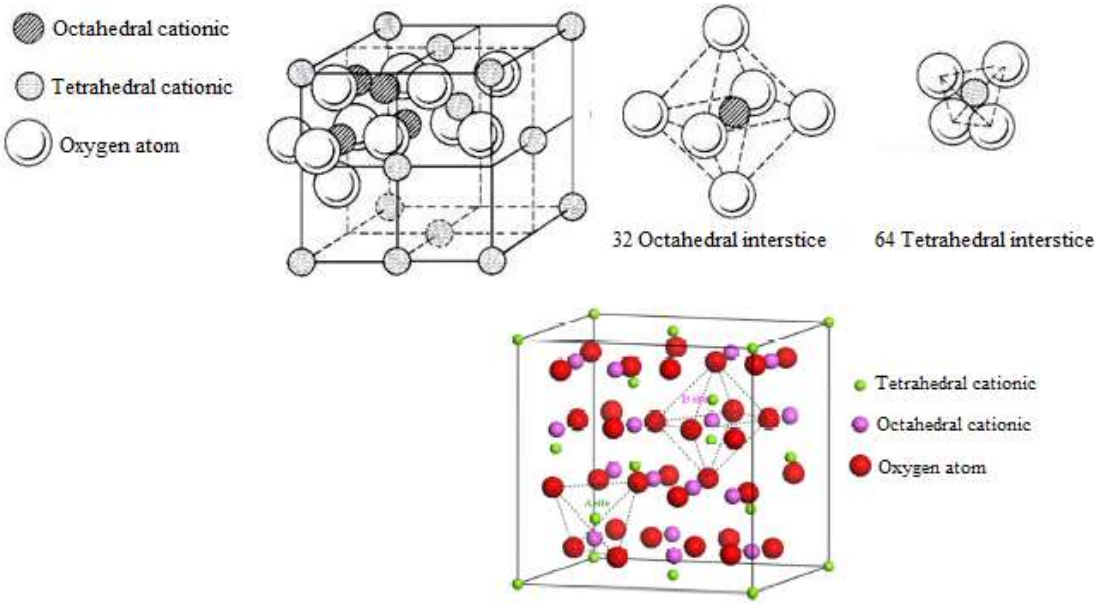

Fig. 1.4 Geometric structure of cubic spinel ferrite (Paufler, 2006).

The geometric structure of spinel ferrite is divided into two classes, normal spinel and inverse spinel. In the normal spinel structure, A is occupied by Fe^{2+} on the tetrahedral structure and site B is occupied by Fe^{3+} octahedral structure. While in the inverse spinel structure, A was occupied by Fe^{3+} and B was randomly occupied by Fe^{2+} and Fe^{3+} (Jeong et al., 2016). The geometry structure of the two types of spinel ferrite as shown below.

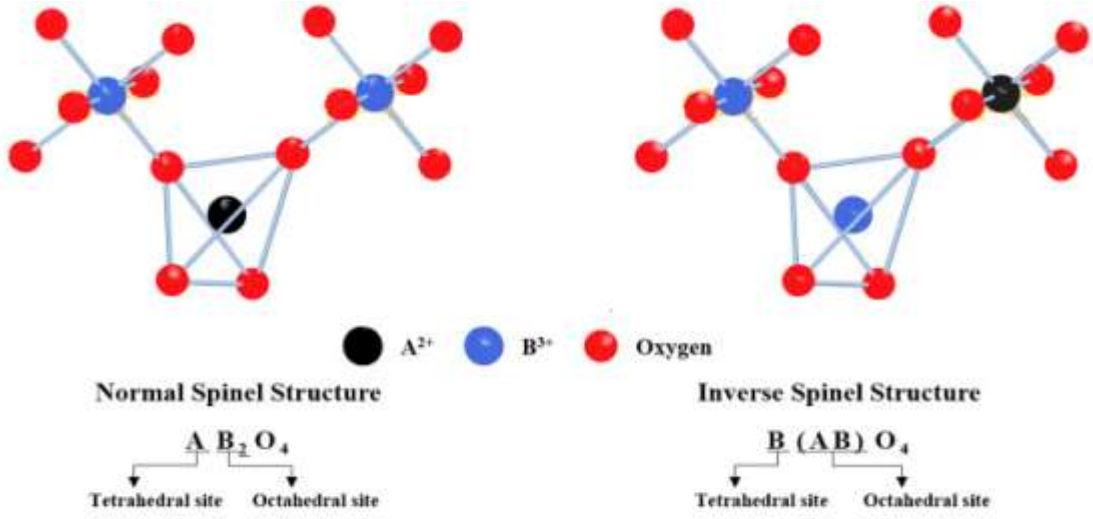

Fig. 1.5 Normal spinel and inverse spinel structures (Jeong et al., 2016).

1.2.5 Disodium Ethylenediaminetetraacetic acid (Na_2EDTA)

Disodium ethylenediaminetetraacetic acid (Na_2EDTA) is an inorganic salt which has a functional group of amines and carboxylic acids as hexadentate ligand. The structure of Na_2EDTA and its properties is shown below:

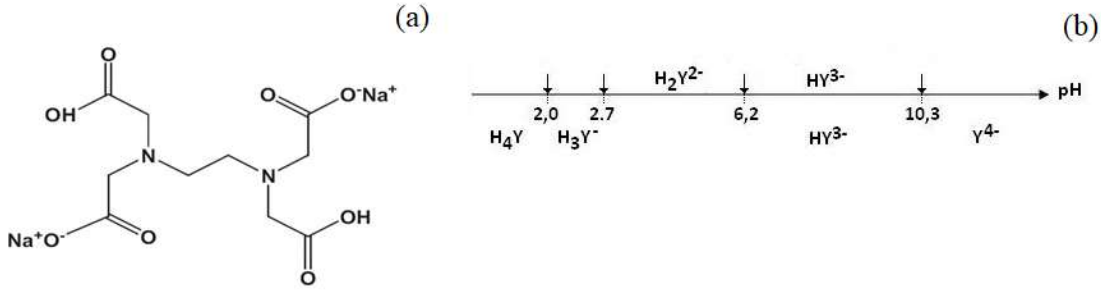

Fig. 1.6 (a) Chemical structure of Na_2EDTA and (b) predominant species of Na_2EDTA at different pH value (Maketon et al., 2008, Zhao et al., 2017)

IUPAC Name:

2-[2-[bis(carboxymethyl)amino]ethyl-(carboxymethyl)amino]acetic acid;sodium

Common Names: EDTA disodium, Disodium ethylenediaminetetraacetic acid

Molecular Formula: $C_{10}H_{16}N_2Na_2O_8$

Molecular Mass: 338.22 $g.mol^{-1}$

Flash Point: > 100ºC

Solubility in water at 25ºC: 1000 $g.L^{-1}$

Ethylenediamine tetraacetic acid (EDTA) has been used as a low-cost, strong and stable chelating agent for metal ions. Functionalization of several materials with EDTA has carried out such as on Fe_3O_4/graphine oxide (Zhao et al., 2017), Fe_3O_4/SiO_2 (Liu et al., 2016), graphene oxide (Cui et al., 2015) nano-Fe_3O_4 (Wang et al., 2012b) and $CoFe_2O_4$ (Zou et al., 2017). Addition of EDTA also does not cause secondary pollution, thus adding to the prospective value of EDTA as chelating agents. Na2EDTA is an inorganic salt which is acidic and difficult to dissolve under very low pH value.

Na2EDTA will change to a dissociated species depending on the pH value and the corresponding pKa value as below (Maketon et al., 2008):

H_4Y species dominates at pH < ~2.

H_3Y^- species allies at ~ 2 < pH < ~2.7.

H_2Y^{2-} species dominates at ~ 2.7 < pH < ~6.2.

HY^{3-}species dominates at ~ 6.2 < pH < ~10.3.

Y^{4-} species dominates at pH > ~10.3.

1.2.6 Rhodamine B

Basic dyes are included in the class of cationic dyes which are considered more toxic than anionic dyes. Rhodamine B is a class of basic dyes that are often used in the textile, paint, leather and food industries. The molecular size of Rhodamine B (1.44 nm) is much greater than the size of other molecular aromatic compounds such as phenol (0.58 nm) (Jiang and Huang, 2016). The structure of Rhodamine B and its properties is shown below:

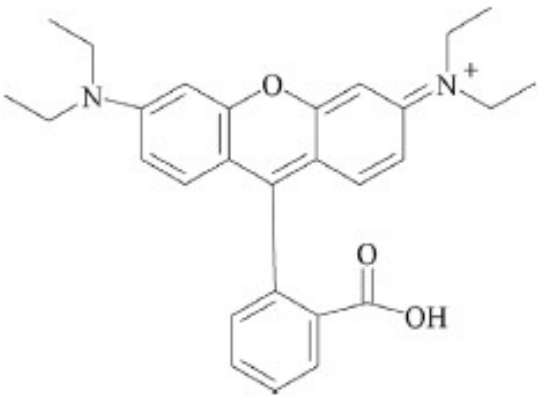

Fig. 1.7 Chemical structure of Rhodamine B (Sattar et al., 2017).

IUPAC Name:

9-(2-carboxyphenyl)-6-diethylamino-3-xanthenylidene]-diethylammonium chloride)

Common Names: Pigment Violet 1, Rhodamine B, Basic Violet 10, Rhodamine 540

Molecular Formula: $C_{28}H_{31}ClN_2O_3$

Molecular Mass: 479.02 $g.mol^{-1}$

Melting point: 210-211°C

Solubility in water at 20°C: 50 $g.L^{-1}$

In recent years, the water pollution caused by the wastewater contaminated with Rhodamine B has received a lot of attention due to it can destroy the environment and harm to human. Water contaminated with Rhodamine B when it is consumed by human will cause respiratory and digestive problems, eye and skin irritations, neurotoxic, chronic and carcinogenic (Bordoloi et al., 2018, Jiang and Huang, 2016, Khamparia and Jaspal, 2017, Thakur and Kaur, 2017).

1.2.7 Ibuprofen sodium salt

Ibuprofen is one of the drugs in the class of non-steroidal anti-inflammatory drugs derived from propionic acid with the IUPAC name, namely 2- (4-isobutylphenyl) propionate. The first development of ibuprofen was carried out in the 1960s when it was looking for safer alternative drugs of aspirin. In 1961-1974, ibuprofen was patented and launched as a drug to against rheumatoid arthritis in the United Kingdom and America.

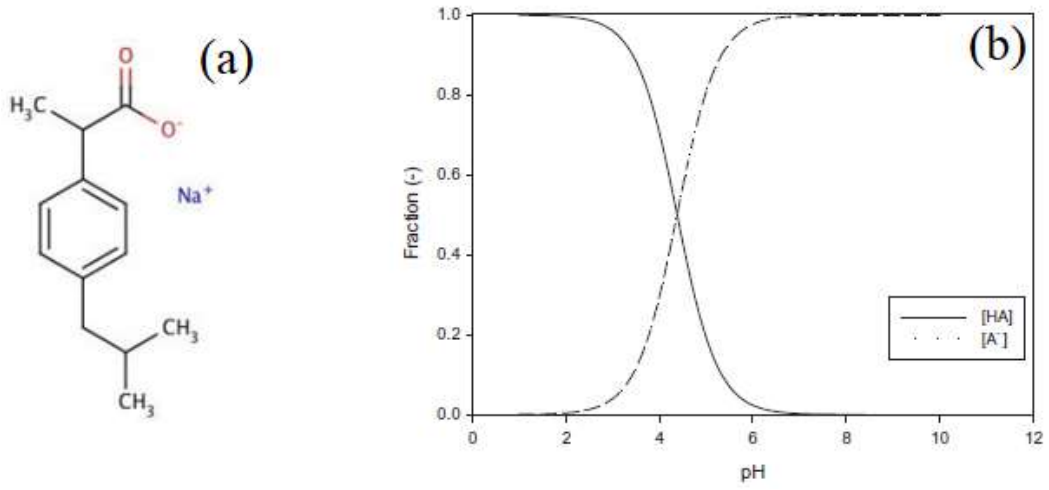

Fig. 1.8 (a) Chemical structure and (b) speciation diagram of Ibuprofen sodium salt in aqueous solution (Iovino et al., 2015).

IUPAC name: Sodium 2-[4-(2-methylpropyl)phenyl]propanoate

Common names: Esprenit (TN), p-Isobutylhydratropic acid sodium salt

Molecular Formula: $C_{13}H_{17}NaO_2$

Molecular Mass: 228.26 $g.mol^{-1}$

Solubility in water at 25°C: 21.9 $g.L^{-1}$

Ibuprofen is often used to treat muscle aches, headaches, arthritis or injuries. Ibuprofen will play a role in suppressing prostaglandin production thereby reducing pain and fever. Frequently appearance of ibuprofen in wastewater systems can be due to high human consumption of anti-inflammatory and analgesic so that making ibuprofen as a pollutant candidate in water systems. Several studies have proven that water pollution by this substance can be caused by the use and excretion of human, and can be caused by industrial waste of fungicides and disinfectants (Mestre et al., 2007).

1.2.8 Copper ion (Cu^{2+})

Copper is one of the important elements for human health and at least around 900 μg of copper is needed by the adult human body. However, excess copper intake is also dangerous for humans such as headaches, dizziness and diarrhea. There needs to be monitoring and controlling for the amount of released copper into the environment so that it does not pose a dangerous impact to human life. Copper is one of the heavy metals commonly found in several water sources that can come from various sources. For example in the United States, mining and processing of copper which produce wire, pipes and sheet metal is potentially become a pollutant source.

Table 1.1 Limit of various permitted heavy metals and their effects on human health (Sud et al., 2008)

Metal contaminant	Permissible limits for industrial effluent discharge (in mg/l)			Permissible limits by international bodies (µg/l)		Health hazards
	Into inland surface waters Indian Standards: 2490(1974)	Into public sewers Indian Standards: 3306(1974)	On land for irrigation Indian Standards: 3307 (1974)	WHO	USEPA	
Arsenic	0.20	0.20	0.20	10	50	Carcinogenic, producing liver tumors, skin and gastrointestinal effects
Mercury	0.01	0.01	–	01	02	Corrosive to skin, eyes and muscle membrane, dermatitis, anorexia, kidney damage and severe muscle pain
Cadmium	2.00	1.00	–	03	05	Carcinogenic, cause lung fibrosis, dyspnea and weight loss
Lead	0.10	1.00	–	10	05	Suspected carcinogen, loss of appetite, anemia, muscle and joint pains, diminishing IQ, cause sterility, kidney problem and high blood pressure
Chromium	0.10	2.00	–	50	100	Suspected human carcinogen, producing lung tumors, allergic dermatitis
Nickel	3.0	3.0	–	–	–	Causes chronic bronchitis, reduced lung function, cancer of lungs and nasal sinus
Zinc	5.00	15.00	–	–	–	Causes short-term illness called "metal fume fever" and restlessness
Copper	3.00	3.00	–	–	1300	Long term exposure causes irritation of nose, mouth, eyes, headache, stomachache, dizziness, diarrhea

1.3 Literature Review

Asfaram et al. (2017) conducted a study on the adsorption process of cationic dyes such as brilliant green (BG) and malachite green (MG) using Mn-doped Fe_3O_4 nanoparticle-loaded activated carbon (Mn-Fe_3O_4-NP-AC) assisted with ultrasound simultaneously. Interactions among independent variables were investigated using analysis of variance (ANOVA) with 95% confidence level. The maximum yield for adsorption of BG and MG reached 99.50 and 99.00%, respectively, which occurred at pH 7 for 3 min with 0.02 g of adsorbent dosage. Based on the Langmuir isotherm model, the maximum adsorption capacity for BG and MG are 101.215 and 87.566 mg/g, respectively. In another study conducted by Zhang et al. (2015), manganese-zinc ferrite ($Mn_{0.5}Zn_{0.5}Fe_2O_4$: MZF) was immobilized into activated carbon by a hydrothermal process. The result obtained is the existence of a spinel phase structure inside the active carbon pore resulting in increased saturation magnetization of MZF/AC followed by increased ferrite content, but decreases the specific surface area and pore volume. The adsorption process for methylene blue showed an adsorptive performance value of 99% within 30 min. The MZF/AC separation process can be done easily using magnet.

Shao et al. (2012) conducted the adsorption process of one of the pharmaceutical waste, Tetracycline (TC) using $MnFe_2O_4$-activated carbon magnetic composites made by chemical coprecipitation technique. Separation can be done easily because the composite has magnetic properties. The experimental results show that there is no significant effect of the Fe-Mn spinel phase in the pore structure of the activated carbon to the change of pore volume and specific surface area. The maximum adsorption capacity obtained for Tetracycline adsorption (TC) was 590.5 mmol/kg at pH 5. The adsorption process carried out by $MnFe_2O_4$-activated carbon magnetic composites follows the pseudo-second-order kinetic model where the process is endothermic so that the removal process decreases with increasing pH values and will increase with increasing temperature.

From Zhou et al. (2018), ferromanganese binary oxide-biochar composites (FMBC) are prepared by impregnation or sintering methods to remediate soil and water contaminated by heavy metals. The adsorption process follows the pseudo-second-order kinetic model and the Langmuir isotherm model, while the maximum adsorption capacity of FMBC for Cu^{2+} and Cd^{2+} is 64.9 and 101 $mg.g^{-1}$, respectively. These results were greater than the maximum adsorption capacity produced by biochar for Cu^{2+} and Cd^{2+} were 21.7 and 28 $mg.g^{-1}$, respectively. The increase of pH and humic acid concentration becomes the determining factor in the adsorption process. The results of FTIR and XPS analysis show that the presence of divalent Cu and Cd ions adsorbed in FMBC due to the formation of strong mono- or multi- dentate inner sphere complexes.

Ghobadi et al. (2018) synthesized $MnFe_2O_4$-graphene oxide magnetic nanoparticles to remove rare earth elements/REE (La^{3+} and Ce^{3+}) from aqueous solutions. The maximum adsorption capacity of MnFe2O4-GO for REEs removal was 1001 and 982 $mg.g^{-1}$ which was achieved for 20 min at pH 7 and room temperature, respectively. Adsorption kinetics and isotherms show that the adsorption data were very fit with the Langmuir isotherm model and the pseudo-second order kinetics model. The value of thermodynamic parameters indicated that the adsorption occurs in an endothermic and spontaneous process. In addition, the obtained data from the Dubinin-Radushkevich model predicts the adsorption process via chemical ion-exchange.

Furthermore, regeneration studies show that $MnFe_2O_4$-GO can be regenerated for several successive cycles.

Xu et al. (2018) prepared a combination of manganese ferrite nanoparticles ($MnFe_2O_4$) and graphene oxide (GO) coated with tetraethylenepentamine (TEPA) as novel nanohybrid ternary via a facile hydrothermal and used to remove Pb (II) in aqueous solution effectively. The maximum adsorption capacity of TEPA-GO/$MnFe_2O_4$ (263.2 $mg.g^{-1}$) was higher than GO/$MnFe_2O_4$ (133.3 $mg.g^{-1}$) and GO (196.1 $mg.g^{-1}$) at optimum pH 5.5. Pseudo second order kinetic model and the Langmuir isotherm model were very fit with the experimental data. The value of thermodynamic parameters exhibit that the adsorption process of Pb^{2+} on TEPA-GO/$MnFe_2O_4$ occur spontaneously and endothermic. The regeneration process of TEPA-GO/$MnFe_2O_4$ with HCl show a good percentage of reusability after four consecutive cycles.

Qi et al. (2015) synthesized Fe-Mn impregnated on chitosan bead (FMCB) as an effective novel adsorbent for As^{5+} and As^{3+}. The maximum adsorption capacity for As^{5+} and As^{3+} were 39.1 and 54.2 $mg.g^{-1}$, respectively. FMCB that contains arsenic can be re-modified several times using NaOH. The results of column tests exhibit that there were 233 µg/L of As^{5+} and As^{3+} in the simulated groundwater with 1500 and 3200 bed volumes can be treated by FMCB. These results indicated that FMCB can be applied to remove As^{5+} and As^{3+} for real water matrix.

1.4 Objectives

1.4.1 The fabrication of a novel ethylenediaminetetraacetic acid (EDTA) functionalized hydrochar from green tea waste (*Camelia sinensis*) waste, doped with the manganese ferrite by hydrothermal carbonization (HTC) coupled with the activation process (EDTA-FMHC-700).

1.4.2 Adsorption studies of adsorption capacity and percentage of efficiency on Rhodamine B (RhB) Copper ion (Cu^{2+}) and Ibuprofen (IBP) removal in aqueous solution.

1.4.3 Regeneration studies of EDTA-FMHC-700 on Rhodamine B (RhB) Copper ion (Cu^{2+}) and Ibuprofen (IBP).

CHAPTER 2

RESEARCH METHODOLOGY

2.1 Chemicals and Materials

1. Green tea waste as the raw material is obtained from a coffee shop around the Faculty of Science, Prince of Songkla University
2. Copper (II) sulfate pentahydrate ($CuSO_4.5H_2O$), 98.0%, Sigma-Aldrich, ACS Reagent grade
3 Ferric chloride anhydrous ($FeCl_3$), 99.0%, VWR Chemicals, Analytical Reagent grade
4 Manganese (II) sulfate monohydrate ($MnSO_4.H_2O$), 99.0%, ANaPURE, Analytical Reagent grade
5 Ammonium ferrous sulfate ($(NH_4)_2SO_4.FeSO_4.6H_2O$), 99.0%, UNIVAR, Analytical Reagent grade
6 Rhodamine B ($C_{28}H_{31}ClN_2O_3$), 95.0%, Fluka, Analytical Reagent grade
7 Ibuprofen sodium salt ($C_{13}H_{17}NaO_2$), 98.0%, Sigma-Aldrich, Analytical Reagent grade
8 Sodium hydroxide (NaOH), 97.0%, RCI Labscan, Analytical Reagent grade
9 Potassium hydroxide (KOH), 85%, RCI Labscan, Analytical Reagent grade
10 Ethylenediaminetetraacetic acid disodium salt dihydrate (EDTA), 99.0%, ANaPURE, Analytical Reagent grade
11 Ammonia solution (NH_4OH), 25%, Merck, Analytical Reagent grade.
12 De-Ionized water/DI-water (15 MΩ cm)

2.2 Equipment and Instruments

1. Teflon lined autoclave reactor 400 mL
2. An electric oven; Model ULP 400, Memmert
3. pH meter; Model Delta 320, Mettler Toledo
4. Laboratory shaker, IKA KS 130, China
5. Laboratory shaker, Scilogex SK-O330-Pro, USA
6. Thermostat shaker water bath, WB/OB 7-45, Memmert

7. Neodymium magnet grade N35 (100 mm x 50 mm x 10 mm)
8. CHNS/O Analyzers, Thermo Scientific^{TM} Flash 2000, USA
9. PALS Zeta Potential Analyzer, Brookhaven Instrument , USA
10. Fourier Transform Infrared Spectroscopy (FTIR), Perkin Elmer Spectrum BX, USA
11. Vibrating Sample Magnetometer (VSM), Electricity and Magnetism Research Lab, Kasetsart University, Thailand
12. Surface Area and Porosity Analyzer, Micromeritic ASAP2460, USA
13. X-Ray Diffraction (XRD), PANalytical X'Pert MPD, UK
14. X-ray Photoelectron Spectroscopy (XPS), AXIS Ultra DLD Shimadzu, Japan.
15. Scanning Electron Microscope–Electron Dispersive X-Ray Spectrometer (SEM-EDX), Thermo Scientific^{TM} Apreo, USA
16. UV-Visible Spectrophotometer, Shimadzu UV-2600, Japan
17. Inductively Coupled Plasma-Optical Emission Spectrometer (ICP-OES), Perkin Elmer AVIO^{TM} 500, USA

2.3 Method

2.3.1 Preparation of Fe-Mn Binary Oxide Immobilized into Hydrochar *via* Hydrothermal Carbonization-Activation Process (FMHC and FMHC-700)

Some impurieties of GTW was cleaned using DI water several time until not release any color, then dried for 12 h at 110^{o}C in the oven. The next process, 4.86 g of $FeCl_3$, 7.84 g of $(NH_4)_2SO_4.FeSO_4.6H_2O$, 1.7 g of $MnSO_4.H_2O$ with the ratio of $Fe^{3+}/Fe^{2+}/ Mn^{2+}$ (~ 4.3:1:0.2 by mol) were dissolved and homogenized in the 100 mL of DI water, then poured into the reactor. After that, 20 g of GTW was mixed into the mixture and stirred vigorously at the temperature of 80^{o}C for 2 h. Then, 100 mL of potassium hydroxide (KOH) solution was added dropwise and stirred for 1 h (GTW:KOH = 1:3 %wt). The reactor was hydrothermally heated at 220^{o}C for 24 h in the oven. Next, it was separated with external magnet, washed by acetone and DI water until clear and reach neutral pH. Then, dried in the oven at 100 ^{o}C for 5 h. The obtained product was labelled as FMHC. For the activation process, the FMHC was heated using a pyrolizer at 700^{o}C for 3h under N_2-atmosphere with heating rate 5^{o}C/min. Finally, the product was labelled as FMHC-700.

2.3.2 EDTA coated onto activated Fe-Mn hydrochar (EDTA-FMHC-700)

4 g of EDTA was dissolved in 100 mL of DI water and added 10 mL of ammonia solution to adjust the solution pH under alkaline condition. Then, 15 g of FMHC-700 was added into the above solution and stirred at 60ºC for 24 h. Furthermore, the sample was separated from the solution using an external magnet and washed several times with DI water and dried in the oven at 100ºC for 5 h. The sample was labeled as EDTA-FMHC-700 and stored for further use.

2.3.3 Characterization of Materials

2.3.3.1 Elemental Analysis

Elemental Analyzer (Thermo Scientific^{TM} Flash 2000 CHNS/O Analyzers, USA) was used to determine the chemical compositions of FMHC, FMHC-700 and EDTA-FMHC-700.

2.3.3.2 Zeta Potential Analyzer

Zeta Potential Anlayzer (PALS Zeta Potential Analyzer, Brookhaven Instruments Corp, USA) was used to measure the zeta potential of FMHC, FMHC-700 and EDTA-FMHC-700 at the pH range of 2 to 12.

2.3.3.3 Field-Emission Scanning Electron Microscopy-Electron Dispersive X-Ray Spectrometer (FESEM-EDX)

FESEM-EDX (Thermo Scientific^{TM} Apreo Scanning Electron Microscope, USA) was used to describe the morphology and elemental analysis of FMHC, FMHC-700 and EDTA-FMHC-700.

2.3.3.4 XRD

X-Ray Diffraction (XRD, PANalytical X'Pert MPD) was used to observe diffraction patterns and crystalline systems of FMHC, FMHC-700 and EDTA-FMHC-700.

2.3.3.5 Surface Area and Porosity Analyzer

The Nitrogen sorption Analyzer (Micromeritic ASAP2460, USA) was used to measure the specific surface area, pore volume and average pore diameter of FMHC, FMHC-700 and EDTA-FMHC-700.

2.3.3.6 Vibrating Sample Magnetometer (VSM)

Vibrating Sample Magnetometer (VSM) was used to measure the magnetic properties of FMHC, FMHC-700 and EDTA-FMHC-700 at room temperature.

2.3.3.7 XPS

X-Ray Photoelectron spectroscopy (XPS, AXIS Ultra DLD Shimadzu) was used to confirm the surface functional groups of FMHC, FMHC-700 and EDTA-FMHC-700.

2.3.3.8 Fourier Transform Infrared (FTIR) Spectroscopy

FTIR spectroscopy (Perkin Elmer Spectrum BX, USA) using the KBR pellet method was used to analyze some functional groups from FMHC, FMHC-700 and EDTA-FMHC-700 at the wavenumber of 400 to 4000 cm^{-1}.

2.3.4 Adsorption of Rhodamine B, copper ion (Cu^{2+}) and ibuprofen

The adsorption of RhB, copper ion (Cu^{2+}) and IBP was conducted by a batch processes. Some parameters such as effect of contact time (0-180 mins) and initial concentration (10-250 $mg.L^{-1}$), effect of adsorbent mass (0.01-0.1 g), effect of solution pH (pH 2-11) and effect of temperature (30-50^{o}C) were studied in the adsorption of RhB, copper ion (Cu^{2+}) and IBP. For the experiment process, a number of EDTA-FMHC-700 was added into 50 mL of RhB, copper ion (Cu^{2+}) and IBP solutions at the natural pH of each adsorbates, respectively. After the adsorption reach equilibrium condition, the adsorbent was separated from each solution using an external magnet. All of the adsorption experiments were carried out for three times. To study kinetics and isotherm adsorption, the adsorption capacity (q_e) and removal efficiency ($\% R$) of adsorbent would be determined using Eq. (1) and (2):

$$q_e = \frac{(C_0 - C_e)V}{W} \quad (1)$$

$$Removal\ efficiency\ (\%\ R) = \frac{(C_0 - C_e)}{C_0}\ x\ 100 \quad (2)$$

Where q_e is the amount of adsorbates which was adsorbed by adsorbent (mg.g^{-1}), C_0 and Ce are the initial and equilibrium concentration of adsorbates (mg.L^{-1}), V is the volume of solution (L) and W is adsorbent mass (g).

2.3.5 Regeneration studies of EDTA-FMHC-700

To investigate the regeneration and reusability of the adsorbent, EDTA-FMHC-700 was added into 50 mL of each adsorbate solutions, then shaked at room temperature. After the adsorption reach equilibrium, an external magnet is used to separate between EDTA-FMHC and adsorbates solution. The collected EDTA-FMHC-700 were desorbed using 20 mL of acetone for Rhodamine B and Ibuprofen (Saleh and Ali, 2018, Tzereme et al., 2019), then 20 mL of 0.1 M HCl for copper ion (Cu^{2+}) for 1 h (Cui et al., 2015), respectively. The adsorbents were washed with DI water until reach neutral pH, then heated at 100^{o}C for 5 h. Finally, the EDTA-FMHC-700 was reused to remove all adsorbates in four successive cycles.

Furthermore, the software namely OriginPro 2018, SpectraGryph 1.2 and ChemDraw 15 (Legal Version) were used to prepare the obtained data from the experimental results.

CHAPTER 3

RESULTS AND DISCUSSION

3.1 The Fabrication of FMHC and EDTA-FMHC-700

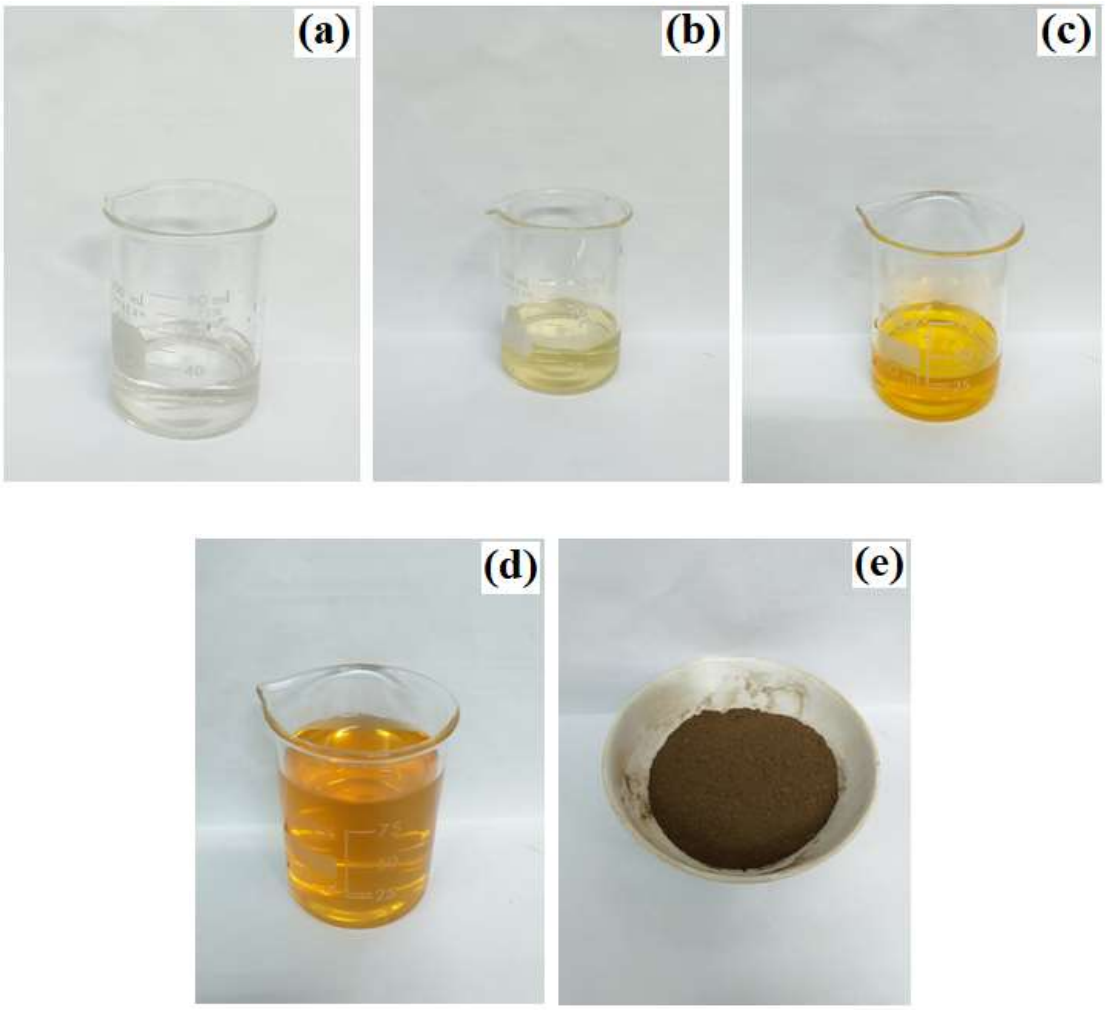

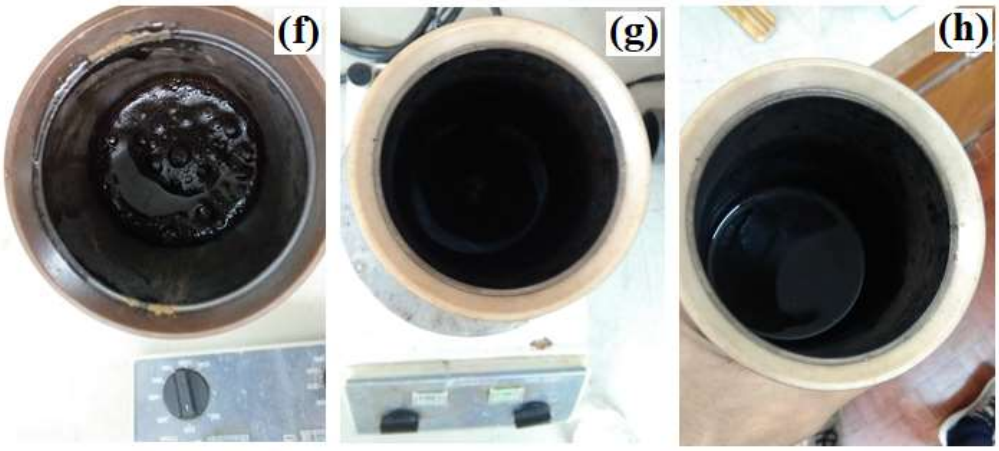

Fig. 3.1 (a) $MnSO_4.H_2O$, (b) $(NH_4)_2SO_4.FeSO_4.6H_2O$, (c) $FeCl_3$, (d) Fe-Mn solution, (e) GTW, (f) mixture of GTW and Fe-Mn solution, (g) before and (h) after hydrothermal carbonization

The first step was the fabrication of magnetic Fe-Mn binary oxide ($MnFe_3O_4$) immobilized on hydrochar *via* the hydrothermal carbonization at a temperature of 220ºC for 24 h. The solution of Fe^{3+}, Fe^{2+} and Mn^{2+} source as well as GTW as raw material were prepared firstly, as shown in Fig. 3.1(a-e). All materials were mixed into the autoclave reactor and heated at 80ºC for 2 hours. This heating process aims to assist the dispersion of Fe-Mn into the GTW pores. Then KOH solution was added which was to control the pH of the mixture so that Fe^{3+}, Fe^{2+} and Mn^{2+} settles. The color of mixture before the hydrothermal carbonization was dark brown, then the color changed to be black after hydrothermal carbonization done as shown in Fig. 3.1(f-h). When the hydrothermal carbonization process takes place, GTW will be converted into hydrochar through hydrolysis, dehydration and decarboxylation of cellulose derivatives which allow $MnFe_2O_4$ to be immobilized on the surface and in the carbon matrix of hydrochar. Finally, the obtained solid product are labeled as FMHC.


(a)
100
50


(b)


(c)

Fig. 3.2 The image of (a) coating process with EDTA and magnetic response of (b) FMHC, (c) FMHC-400 and (d) EDTA-FMHC-700

However, further heating was carried out at a temperature of 700ºC for 3 h under nitrogen atmosphere. The purpose of this process was to increase the physical properties of the material and removing unwanted impurities compounds. The color of the obtained product looks like black solid, then it was labeled as FMHC-700. The last step was to modify the FMHC-700 surface by using ethylenediaminetetraacetic acid (EDTA) to improve the performance and physical properties of the adsorbent, as shown in Fig. 3.2a. This process was conducted at 80ºC for 12 h to ensure that EDTA was optimally coated on the FMHC-700 surface. The color of the obtained product was brownish black, then it was labeled as EDTA-FMHC-700. For information, all synthesized materials were separated from the solution using an external magnetic field.

Furthermore, all synthesized materials also exhibit good magnetic properties, as shown in Fig. 3.2(b-d). From Fig. 3.2b, FMHC exhibits good magnetic properties with a very strong response to the external magnetic field and can be completely separated from the water within 5 s. As for FMHC-700, its response to the external magnetic field decreases and can be separated from the water within 8 s, as shown in Fig. 3.2c. This was probably caused by the change in the chemical structure of FMHC due to the activation process which decreases its magnetic properties. While the response of EDTA-FMHC-700 to the external magnetic field was lowest compared to FMHC and FMHC-700 so that it can be separated within 12 s, as shown in Fig. 3.2d. The reduced

magnetic response from EDTA-FMHC-700 can be caused by the previous activation process and the addition of EDTA to FMHC-700.

3.2 Material Characterizations

3.2.1 Elemental Analysis

Table 3.1 Elemental composition of FMHC, FMHC 700 and EDTA-FMHC-700

Samples	**C[a] (%)**	**H[a] (%)**	**N[a] (%)**	**O[a] (%)**	**Fe[b] (%)**	**Mn[b] (%)**	**Other elements (%)**
FMHC	11.42	1.57	0.14	22.71	39.50	8.60	16.06
FMHC-700	5.79	0.18	0.06	11.18	51.60	11.90	19.29
EDTA-FMHC-700	5.92	0.26	0.14	14.23	51.80	9.90	17.75

[a] Measured by CHNO analysis, [b] Measured by EDX analysis

Elemental analysis data for FMHC, FMHC-700 and EDTA-FMHC-700 were presented in Table 3.1. The C, H, N and O contents on FMHC-700 were lower than FMHC which may be caused by the further hydrolysis, dehydration and decarboxylation of the hydrochar matrix during the activation process. Conversely, the Fe and Mn contents on FMHC-700 were relatively higher compared to FMHC. This can be caused by the activation process which enable the crystal phase growth of Fe and Mn. For EDTA-FMHC-700, the increase of the C, H, N and O contents can be caused by the addition of EDTA on FMHC-700. Whereas the Fe and Mn contents in EDTA-FMHC-700 was relatively constant.

3.2.2 Zeta Potential Analyzer

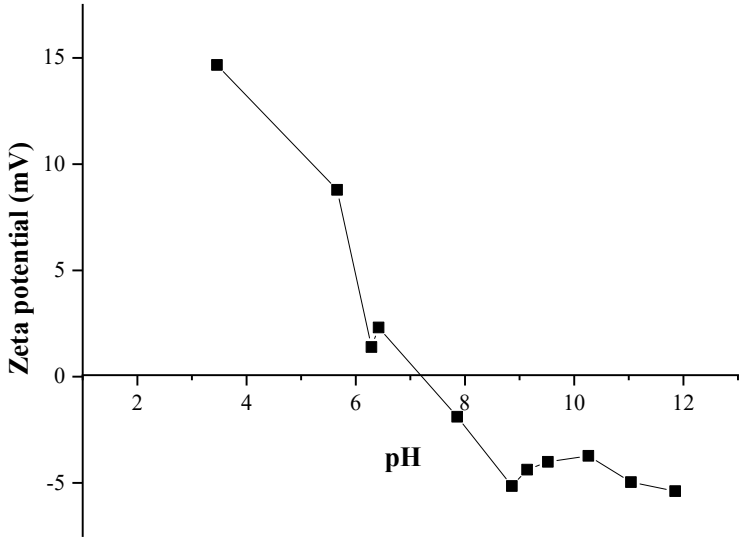

Fig. 3.3 Zeta potential of EDTA-FMHC-700 at different pH

Zeta potential measurement was used to evaluate electrostatic mobility on the surface of the adsorbent and determine the pH at point of zero charge (pH_{pzc}) or pH where the adsorbent surface zero total charge (isoelectric point). The zeta potentials of EDTA-FMHC-700 were evaluated at different pH and room temperature, as shown in Fig. 3.3. With increasing pH value, the zeta potential of EDTA-FMHC-700 decrease gradually, then the obtained pH_{pzc} was 7.21. Therefore, the EDTA-FMHC-700 surface will be positively charged at pH < pHpzc where this will have the effect on substances containing positive charge with the emergence of electrostatic repulsion. Conversely, the surface of EDTA-FMHC-700 will be negatively charged if pH > pHpzc so that will produce electrostatic attraction between the adsorbent surface and the substances containing positive charge (Xu et al., 2018).

3.2.3 Field-Emission Scanning Electron Microscopy-Electron Dispersive X-Ray Spectrometer (FESEM-EDX)

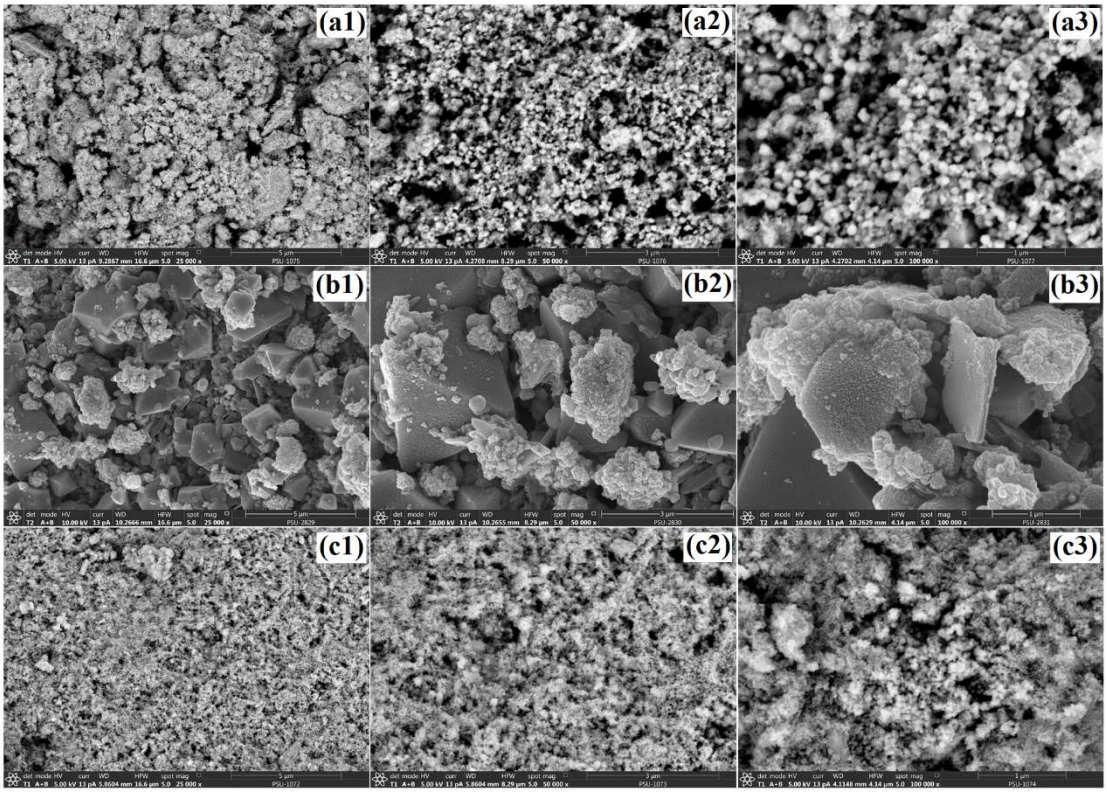

Fig. 3.4 Morphology studies of (a) FMHC, (b) FMHC-700 and (c) EDTA-FMHC-700 by FESEM

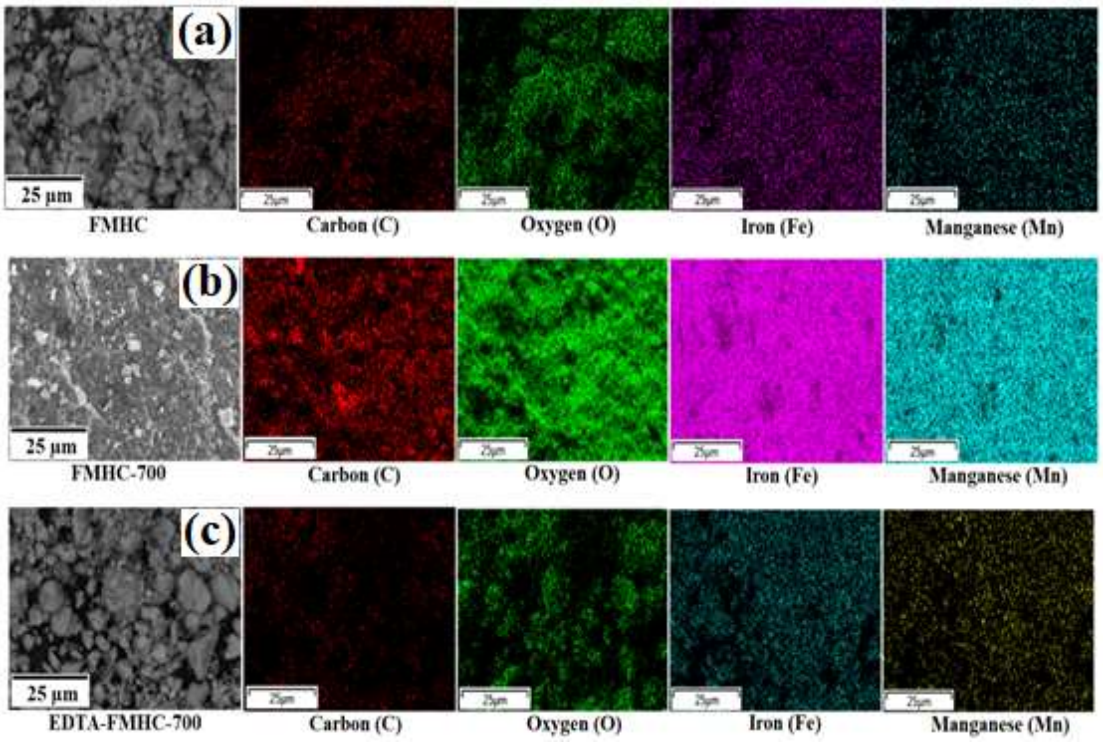

Fig. 3.5 Elemental mapping of C, O, Fe and Mn onto (a) FMHC, (b) FMHC-700 and (c) EDTA-FMHC-700 by FESEM-EDX

The surface morphology and the particle size of FMHC, FMHC-700 and EDTA-FMHC-700 were depicted using FE-SEM at the magnification of 25000-100000x. As presented in Fig. 3.4(a1-a3), particles of $MnFe_2O_4$ were distributed uniformly with the spherical shape on the FMHC surface with the average diameter of 50-200 nm. In the image of FMHC-700, its surface morphology exhibits the partial phase transformation from spherical shape to tetragonal-like shape that might be caused by the activation process as shown in Fig. 3.4(b1-b3). While for EDTA-FMHC-700, the surface morphology shows a rough, wrinkled and micro-porous that disperse homogeneously which was indicate the presence of EDTA on the adsorbent surface as shown in Fig. 3.4(c1-c3). Furthermore, the existence of C, O, Fe and Mn on EDTA-FMHC-700 were confirmed by EDX mapping, as shown in Fig. 3.5. All of these results prove the successful synthesis of $MnFe_2O_4$ on the hydrochar surface as a carbon matrix coated by EDTA.

3.2.4 X-Ray Diffraction (XRD)

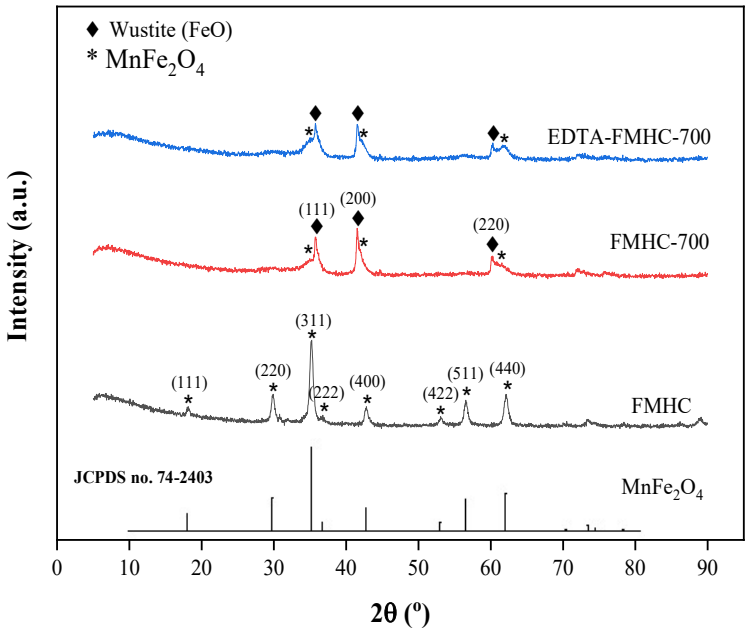

Fig. 3.6 X-Ray diffraction patterns of FMHC, FMHC-700 and EDTA-FMHC-700

Fig. 3.6 shows the XRD patterns of FMHC, FMHC-700 and EDTA-FMHC-700. The XRD pattern of FMHC exhibits the diffraction peaks at 2θ values of 18.2°, 29.9°, 35.2°, 36.8°, 42.8°, 53.1°, 56.5° and 62.1° reflect the (111), (220), (311), (222), (400), (422), (511) and (440) crystal planes of the cubic spinel ferrite phase of manganese ferrite ($MnFe_2O_4$) which was in accordance with the JCPDS no. 74-2403 (Xu et al., 2018). This result exhibits the presence of $MnFe_2O_4$ in the obtained FMHC composite. After the activation process, the FMHC-700 diffraction pattern shows the broad diffraction peaks at 2θ values of 35.8°, 41.6° and 60.3° represent the (111), (200) and (220) crystal planes of the wustite phase of FeO refer to ICDD no. 01-074-1886. The partial change of the crystal planes of iron species in $MnFe_2O_4$ during the activation process are probably due to the less stable of iron species during the activation process at high temperatures which form other iron species with the wustite phase (FeO) (Ding et al., 2015, Yoon et al., 2017).

3.2.5 Surface Area and Porosity Analyzer

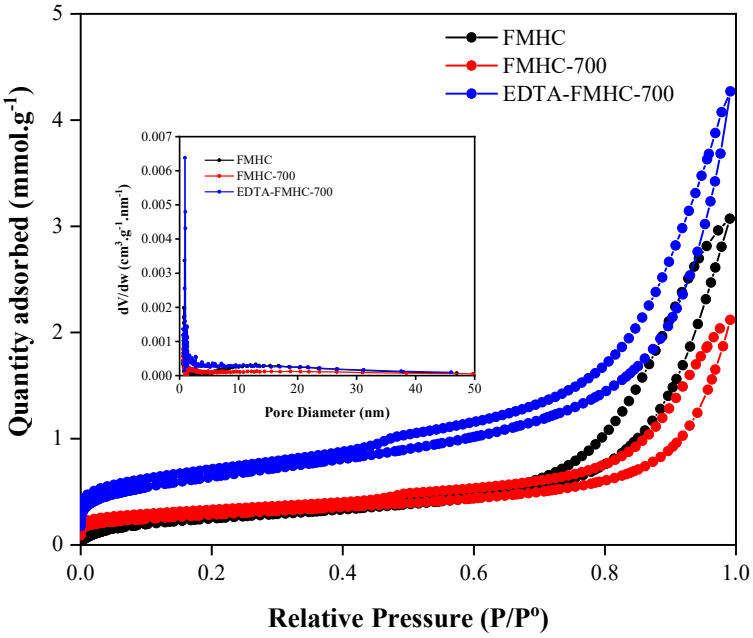

Fig. 3.7 Nitrogen adsorption-desorption isotherm curves of FMHC, FMHC-700 and EDTA-FMHC-700

The BET surface area and pore size analysis for FMHC, FMHC-700 and EDTA-FMHC-700 were described in Fig. 3.7. All of them exhibit type II isotherms (according to the IUPAC classification) with H3 type hysteresis loops which correspond to non-porous or supermicroporous material also refer to open-wedge pores shape with the average pore diameter around 0.09 nm which was shown at inset Fig. 3.7 (Boruah et al., 2019, Sultan et al., 2018, Zhang et al., 2016). These three loops may arise due to the immobilization of $MnFe_2O_4$ into the carbon matrix (Xu et al., 2018). Additionally, the BET surface area and pore volume from FMHC, FMHC-700 and EDTA-FMHC-700 were 21.58, 22.28 and 48.97 $m^2.g^{-1}$ and 0.105, 0.07 and 0.144 $cc.g^{-1}$, respectively. The surface area, pore volume and pore size of EDTA-FMHC-700 greater than FMHC and FMHC-700 were likely to be caused by the addition of EDTA which can improve the physical properties of the adsorbent.

3.2.6 Vibrating Sample Magnetometer (VSM)

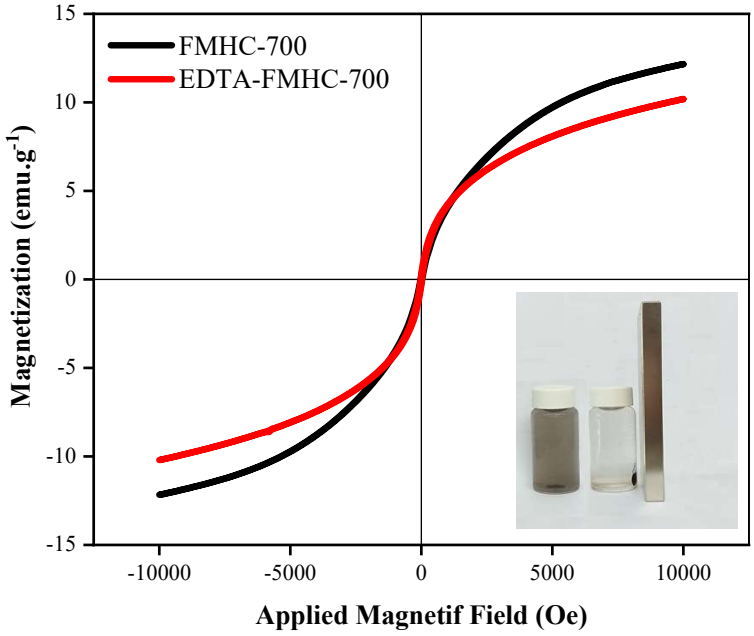

Fig. 3.8 Magnetic hysteresis loops of FMHC-700 and EDTA-FMHC-700

As shown in Fig. 3.8, the magnetization hysteresis loops of FMHC-700 and EDTA-FMHC-700 were measured with an applied magnetic field of 10 kOe at room temperature. The saturation magnetization of FMHC-700 and EDTA-FMHC-700 were 12.16 and 10.18 emu.g^{-1}, respectively. The saturation magnetization of EDTA-FMHC-700 which was slightly decreased was probably caused by the presence of EDTA on the FMHC-700 surface. In the inset Fig. 3.8, the separation process of EDTA-FMHC-700 from water through the external magnetic field can be achieved completely within 12 s. The magnetic separation performance of EDTA-FMHC-700 which was relatively good, easy and fast can provide benefits after the adsorption process which saves more time and costs.

3.2.7 X-Ray Photoelectron Spectroscopy (XPS)

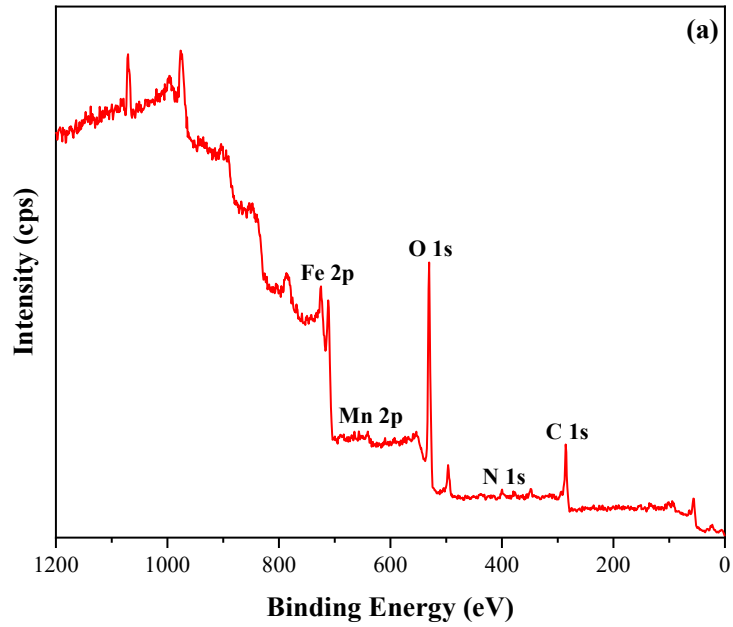

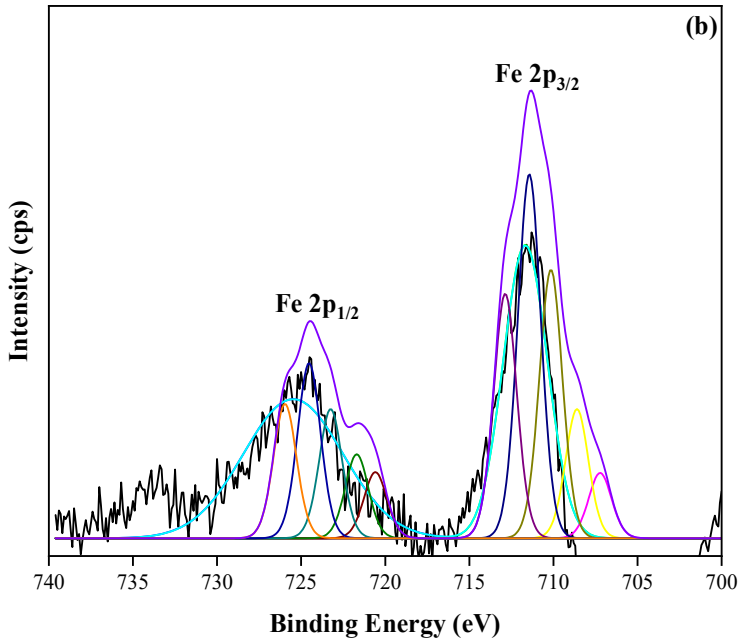

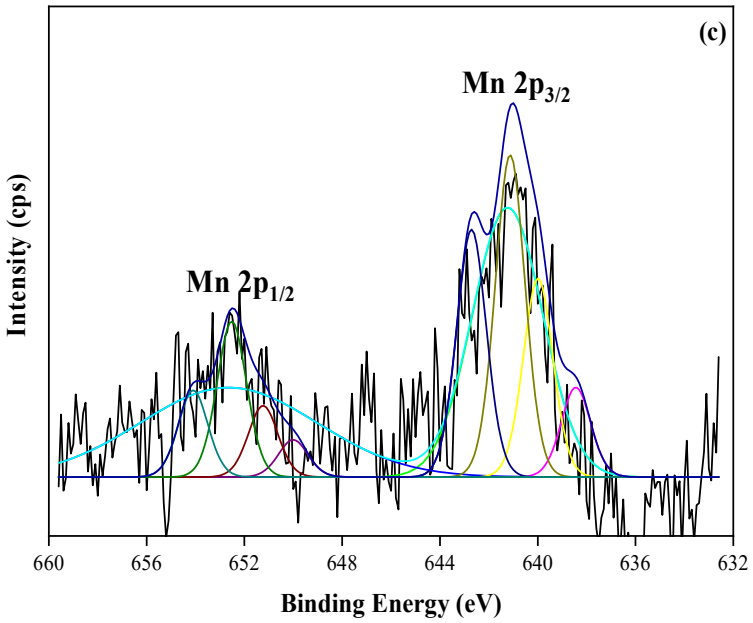
(c)
Mn 2p3/2
Mn 2p1/2
Intensity (cps)
660
656
652
648
644
640
636
632
Binding Energy (eV)

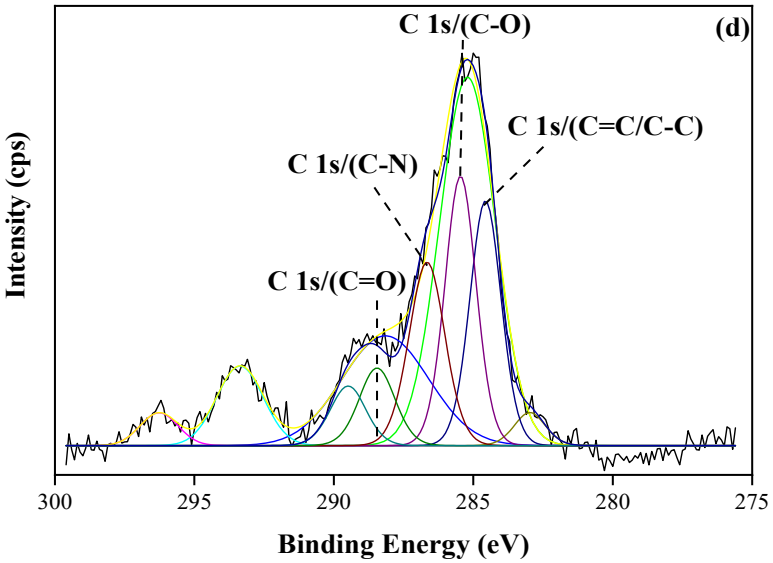
(d)
C 1s/(C-O)
C 1s/(C=C/C-C)
C 1s/(C-N)
C 1s/(C=O)
Intensity (cps)
300
295
290
285
280
275
Binding Energy (eV)

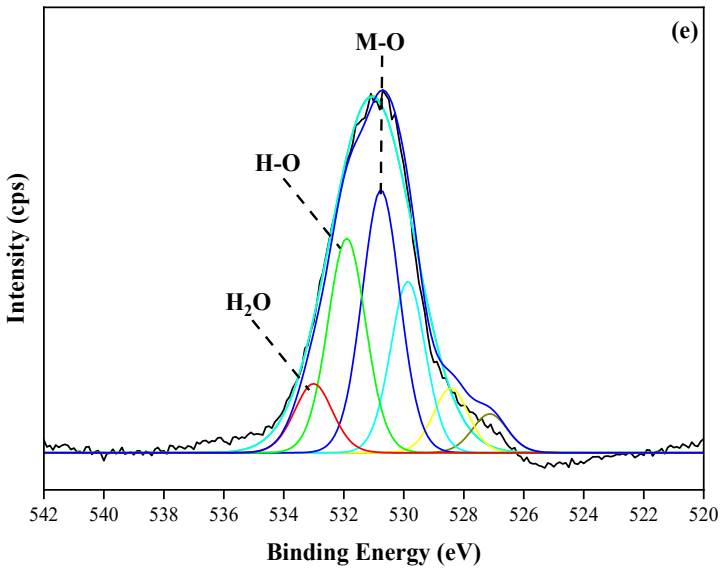

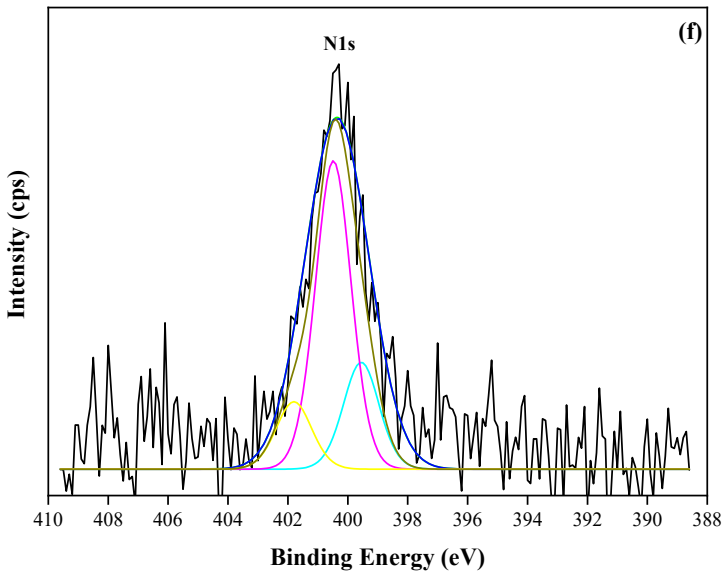

Fig. 3.9 (a) Survey XPS spectra of EDTA-FMHC-700; High resolution XPS (b) Fe2p, (c) Mn2p, (d) C1s, (e) O1s and (f) N1s peaks fitting of EDTA-FMHC-700

The XPS was used to analyze the chemical identity of atoms on the EDTA-FMHC-700 surface in detail based on the difference in bond energy. The overall survey of elements from EDTA-FMHC-700 were shown in Fig. 3.9a. The presence of Fe, Mn, C, O and N in the spectrum were confirmed with the binding energy values at 711.6, 640.6, 285.6, 530.6 and 399.6 eV, respectively. As shown in Fig. 3.9b, the presence of iron phase of Fe_3O_4 in EDTA-FMHC-700 was indicated by the appearance of two peaks namely Fe $2p_{3/2}$ and Fe $2p_{1/2}$ at the binding energy values of 711.6 and 724.5 eV, respectively. This result was in accordance with the characteristics of Fe_3O_4 in previous reported literature (Cui et al., 2015, Yang et al., 2018b). At Fig. 3.9c, the characteristic peaks of Mn $2p_{3/2}$ and Mn $2p_{1/2}$ were centered on the binding energy values of 640.6 and 652.5 eV, respectively. These values were also in accordance with previous work (Ren et al., 2012, Xiong et al., 2017, Yin et al., 2018). This data was also in accordance with the data in Fig. (3.4-3.6) which confirm the formation of $MnFe_2O_4$ on the EDTA-FMHC-700 surface.

The deconvolution of C 1s peak in Fig. 3.9d exhibits that there were several peaks in the binding energy values of 284.6, 285.5, 286.7 and 288.5 eV which can be assigned to C=C/C-C, C-O, C-N and C=O bonds, respectively (Lv et al., 2018, Xu et al., 2018). Then, the deconvolution of O 1s peak in Fig. 3.9e shows four peaks at the binding energy values of 530.8, 531.9 and 533 eV according to M-O (M = Fe or Mn), hydroxyl groups (O-H) and H_2O which is chemically or physically adsorbed, respectively (Deng et al., 2017). As shown in Fig. 3.9f, the deconvolution of N1s peak consists of three peaks with the binding energy values located at 399.6, 400.5, and 401.8 eV, which related to $-CO-NH-$, $-CH_2-NH_2$ and N-H, respectively (Deng et al., 2017, Li et al., 2017, Xu et al., 2018). All the obtained data above confirmed that EDTA-FMHC-700 was successfully fabricated.

3.2.8 Fourier Transform Infrared (FTIR) Spectroscopy

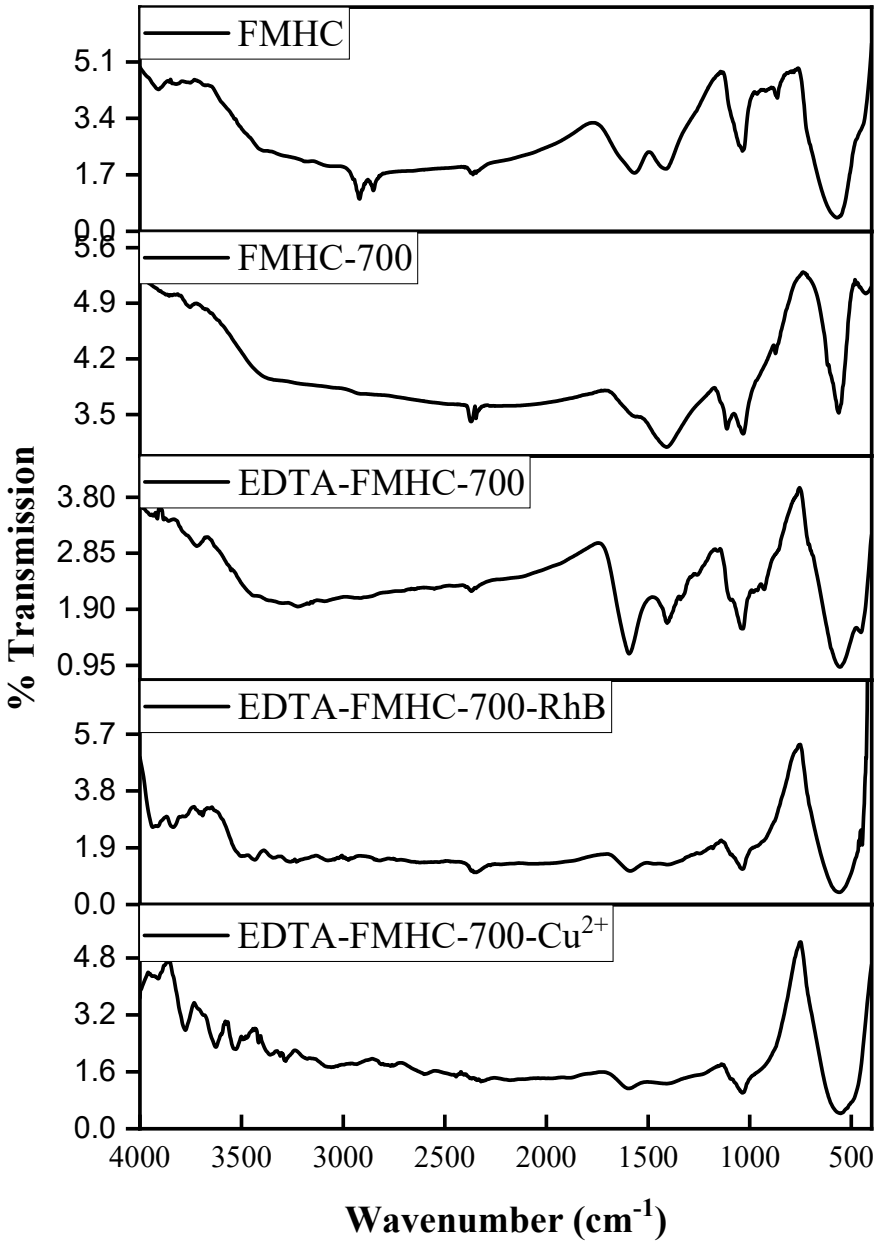

Fig. 3.10 FTIR spectra of FMHC, FMHC-700 and EDTA-FMHC-700 after adsorption with RhB and copper ion (Cu^{2+})

Table 3.2 Possible functionalized groups of FMHC, FMHC-700 and EDTA-FMHC before and after adsorption

Wavenumber (cm^{-1})	Assignment
FMHC	
570	Stretching vibration of Fe-O functional groups
864	Stretching vibration of N-H functional groups
1036	Bending vibration of C-OH functional groups
1412	Stretching vibration of C-O of carboxylic acid functional groups
1568	Stretching vibration of C=C aromatic functional groups
2906 and 2920	Stretching vibration of C-H aliphatic functional groups
3384	Stretching vibration of O-H from hydroxyl functional groups
FMHC-700	
562	Stretching vibration of Fe-O functional groups
874	Stretching vibration of N-H functional groups
1032	Bending vibration of C-OH functional groups
1112	Stretching vibration of C-N functional groups
1408	Stretching vibration of C-O of carboxylic acid functional groups
3340	Stretching vibration of O-H from hydroxyl functional groups
EDTA-FMHC-700	
556	Stretching vibration of Fe-O functional groups
1032	Bending vibration of C-OH functional groups
1406	Stretching vibration of C-O of carboxylic acid functional groups
1594	Stretching vibration of C=C aromatic functional groups
3222	Stretching vibration of O-H from hydroxyl and overlapping N-H functional groups

Wavenumber (cm^{-1})	Assignment
EDTA-FMHC-700-RhB	
560	Stretching vibration of Fe-O functional groups
1038	Bending vibration of C-OH functional groups
1588	Stretching vibration of C=C aromatic functional groups
EDTA-FMHC-700-Cu^{2+}	
552	Stretching vibration of Fe-O functional groups
1036	Bending vibration of C-OH functional groups
1596	Stretching vibration of C=C aromatic functional groups

As shown in Fig. 3.10, FTIR spectrum for FMHC and FMHC-700 shows characteristic peaks in the range 570-556 cm^{-1}, 874-864 cm^{-1}, 1412-1408 cm^{-1}, 3384-3340 cm^{-1} and 1036-1032 cm^{-1} which were assigned for stretching vibration of Fe-O, N-H, C-O, O-H groups and bending vibration of C-OH, respectively. For FMHC-700, several peak characteristics in 1568, 2906 and 2920 cm^{-1} disappeared which were assigned to bending vibration and vibration stretching of N-H and C-H aliphatic functional groups, respectively. In addition, the emergence of a new functional group on FMHC-700 at 1112 cm^{-1} which was assigned to the C-N functional group as a result of the activation process of FMHC which changes the functional groups and crystal plane of FMHC, these results were in accordance with the data from Table 3.1 and Fig. 3.6. Whereas in EDTA-FMHC-700, the appearance of a characteristic peak at 1594 cm^{-1} and the broad peaks at 3222 cm^{-1} were indicated as the C=C aromatic and the overlapping of N-H amide functional groups. These was in accordance with the data from Fig. 3.9 which prove that EDTA has successfully coated on the surface of FMHC-700.

Furthermore, some characteristic peaks for EDTA-FMHC-700 experienced a shift after the adsorption of RhB and copper ion (Cu^{2+}). For RhB adsorption, the characteristic peaks shift occurred at 556 to 560 cm^{-1}, 1032 to 1038 cm^{-1}, 1594 to 1588 cm^{-1} which were characterized as the stretching vibration of Fe-O functional groups and the bending vibrations of C-OH and the stretching vibration of C=C aromatic functional groups, respectively. While for copper ion (Cu^{2+}) adsorption, the characteristic peaks

shift occurred at 556 to 552 cm^{-1}, 1032 to 1036 cm^{-1}, 1594 to 1596 cm^{-1} which were characterized as the stretching vibration of Fe-O functional groups, the bending vibrations of C-OH and the stretching vibration of C=C aromatic functional groups, respectively. Moreover, the characteristic peaks at 1406 and 3222 cm^{-1} disappear which were assigned to stretching vibration of the C-O carboxylic acid functional groups and the O-H hydroxyl as well as the N-H amide functional groups, respectively. These results have confirm that RhB and copper ion (Cu^{2+}) have been adsorbed on EDTA-FMHC-700.

3.3 Adsorption Studies of Rhodamine B, ibuprofen and copper ion (Cu^{2+})

The synthesized EDTA-FMHC-700 was used to remove several pollutants such as Rhodamine B, copper ion (Cu^{2+}) and ibuprofen in aqueous solution through the adsorption process. Several factors that affect the adsorption process such as contact time and concentration, adsorbent weight, solution pH and temperature were studied to investigate the kinetics and isotherms model of the adsorption. The amount of adsorbed substance is the important factor to determine the adsorption capacity (q_e) and the percentage of removal efficiency ($\% R$) of the adsorbent. Experimental data related to the adsorption mechanisms of RhB, copper ion (Cu^{2+}) and IBP on the adsorbent surface are described using Langmuir, Freundlich and Temkin isotherm models.

The time-dependent of adsorption were used for kinetics studies for RhB, copper ion (Cu^{2+}) and IBP removal. In this work, two types of kinetic models such as pseudo first order and pseudo second order were used to study the dynamics and mechanisms in the reaction. The equations for the two types of kinetic models are presented in Eq. (3-4):

Pseudo first order: $\ln\ (q_e - q_t) = \ln\ q_e - k_1 t$ (3)

Pseudo second order: $\frac{t}{q_t} = \frac{1}{K_2 q_e^2} + \frac{t}{q_e}$ (4)

Where q_t is the amount of molecules adsorbed at specified time t, k_1 and k_2 are pseudo first order rate constant (min^{-1}) and pseudo second order rate constant ($g.mg^{-1}.min^{-1}$), respectively.

The Langmuir isotherm model assumes that the adsorption process occurs as monolayer and the interaction between the adsorbate molecule and the adsorbent surface have the same affinity. Therefore, there is no adsorption for the next layer after monolayer adsorption is reached on the adsorbent surface (Ghosal and Gupta, 2017). The non-linear and linear equations for the Langmuir isotherm model are shown in Eq. (5-6), respectively:

$$q_e = \frac{q_m K_L C_e}{1+K_L C_e} \quad (5)$$

$$\frac{C_e}{q_e} = \frac{1}{q_m K_L} + \frac{C_e}{q_m} \quad (6)$$

Where K_L and q_m refer to Langmuir constants which indicate the maximum number of substance molecules adsorbed on the adsorbent ($mg.g^{-1}$) and adsorption free energy ($L.mg^{-1}$). The dimensionless separation factor (R_L) was determined to show the suitability of the experimental data with the Langmuir isotherm model, as well as indicates that the adsorption nature become irreversible ($R_L = 0$), favourable ($0 < R_L < 1$), linear ($R_L = 1$) or unfavourable ($R_L > 1$), as indicate in Eq. (7) (Hayeeye et al., 2017):

$$R_L = \frac{1}{(1+K_L C_0)} \quad (7)$$

Alike with Langmuir isotherm model, Freundlich isotherm model assumes that the number of molecules of substances absorbed on the surface of the adsorbent increases gradually (multilayer adsorption). Linear equation can be used to identify the compatibility of experimental data with the Freundlich isotherm model. If the experimental data shows a correlation coefficient (R^2) that is large enough then the adsorption process is considered match with this isotherm model (Chung et al., 2015). The non-linear and linear forms of the Freundlich isotherm model are shown in Eq. (8-9):

$$q_e = K_F C_e^{1/n} \quad (8)$$

$$Log\ q_e = \frac{1}{n} \log\ C_e + Log\ K_F \quad (9)$$

Where n and K_F are Freundlich constants related to adsorption intensity and adsorption capacity ($(mg.g^{-1}).(L.mg^{-1})^{1/n}$), respectively.

The Temkin isotherm model describes the energy distribution uniformly on heterogeneous active sides (Inyinbor et al., 2016). The non-linear and linear forms of the Temkin isotherm model are shown in Eq. (10-11):

$$q_e = \frac{RT}{B_T} \ln K_T C_e \quad (10)$$

$$q_e = B_T \ln K_T + B_T \ln C_e \quad (11)$$

Where K_T and B_T are the equilibrium binding constant ($L.mg^{-1}$) and the adsorption heat ($J.mol^{-1}$), R is the molar gas constant (8.314 $J.mol^{-1}.K^{-1}$) and T is temperature (K).

3.3.1 Adsorption study of Rhodamine B (RhB)

The RhB adsorption process in an aqueous solution was carried out at a natural pH which was in the range pH 3.5-4.3.The maximum adsorption capacity and adsorption rate were investigated through several parameters that affect to RhB adsorption in the batch experiment. The difference of the RhB concentration in the aqueous solution before and after adsorption was measured using a spectrophotometric method at the maximum wavelength of 554 nm.

3.3.1.1 Effect of adsorbent weight on RhB adsorption

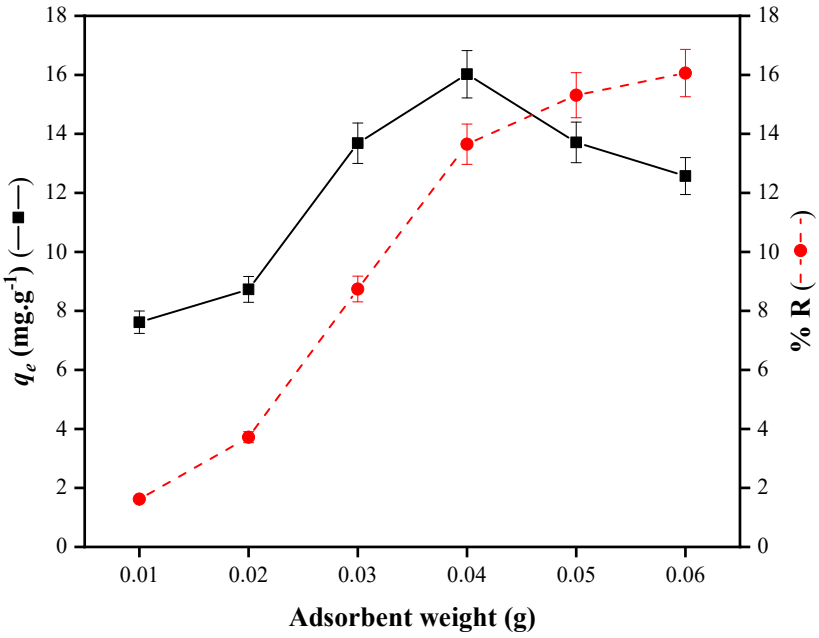

Fig. 3.11 Effect of adsorbent weight for RhB adsorption (C_0 = 100 mg.L^{-1}, $W_{adsorbent}$ = 0.01-0.06 g, V = 50 mL, natural pH, and T = 30^{o}C)

To study the effect of adsorbent weight on RhB adsorption, the weight of EDTA-FMHC-700 was varied from 0.01 to 0.06 g. As shown in Fig. 3.11, The increase of q_e and % R was offset by the increase of the adsorbent weight, and the maximum value was achieved at the adsorbent weight of 0.04 g. Increasing the value of q_e and % R can be caused by increasing the number of active sides on the surface of EDTA-FMHC-700 such as hydroxyl, carboxyl and amine functional groups (Naseem et al., 2018). After reaching the maximum condition at 0.04 g, decreasing in adsorption capacity value (q_e) may be caused by the number of RhB molecules adsorbed fulfilling all the available active sides on the EDTA-FMHC-700 surface. Therefore, the number of unadsorbed RhB molecules remains constant even with the increase of the adsorbent weight. At the weight of 0.04 g, the maximum adsorption capacity of EDTA-FMHC-700 for RhB was 16.02 mg.g^{-1}. The effect of increasing the weight of the adsorbent on the adsorption capacity value (q_e) was also consistent with previous reported literature (da Silva Lacerda et al., 2015, Hayeeye et al., 2017, Sukriti et al., 2017).

3.3.1.2 Effect of solution pH on RhB adsorption

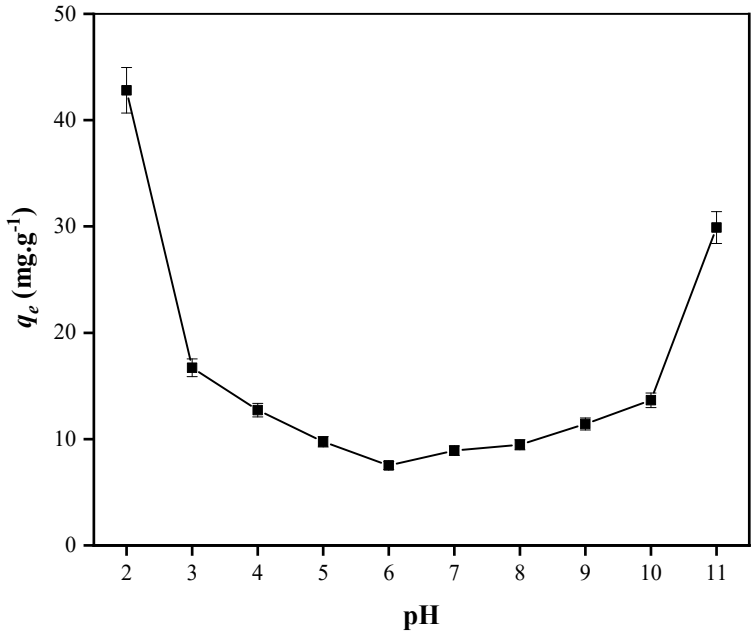

Fig. 3.12 Effect of solution pH for RhB adsorption (C_0 = 100 mg.L^{-1}, $W_{adsorbent}$ = 0.04 g, V = 50 mL, pH = 2-11, and T = 30^{o}C)

The effect of pH on RhB adsorption was carried out in the pH range 2-11, as indicated in Fig. 3.12. The EDTA-FMHC-700 shows the optimal adsorption capacity for RhB which was 42.82 mg.g^{-1} at pH 2. At low pH, excess hydrogen ions were likely to experience electrostatic attraction interactions with the amine functional group of EDTA on the EDTA-FMHC-700 surface, giving rise to a new active sides. The hydrogen bound to nitrogen atoms interacts with oxygen function groups (-O-) on RhB molecules through hydrogen bonding so that the number of adsorbed RhB molecules at low pH increases. Whereas in the range pH of 7-11, increasing in adsorption capacity was possible due to increasing in the amount of hydroxyl ions in the solution where the surface charge of EDTA-FMHC-700 tend to be negative and resulting in electrostatic attraction between adsorbent surface and quaternary amine positive charge (N^+R_3) of the RhB molecule. Furthermore, the adsorption of RhB at natural pH was preferable because it prevent the negative impacts to the environment.

3.3.1.3 Kinetics study of RhB adsorption

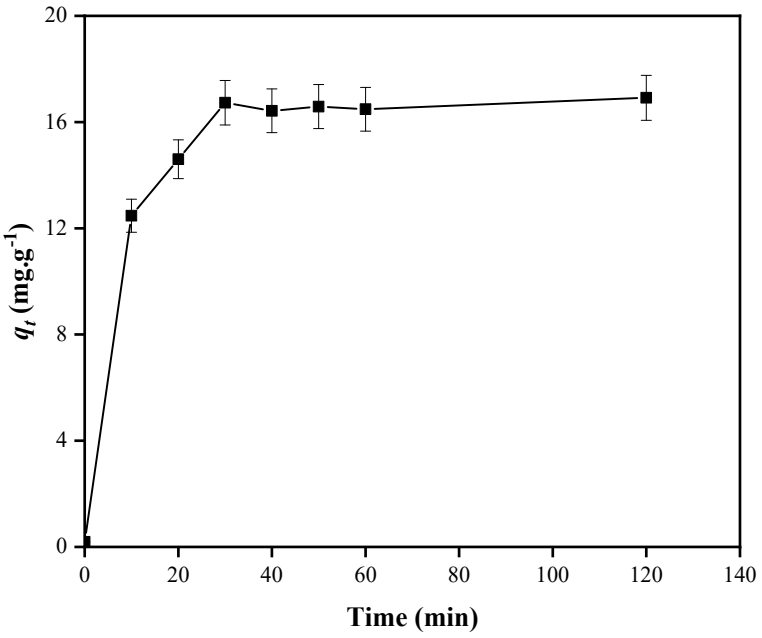

Fig. 3.13 Effect of contact time for the RhB adsorption (C_0 = 100 mg.L^{-1}, $W_{adsorbent}$ = 0.04 g, V = 50 mL, natural pH, and T = 30°C)

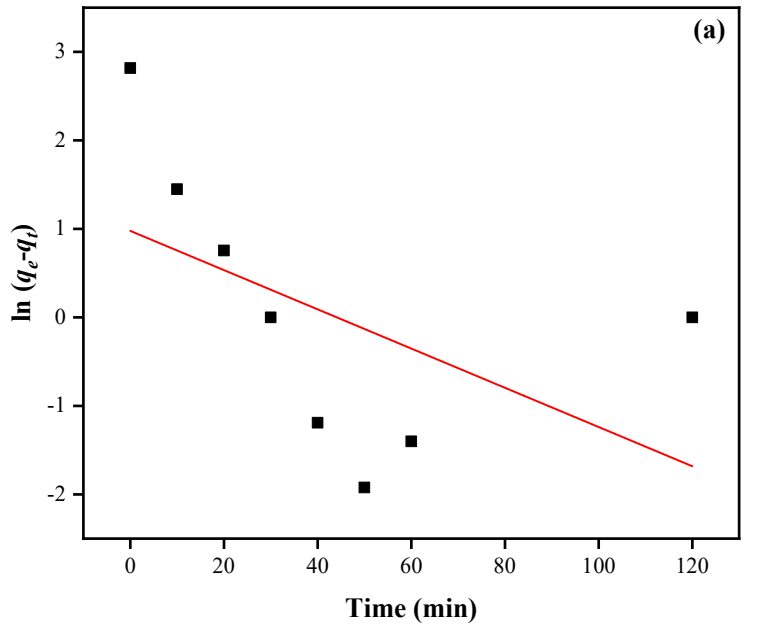

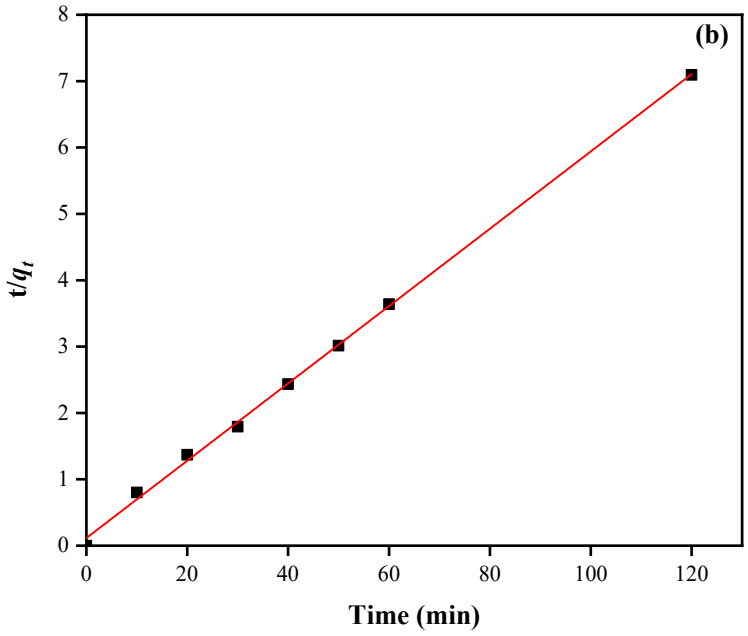

Fig. 3.14 Fitting of kinetic models by (a) pseudo first order and (b) pseudo second order for RhB adsorption (C_0 = 100 mg.L^{-1}, $W_{adsorbent}$ = 0.04 g, V = 50 mL, natural pH, and T = 30°C).

Table 3.3 Kinetics parameters for RhB adsorption by EDTA-FMHC-700 (C_0 = 100 mg.L^{-1}, $W_{adsorbent}$ = 0.04 g, V = 50 mL, natural pH, and T = 30°C).

Kinetics Model	**Parameters**	**Kinetics Model**	**Parameters**
Pseudo First Order	$q_{e\text{-}experiment}$ = 16.73 mg.g^{-1} q_e = 2.66 mg.g^{-1}	Pseudo Second Order	$q_{e\text{-}experiment}$ = 16.73 mg.g^{-1} q_e = 17.15 mg.g^{-1}
	k_1 = 2.2 x 10^{-2} min^{-1}		k_2 = 2.9 x 10^{-2} g.mg^{-1}.min^{-1}
	R^2 = 0.2752		R^2 = 0.9989

To determine the equilibrium time in the RhB adsorption, the EDTA-FMHC-700 was reacted with RhB solution for 120 min to ensure the adsorption process has

reached equilibrium condition, as shown at Fig. 3.13. The adsorption rate of the RhB by EDTA-FMHC-700 increased rapidly in the first 10 minutes, then reached equilibrium condition within 30 minutes. Increasing adsorption rate was probably caused by the amount of active side abundant on the surface of EDTA-FMHC-700 at the initial condition, then gradually slows down as an indication that the available active side has bounded with the RhB molecules until it reaches equilibrium. In this work, pseudo first order and pseudo second order were used as kinetic models to be matched with experimental data, as seen in Fig. 3.14(a-b). Based on data from the kinetics model parameters tabulated in Table 3.3, the relatively closeness of the value between the adsorption capacity of the experiment and the model as well as the higher correlation coefficient value (R^2) has confirmed that the adsorption of RhB by EDTA-FMHC-700 matched with the pseudo second order kinetics model.

3.3.1.4 Isotherms study of RhB adsorption

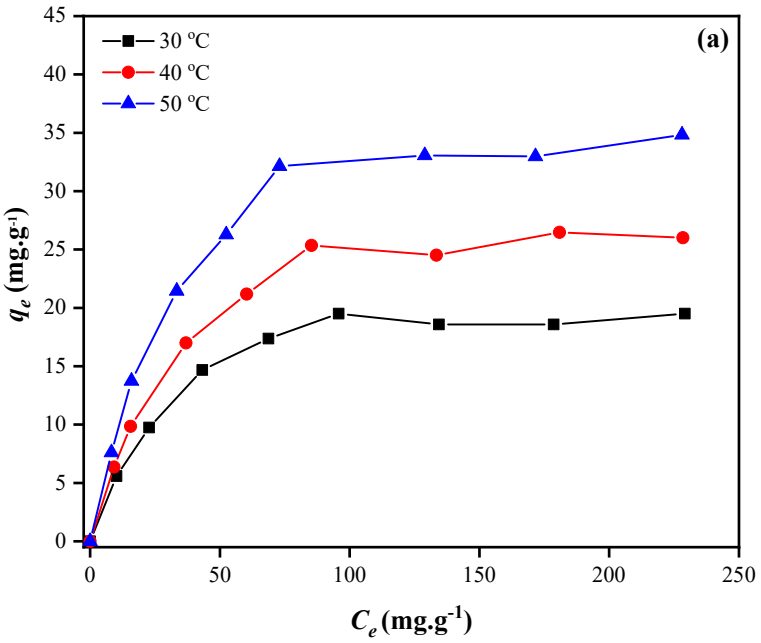

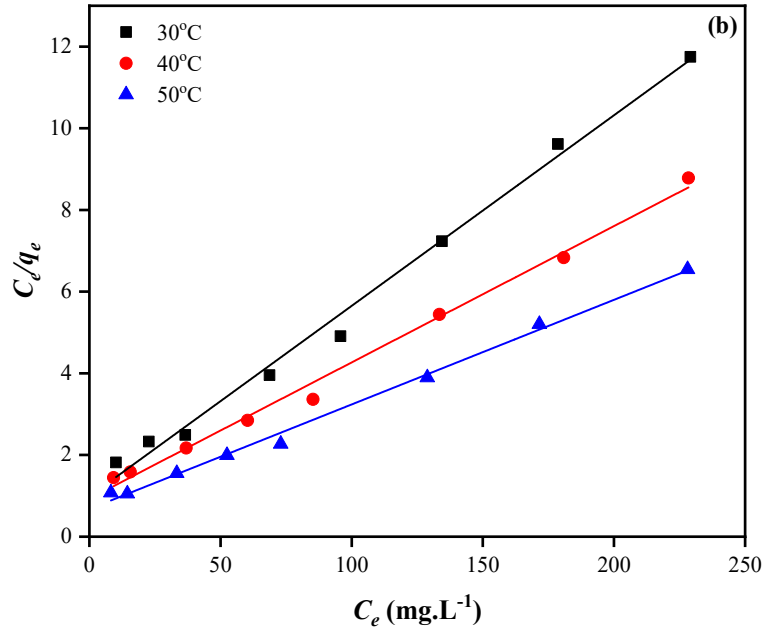
(b)
30°C
40°C
50°C
C_e/q_e
C_e (mg.L^{-1})
0
2
4
6
8
10
12
0
50
100
150
200
250

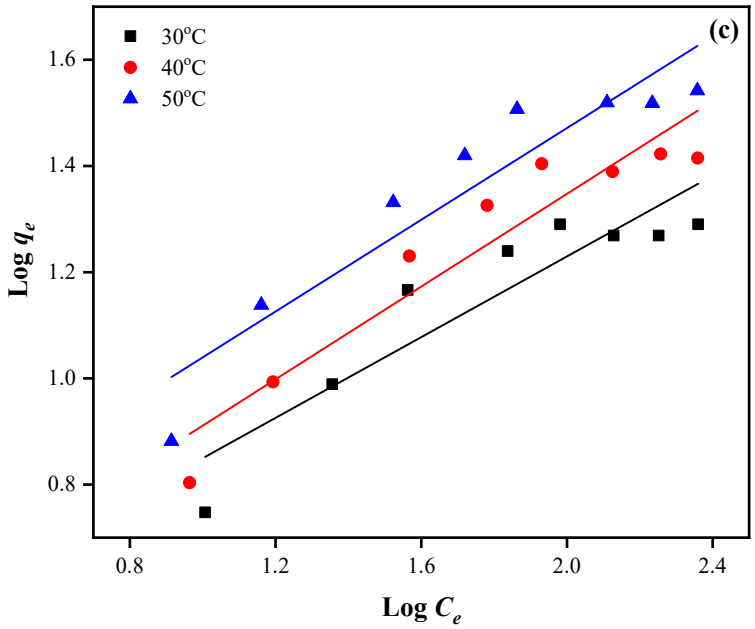
(c)
30°C
40°C
50°C
Log q_e
Log C_e
0.8
1.0
1.2
1.4
1.6
0.8
1.2
1.6
2.0
2.4

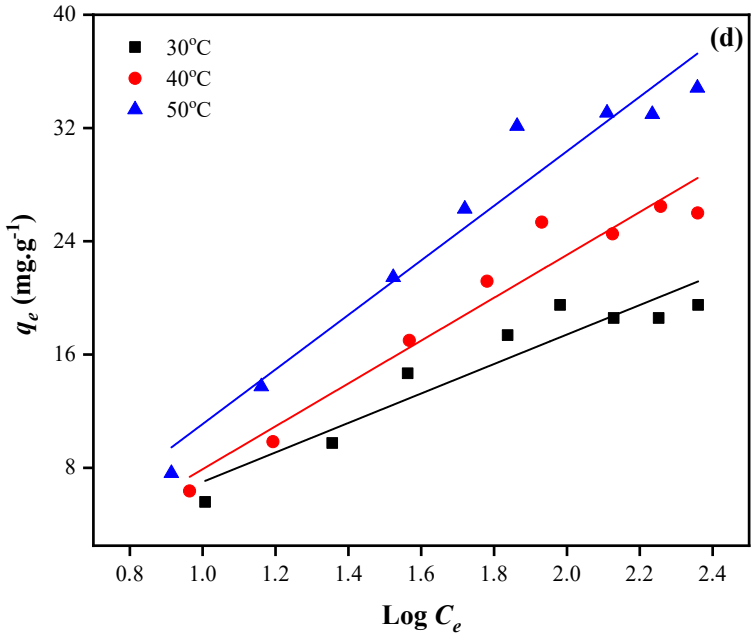

Fig. 3.15 (a) Adsorption isotherms of RhB on EDTA-FMHC-700 at various temperatures, (b) Langmuir, (c) Freundlich and (d) Temkin isotherm models for the adsorption (C_0 = 10-250 mg.L^{-1}, $W_{adsorbent}$ = 0.04 g, V = 50 mL, natural pH, and T = 30-50°C).

Table 3.4 Isotherm models parameters for the adsorption of RhB by EDTA-FMHC-700 (C_0 = 10-250 mg.L^{-1}, $W_{adsorbent}$ = 0.04 g, V = 50 mL, natural pH, and T = 30-50°C).

Temperature	**Isotherm Models**		
	Langmuir	**Freundlich**	**Temkin**
30°C	q_m = 21.41 mg.g^{-1} K_L = 0.0474 L.mg^{-1} R^2 = 0.9927	K_F = 2.95 L.mg^{-1} n = 2.63 R^2 = 0.8464	B_T = 10.41 J.mol^{-1} K_T = 0.72 L.mg^{-1} R^2 = 0.8966

Temperature	Isotherm Models		
	Langmuir	**Freundlich**	**Temkin**
40ºC	q_m = 29.94 mg.g^{-1} K_L = 0.0359 L.mg^{-1} R^2 = 0.9937	K_F = 2.98 L.mg^{-1} n = 2.29 R^2 = 0.9029	B_T = 15.14 J.mol^{-1} K_T = 0.62 L.mg^{-1} R^2 = 0.9479
50ºC	q_m = 39.06 mg.g^{-1} K_L = 0.0378 L.mg^{-1} R^2 = 0.9953	K_F = 4.05 L.mg^{-1} n = 2.31 R^2 = 0.8874	B_T = 19.27 J.mol^{-1} K_T = 0.65 L.mg^{-1} R^2 = 0.9517

The fits isotherm model at constant temperature was studied to determine the effect of RhB concentration on the adsorption capacity of EDTA-FMHC-700 through predictive calculation. The obtained results from Fig. 3.15(a-d) and Table 3.4 exhibit that the Langmuir isotherm model gives the best fits with experimental data based on the correlation coefficient value (R^2) which is higher than the Freundlich and Temkin isotherm models at various temperatures. These results designate that the mechanism of RhB adsorption by EDTA-FMHC-700 following the monolayer adsorption process. For the concentration of RhB at 10-250 mg.L^{-1}, the obtained R_L values were in the range of 0.07-0.67 which represents that the Langmuir isotherm model was more favorable for RhB adsorption (Ibrahim et al., 2019, Maniyazagan et al., 2019). Furthermore, the maximum adsorption capacity of EDTA-FMHC-700 (q_m) against RhB was more eminent than polystyrene/Fe_3O_4/GO (Wang et al., 2012a), magnetite/RGO (Sun et al., 2011) and $MnFe_2O_4$ (Lamdab et al., 2018). The maximum adsorption capacity of EDTA-FMHC-700 compare with various types of the reported magnetic adsorbents for RhB adsorption, were shown in Table 3.5.

Table 3.5 Comparison of the maximum adsorption capacity (q_{max}) of EDTA-FMHC-700 with various types of magnetic adsorbents for RhB adsorption.

Adsorbent	pH	t_{eq}[a] (min)	q_{max} (mg.g^{-1})	Ref.
$MnFe_2O_4$	10.5	25	9.30	(Lamdab et al., 2018)
Polystyrene/Fe_3O_4/GO	7	1440	13.8	(Wang et al., 2012a)
Magnetite/RGO	7	30	13.5	(Sun et al., 2011)
L-Serine-Fe_3O_4 MNPs	7.4	180	6.82	(Belachew et al., 2017)
ZnFe-NC	7	20	12.1	(Konicki et al., 2017)
Magnetic Lignin-based hollow microspheres	Natural pH	180	17.62	(Li et al., 2016)
EDTA-FMHC-700	3.8	30	21.41	This study

[a] t_{eq} is the equilibrium time for the adsorption of RhB

3.3.1.5 Regeneration Study for RhB adsorption

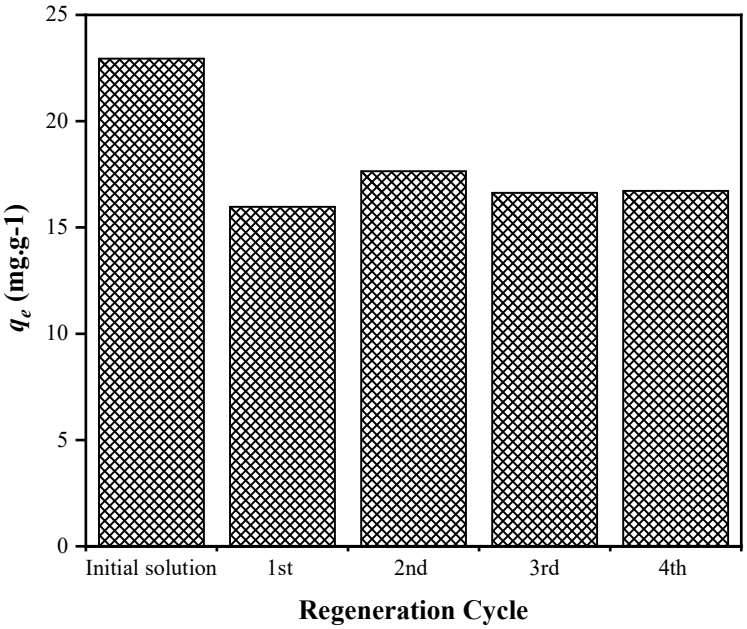

Fig. 3.16 Adsorption capacity of RhB by EDTA-FMHC-700 in four successive cycles (C_0 = 100 mg.L^{-1}, $W_{adsorbent}$ = 0.04 g, V = 50 mL, natural pH, and T = 30°C)

To follow the industry perspective, regeneration studies were one of the important factors to investigate the cost, effectiveness and efficiency of using adsorbents. For this regeneration, the loaded RhB in EDTA-FMHC-700 was separated from the solution using an external magnet, then washed using acetone followed by DI water. Then it dried in the oven at 100ºC for 5 h. This process was conducted for each adsorption-desorption process. As shown at Fig. 3.16, the adsorption capacity of RhB by EDTA-FMHC-700 was 22.94 $mg.g^{-1}$ at the initial condition. After four consecutive cycles, the RhB adsorption capacity decreased from 22.94 to 16.72 $mg.g^{-1}$ but the performance still maintained as much as 75% of the initial condition. EDTA-FMHC-700 performance shows good regeneration, effectiveness and efficiency that can be considered to be applied for industrial purposes as well as environmental remediation processes.

3.3.1.6 The proposed mechanism on the adsorption of RhB

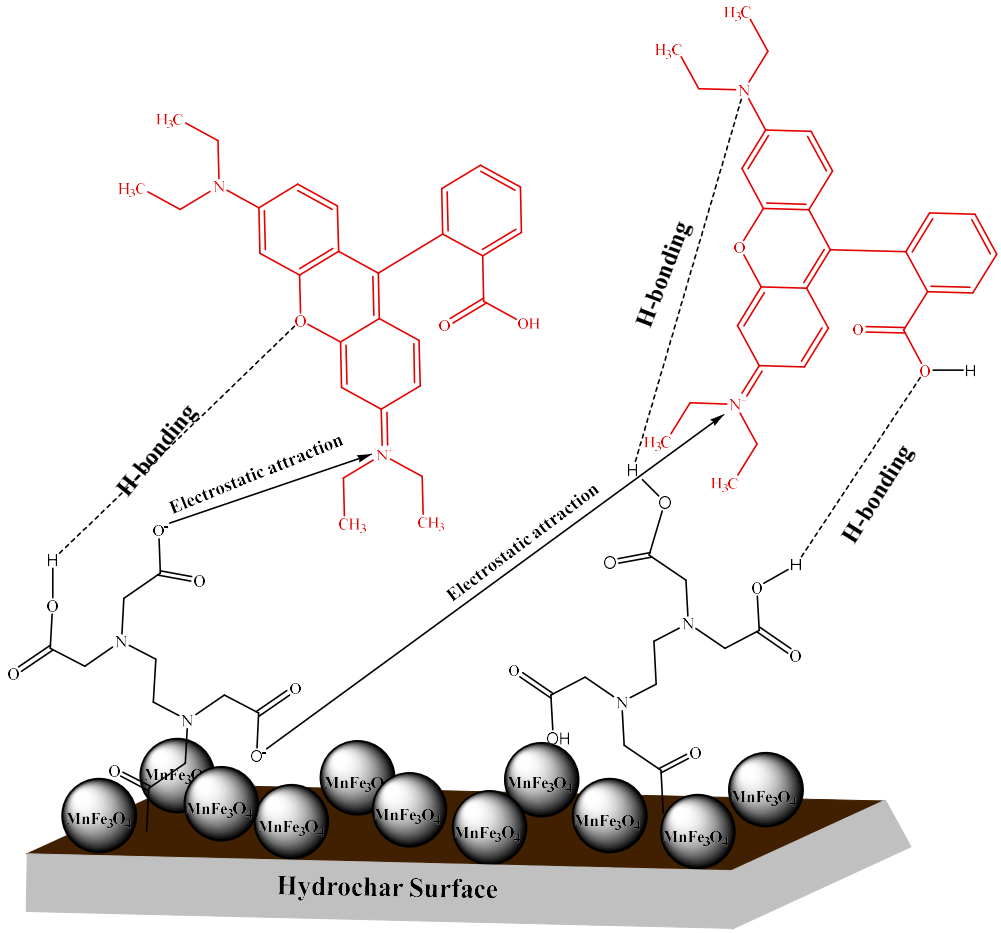

Fig. 3.17 The proposed mechanism of RhB adsorption onto EDTA-FMHC-700 (C_0 = 100 mg.L^{-1}, $W_{adsorbent}$ = 0.04 g, V = 50 mL, natural pH (3.8) and T = 30ºC)

The adsorption of RhB on EDTA-FMHC-700 was carried out at the natural pH of RhB at the pH range of 3.5-4.3, so the RhB tends to be in its cationic form (Jiao et al., 2015). Chemisorption may have more role than physisorption in the RhB adsorption process. In the physisorption, the average pore diameter of the adsorbent (0.91 nm) that corresponds to the data from Fig. 3.7, a little difficult to let the RhB molecules with the ionic radius of 1.44 nm to enter the pores (Jiang and Huang, 2016).

While for chemisorption, the EDTA structure (H_4Y) will undergo a dissociation process at the natural pH of RhB solution (pH 3.8) into its ionic form (H_2Y^{2-}) according to the previous literature (Maketon et al., 2008). Therefore, the interaction between RhB molecules and the adsorbent surface tends to be dominated by electrostatic attraction

and hydrogen bonding. The electrostatic attraction occurs between the dissociated species of EDTA ($-COO^-$) and the positive charge of quaternary amine group (R_3N^+) from the RhB molecules. While hydrogen bonding occur between hydrogen atom from the -OH carboxylic acid functional groups in EDTA with both oxygen atom from ether (C-O-C) functional group and nitrogen atom from a secondary amine in the RhB molecules (Li et al., 2013, Punyapalakul et al., 2009). These results were also correspond to FTIR results in Fig. 3.10 and Table 3.2.

3.3.2 Adsorption study of copper ion (Cu^{2+})

The adsorption of copper ion (Cu^{2+}) in an aqueous solution was conducted in batch experiment at natural pH of copper ion (Cu^{2+}) solution which was the pH of 4.98-5.15. Some parameters which affect to the adsorption of copper ion (Cu^{2+}) such as initial concentration and contact time, adsorbent weight and solution pH were also studied. The concentration of copper ion (Cu^{2+}) in the aqueous solution before and after adsorption was measured using an inductively coupled plasma-optical emission spectrometer (ICP-OES).

3.3.2.1 Effect of adsorbent weight on copper ion (Cu^{2+}) adsorption

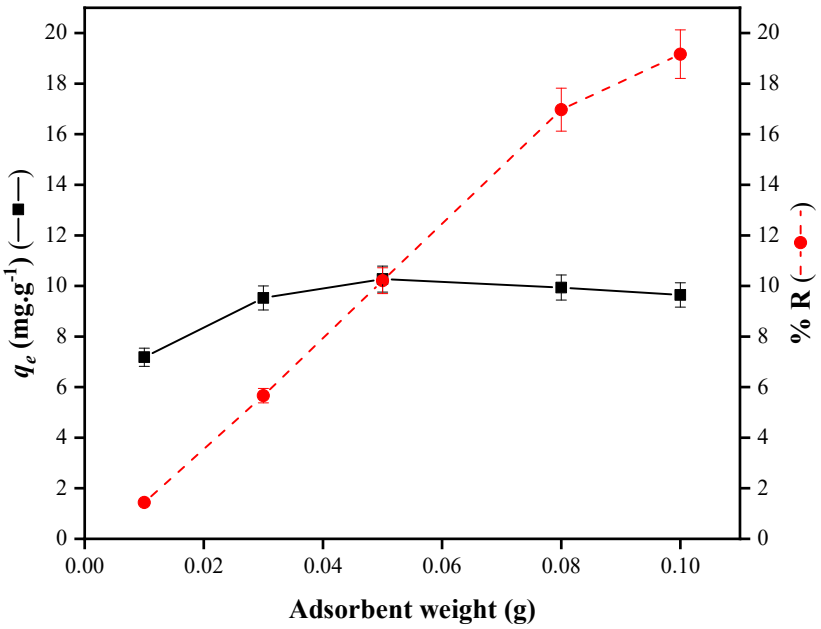

Fig. 3.18 Effect of adsorbent weight for the copper ion (Cu^{2+}) adsorption (C_0 = 100 mg.L^{-1}, $W_{adsorbent}$ = 0.01-0.1 g, V = 50 mL, natural pH, and T = 30°C)

The adsorption capacity (q_e) and removal efficiency (*% R*) were best found on the adsorbent weight of 0.05 g for the adsorption of copper ion (Cu^{2+}), as shown in Fig. 3.18. The maximum adsorption capacity (q_e) and removal efficiency (*% R*) of EDTA-FMHC-700 for copper ion (Cu^{2+}) were 10.27 mg.g^{-1} and 10.21%, respectively. The increasing of q_e and *% R* values can be caused by the large number of active sides on

the surface of EDTA-FMHC-700 at the initial conditions which can cause the increase in the chelating process of copper ions (Cu^{2+}) with the presence of EDTA on the adsorbent surface (Cui et al., 2015). After reaching the maximum condition at 0.05 g, the amount of unadsorbed copper ion (Cu^{2+}) remains constant even though the adsorbent weight increases.

3.3.2.2 Effect of solution pH on copper ion (Cu^{2+}) adsorption

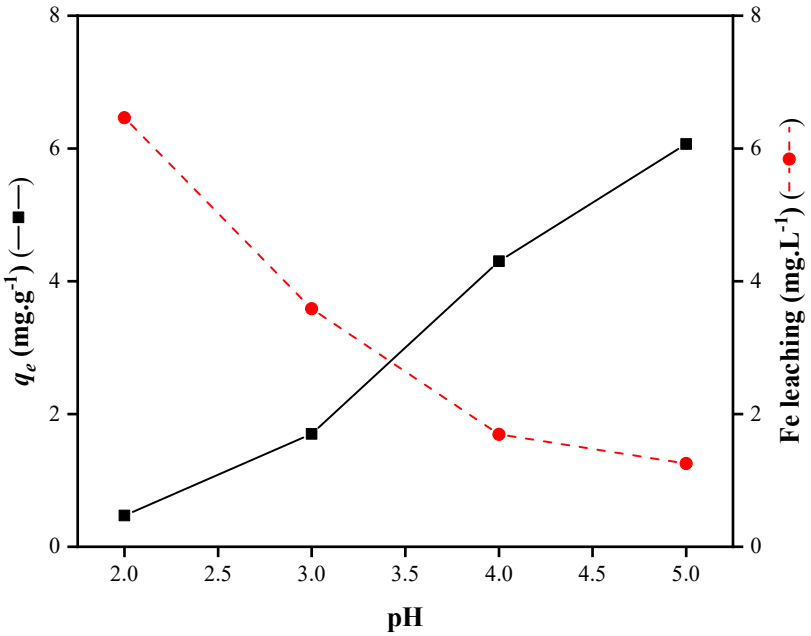

Fig. 3.19 Effect of solution pH for copper ion (Cu^{2+}) adsorption (C_0 = 100 mg.L^{-1}, $W_{adsorbent}$ = 0.05 g, V = 50 mL, pH = 2-5, and T = 30ºC)

In the adsorption of copper ion (Cu^{2+}), the protonation occurs at low pH value resulting in EDTA-FMHC-700 surface tends to be positively charged which cause repulsion interactions between R_2N^+ and Cu^{2+}, as shown in Fig. 3.19. Furthermore, the increase in pH value causes deprotonation on the EDTA-FMHC-700 surface so that the adsorbent surface tends to be more negative so increase the electrostatic attraction on Cu^{2+}. The estimation about the resistance of Fe content on EDTA-FMHC-700 at acid condition was one of the important factors to investigate the adsorbent performance, especially the magnetic properties. The effect of pH on Fe-leaching on EDTA-FMHC-

700 was also shown in Fig. 3.19. At strong acidic conditions, some particles of Fe_3O_4 from the adsorbent dissolved significantly in the solution because the bond between some Fe_3O_4 particles and the carbon fraction on the adsorbent surface became weak then finally broke. Hence, the adsorption of copper ion (Cu^{2+}) at natural pH was preferable because it prevents the Fe leaching and reduces the negative impacts to the environment.

3.3.2.3 Kinetics study of copper ion (Cu^{2+}) adsorption

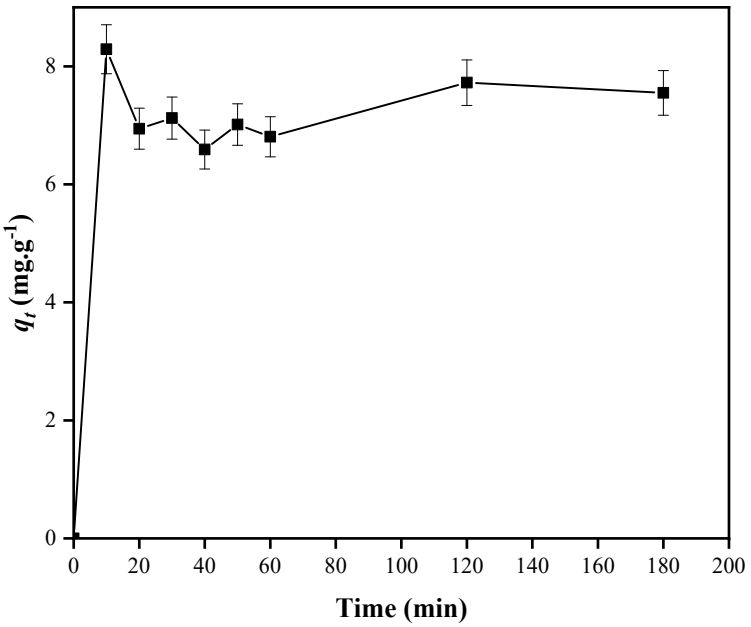

Fig. 3.20 Effect of contact time for copper ion (Cu^{2+}) adsorption (C_0 = 100 mg.L^{-1}, $W_{adsorbent}$ = 0.01-0.1 g, V = 50 mL, natural pH, and T = 30^{o}C)

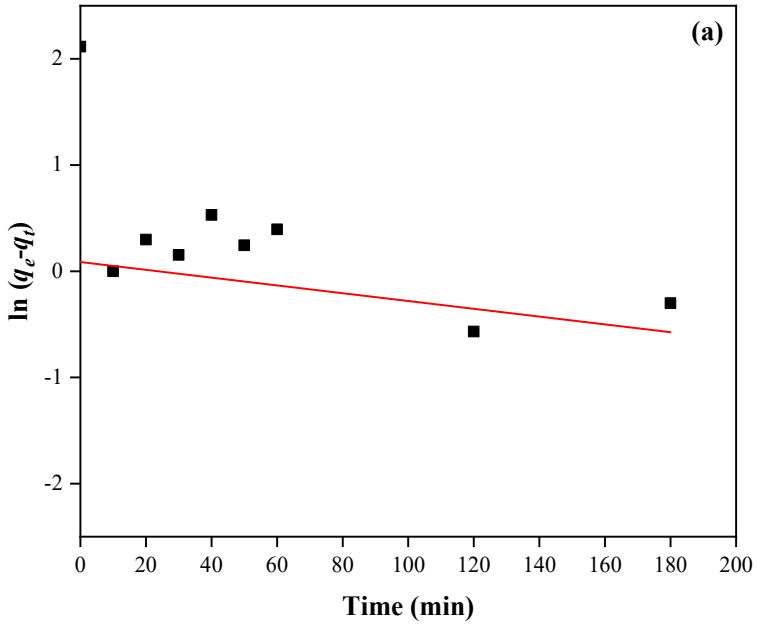
(a)
ln (q_e-q_t)
Time (min)

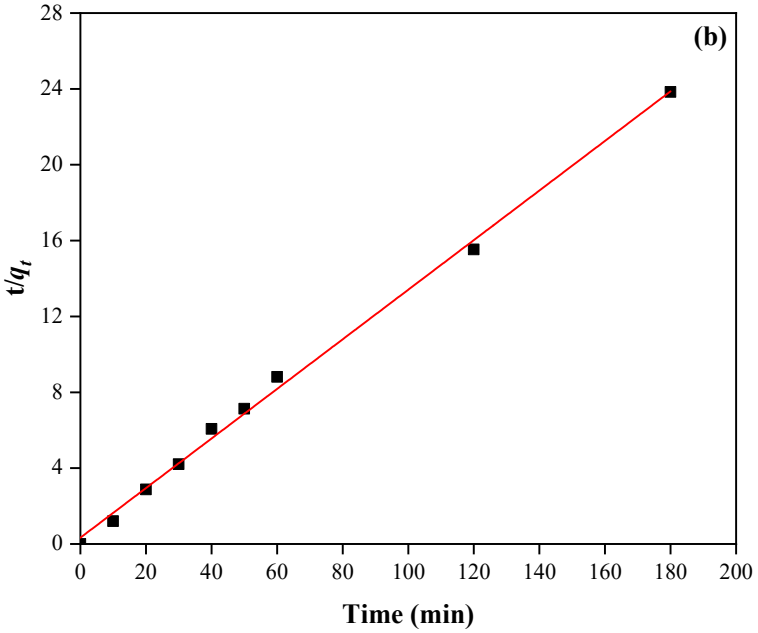
(b)
t/q_t
Time (min)

Fig. 3.21 Kinetic models by pseudo first order (a) and pseudo second order (b) for copper ion (Cu^{2+}) adsorption (C_0 = 100 mg.L^{-1}, $W_{adsorbent}$ = 0.05 g, V = 50 mL, natural pH, and T = 30ºC).

Table 3.6 Kinetics parameters for copper ion (Cu^{2+}) adsorption by EDTA-FMHC-700 (C_0 = 100 mg.L^{-1}, $W_{adsorbent}$ = 0.05 g, V = 50 mL, natural pH, and T = 30ºC).

Kinetics Model	**Parameters**	**Kinetics Model**	**Parameters**
Pseudo First Order	$q_{e\text{-}experiment}$ = 8.29 mg.g^{-1}	Pseudo Second Order	$q_{e\text{-}experiment}$ = 8.29 mg.g^{-1}
	q_e = 2.17 mg.g^{-1}		q_e = 7.64 mg.g^{-1}
	k_1 = 0.8 x 10^{-2} min^{-1}		k_2 = 5.1 x 10^{-2} g.mg^{-1}.min^{-1}
	R^2 = 0.3811		R^2 = 0.9973

As seen in Fig. 3.20, the adsorption of copper ion (Cu^{2+}) by EDTA-FMHC-700 was conducted for 120 min to confirm that the adsorption equilibrium was reached. It can be seen that the adsorption rate of copper ions (Cu^{2+}) was relatively fast and reach the equilibrium condition in the first 10 min. The addition of EDTA can act as the active side donor and chelating agent for copper ions which probably cause increasing in the adsorption rate of copper ion (Cu^{2+}) adsorption at the initial conditions. When the equilibrium conditions have been reached so the adsorption rate decreases gradually as the indication that all active sides have chelated with copper ions. Furthermore, the obtained experimental data will be fitted with one of the kinetics model, namely pseudo first order and pseudo second order kinetics model, as seen in Fig. 3.21(a-b). From the kinetics model parameters presented in Table 3.6, the adsorption capacity values which are obtained from the experiment data relatively similar with the adsorption capacity values from the pseudo second order kinetics model. This result was supported by the obtained linearity coefficient value (R^2), where the linearity coefficient value of the pseudo second order higher that pseudo first order. Hence, it can be confirmed that the

adsorption of copper ions (Cu^{2+}) by EDTA-FMHC-700 fits with the pseudo second order kinetics.

3.3.2.4 Isotherms study of copper ion (Cu^{2+}) adsorption

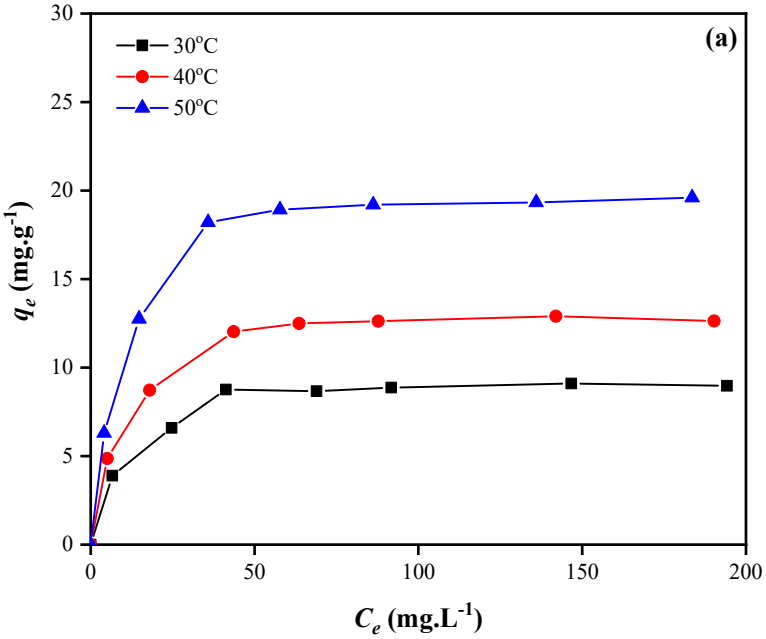

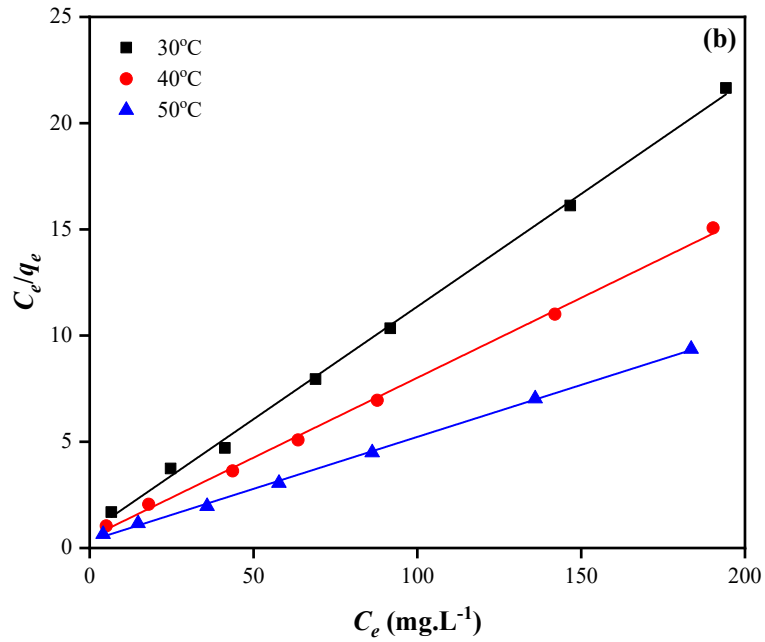

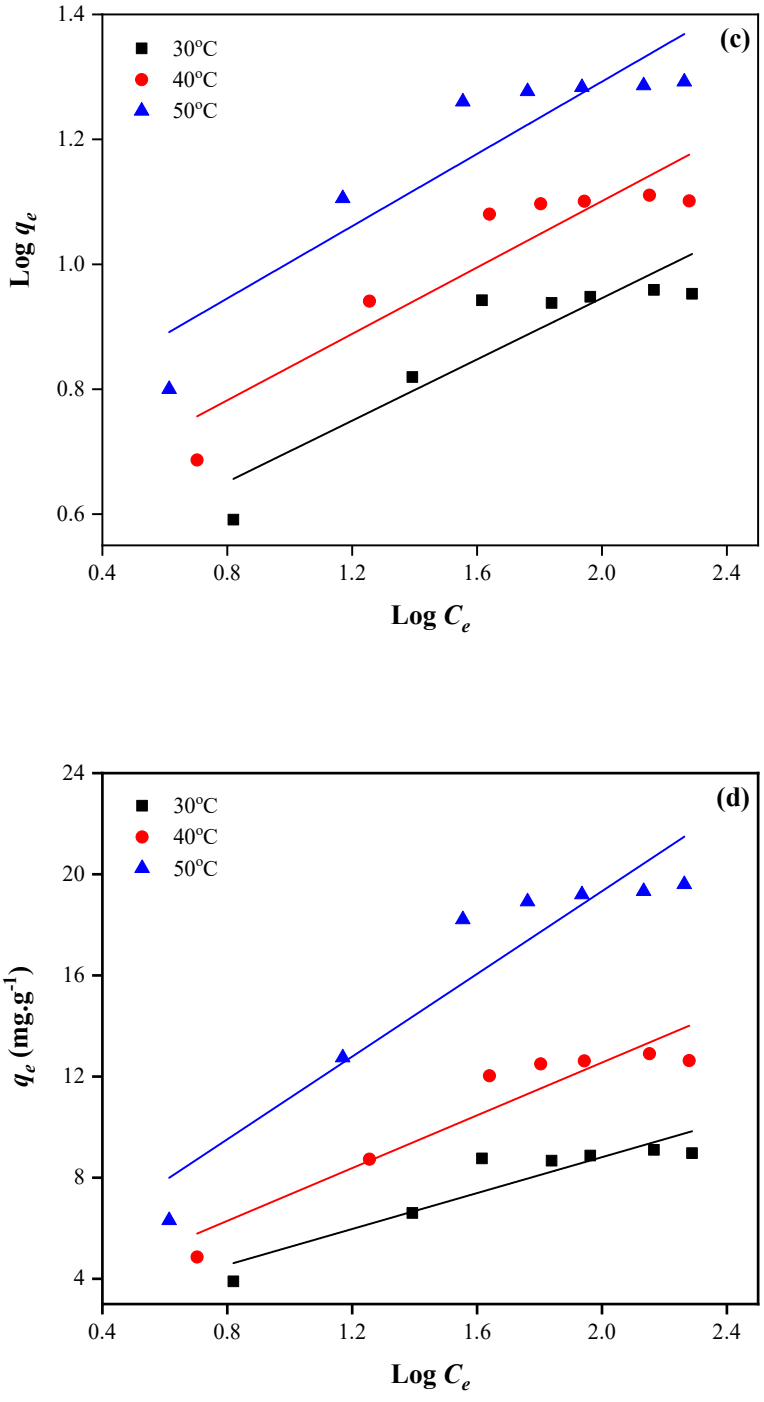

Fig. 3.22 (a) Adsorption isotherms of copper ion (Cu^{2+}) on EDTA-FMHC-700 at various temperatures, (b) Langmuir, (c) Freundlich and (d) Temkin isotherm models for the adsorption (C_0 = 10-200 mg.L^{-1}, $W_{adsorbent}$ = 0.05 g, V = 50 mL, natural pH, and T = 30-50°C).

Table 3.7 Isotherm models parameters for the adsorption of copper ion (Cu^{2+}) by EDTA-FMHC-700 (C_0 = 10-200 mg.L^{-1}, $W_{adsorbent}$ = 0.05 g, V = 50 mL, natural pH, and T = 30-50°C).

Temperature	Isotherm Models		
	Langmuir	**Freundlich**	**Temkin**
30°C	q_m = 9.43 mg.g^{-1} K_L = 0.1392 L.mg^{-1} R^2 = 0.9983	K_F = 2.85 L.mg^{-1} n = 4.08 R^2 = 0.8282	B_T = 3.55 J.mol^{-1} K_T = 1.62 L.mg^{-1} R^2 = 0.8531
40°C	q_m = 13.30 mg.g^{-1} K_L = 0.1526 L.mg^{-1} R^2 = 0.9984	K_F = 3.71 L.mg^{-1} n = 3.76 R^2 = 0.8592	B_T = 5.22 J.mol^{-1} K_T = 1.50 L.mg^{-1} R^2 = 0.8929
50°C	q_m = 20.45 mg.g^{-1} K_L = 0.1445 L.mg^{-1} R^2 = 0.9991	K_F = 5.17 L.mg^{-1} n = 3.46 R^2 = 0.8433	B_T = 8.18 J.mol^{-1} K_T = 1.44 L.mg^{-1} R^2 = 0.8909

Predictive calculation of the fits isotherm model were used to study the effect of copper ion (Cu^{2+}) concentration on the adsorption capacity of EDTA-FMHC-700. As shown in Fig. 3.22(a-d) and Table 3.7, the experimental data was fitted well with the Langmuir isotherm model based on the correlation coefficient value (R^2) which is higher than the Freundlich and Temkin isotherm models at various temperature, so that the adsorption of copper ions (Cu^{2+}) by EDTA-FMHC-700 follows the monolayer adsorption mechanism of the Langmuir isotherm model. For copper ion (Cu^{2+}) adsorption at the concentration of 10-200 mg.L^{-1}, the obtained R_L values were in the range of 0.03-0.41 which represents that the Langmuir isotherm model was more favorable for copper ion (Cu^{2+}) adsorption (Ojemaye et al., 2017). The maximum

adsorption capacity (q_m) of EDTA-FMHC-700 for copper ion (Cu^{2+}) adsorption compared to other adsorbents are shown in Table 3.8.

Table 3.8 Comparison of the maximum adsorption capacity (q_{max}) of EDTA-FMHC-700 with various type of magnetic adsorbents for copper ion (Cu^{2+}) adsorption.

Adsorbent	pH	t_{eq}[a] (min)	q_{max} ($mg.g^{-1}$)	Ref.
Fe_3O_4-EDTA	6.0	5	46.27	(Liu et al., 2013)
MNP-Maph	5.0	45	34.08	(Ojemaye et al., 2017)
Amino-functionalized magnetic nanoparticles	6.0	5	25.77	(Hao et al., 2010)
C-dots / Fe_3O_4 magnetic nanocomposites	6.0	~ 5	13.51	(Masoudi and Honarasa, 2018)
Oxidized mesoporous carbon-based magnetic composite	5.3	240	51.40	(Yi et al., 2019)
EDTA-FMHC-700	5.0	10	9.43	This study

[a] t_{eq} is the equilibrium time for the adsorption of copper ion (Cu^{2+})

3.3.2.5 Regeneration study for copper ion (Cu^{2+}) adsorption

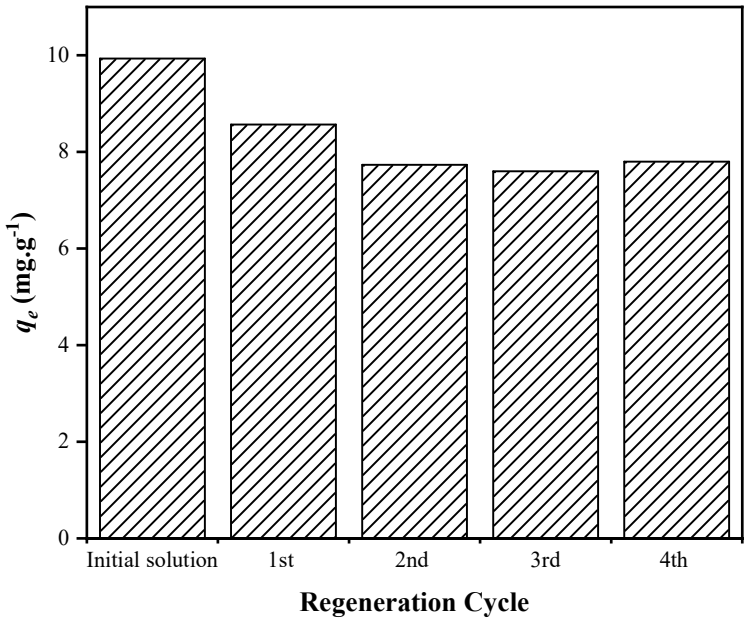

Fig. 3.23 Adsorption capacity of copper ion (Cu^{2+}) by EDTA-FMHC-700 in four successive cycles (C_0 = 100 mg.L^{-1}, $W_{adsorbent}$ = 0.05 g, V = 50 mL, natural pH, and T = 30^{o}C)

To examine the effectiveness and efficiency from the use of adsorbents, the adsorption-desorption process was carried out by separating copper ions loaded EDTA-FMHC-700 from the solution, then soaked with 0.1 M HCl for 1 h, washed with DI water then dried in the oven at 100^{o}C for 5 h. This process was performed in 4 consecutive cycles, where the obtained initial adsorption capacity was 9.93 mg.g^{-1}, as shown in Fig. 3.23. In the first cycle the adsorption capacity of copper ions (Cu^{2+}) decreased from 9.93 to 8.56 mg.g^{-1}. Then it decreased again with adsorption capacity of 7.73 mg.g^{-1} in the second cycle then stable until the fourth cycle. This reduced adsorption capacity was probably caused by the loss of several active sides of the adsorbent due to the desorption process using HCl. However, overall the EDTA-FMHC-700 can still maintain its performance up to 78.55% from the initial condition. The EDTA-FMHC-700 exhibits relatively good regeneration and stability so that can

be considered to be used for further application such as environmental remediation processes from heavy metals.

3.3.2.6 The proposed mechanism on the adsorption of copper ion (Cu^{2+})

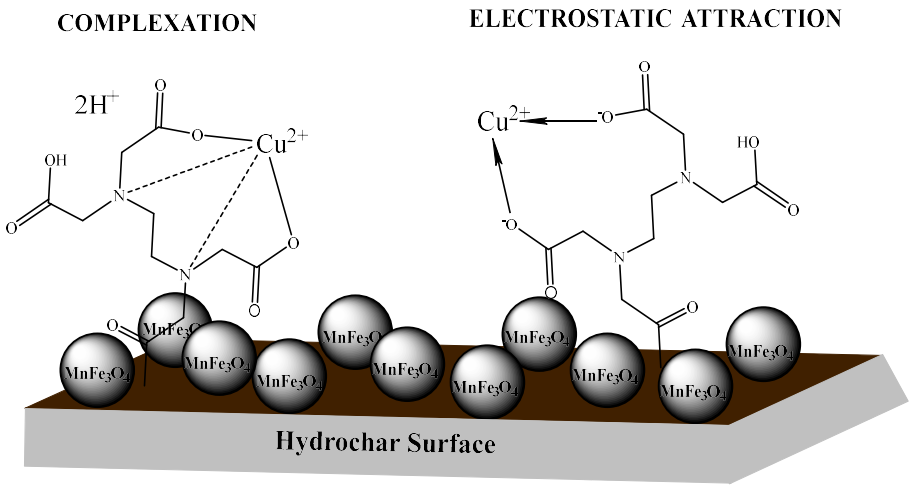

Fig. 3.24 The proposed mechanism of copper ion (Cu^{2+}) adsorption onto EDTA-FMHC-700 700 (C_0 = 100 mg.L^{-1}, $W_{adsorbent}$ = 0.05 g, V = 50 mL, natural pH (5.0) and T = 30°C).

The adsorption of copper ion (Cu^{2+}) on EDTA-FMHC-700 was carried out at the natural pH of copper ion (Cu^{2+}) solution at the pH range of 4.98-5.15. The combination of physisorption and chemisorption may play a role in the copper ion (Cu^{2+}) adsorption process. Similar with the RhB adsorption, physisorption occur between the copper ion (Cu^{2+}) and the surface pores of EDTA-FMHC-700 through van der Waals bonding. The radius of copper ion (Cu^{2+}), which is 0.14 nm, allows it to enter the adsorbent pores with the average pore diameter of 1.5 nm as shown in Fig. 3.7 (Xu et al., 2018).

For chemisorption, the complexation of copper ions (Cu^{2+}) with the functional groups of EDTA such as carboxylic acid (-COOH) and amine with lone pair electrons (–R-N:) was likely to dominate due to they can act as exchange site for metal ions. The lone electron pairs from amine functional groups (-R-N:) and the oxygen atom from the carboxylic acid functional group (-COOH) can bind to copper ions (Cu^{2+}) then release

two hydrogen ions (H^+), as shown in Fig. 3.24. In addition, the mechanism of copper ions (Cu^{2+}) adsorption is possible via electrostatic attraction caused by the EDTA structure (H_4Y) to undergo dissociation process at the natural pH of copper ion solutions (pH 5.0) to their ionic form (H_2Y^{2-}) according to previous literature. Therefore, the interaction between copper ion (Cu^{2+}) molecules and the adsorbent surface can occur between EDTA species which dissociate ($-COO^-$) and positive charges from copper ions (Cu^{2+}) as shown in Fig 3.24. These results were related with the data from Fig. 3.10 and Table 3.2 as well as the prior literature (Lv et al., 2018, Shen et al., 2012, Zou et al., 2017).

3.3.3 Adsorption study of ibuprofen (IBP)

The adsorption process of IBP in aqueous solution was conducted at the natural pH which was in the pH range of 6.86-6.93. The maximum adsorption capacity and adsorption rate were investigated through several parameters that influenced the adsorption of IBP in a batch experiment.

3.3.3.1 Effect of adsorbent weight on ibuprofen (IBP) adsorption

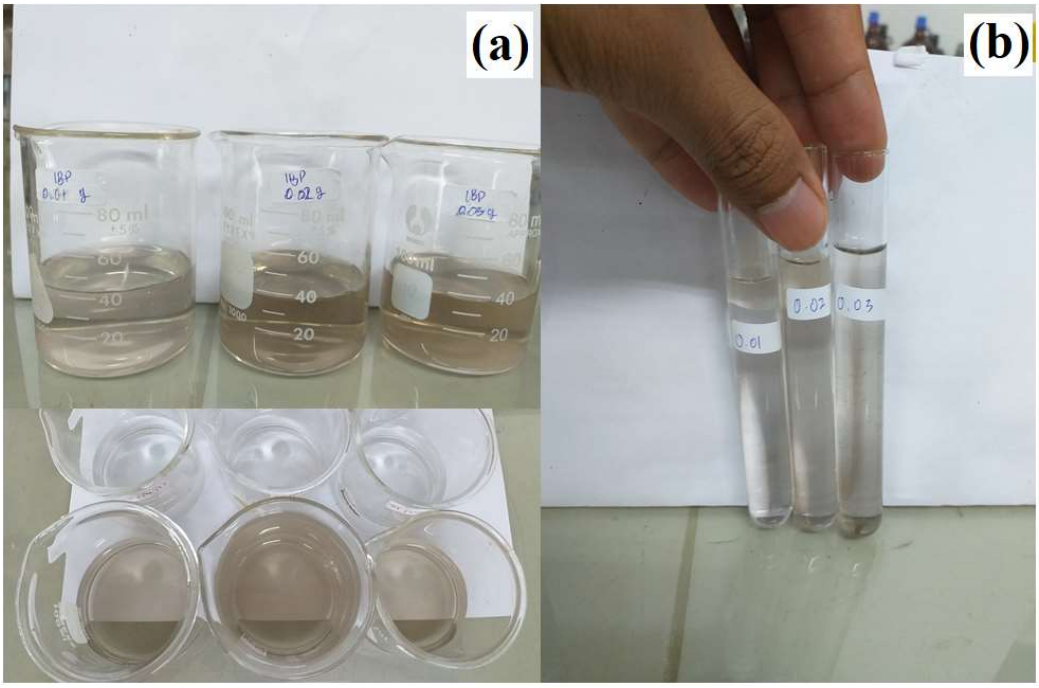

Fig. 3.25 The image of IBP solution before and after adsorption by effect of adsorbent weight (C_0 = 100 mg.L^{-1}, $W_{adsorbent}$ = 0.01-0.05 g, V = 50 mL, natural pH (pH 6.9) and T = 30°C)

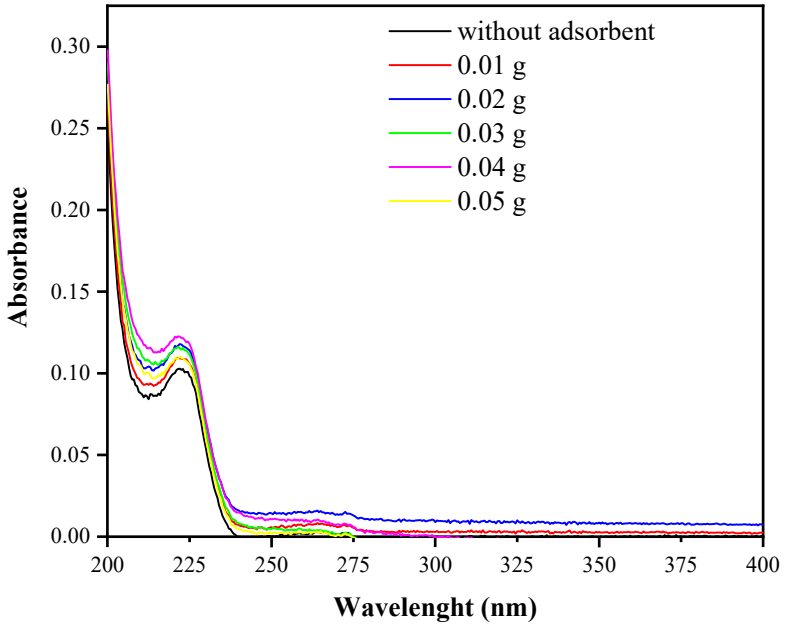

Fig. 3.26 UV-Vis spectra for IBP adsorption by effect of adsorbent weight (C_0 = 100 mg.L^{-1}, $W_{adsorbent}$ = 0.01-0.05 g, V = 50 mL, natural pH (pH 6.9) and T = 30^oC)

The variation of EDTA-FMHC-700 weight from 0.01-0.05 g was used to study its effect on the IBP adsorption. In general, the increase of the adsorbent weight will be offset by the increase of adsorption capacity due to the increase in the number of active sides on the adsorbent surface. Unfortunately, different results were shown in the IBP adsorption. This IBP adsorption cannot be studied further due to the phenomenon of increasing IBP concentration as the effect of increasing the adsorbent weight. As seen in Fig. 3.25(a-b), the increase of the adsorbent weight resulted in the IBP solution becoming more turbid even though it had undergone a centrifugation process. The increase in the absorbance value after the adsorption also occurs and followed by a slight shift in the maximum wavelength of IBP in the range of 221-223 nm, as shown in Fig. 3. 26.

This can be influenced by the pKa value of IBP and the surface charge of EDTA-FMHC-700. At the natural pH of IBP circa 6.86-6.93, the adsorbent surface was dominated by hydroxyl ions (OH^-) compared to hydrogen ions (H^+) due to the solution pH < pH_{pzc}. Then in the pKa value of IBP circa 4.91, IBP molecules were in

the neutral form species (Guedidi et al., 2017, Lindqvist et al., 2005). Whereas, if the solution pH > pKa value, the number of deprotonated species will increase. Therefore, these two things make the surface of the adsorbent produce a quite large electrostatic repulsion which make the adsorption of IBP less favourable (Reza et al., 2014). The other thing which allow this phenomenon to occur was due to the decrease in the total surface area of the adsorbent caused by the aggregation process on the adsorbent surface (Mondal et al., 2016). In consideration of the overall results, the IBP adsorption process on EDTA-FMHC-700 was not continued to the next step.

CHAPTER 4

CONCLUSION

1. The fabrication of Fe-Mn binary oxide ($MnFe_3O_4$) immobilized on hydrochar from green tea waste and coated with Ethylenediaminetetraacetic acid (EDTA) has successfully conducted by the facile hydrothermal carbonization combined with the activation process.
2. The overall of characterization results showed that the hydrothermal carbonization, activation and coating with EDTA had some effect on the physical and chemical properties of the all of synthesized materials.
3. The adsorptions of RhB and copper ion (Cu^{2+}) by EDTA-FMHC-700 were best fits with pseudo second order kinetic model and Langmuir isotherm model with the maximum adsorption capacity (q_{max}) of 21.41 and 9.43 $mg.g^{-1}$, respectively. The adsorption mechanisms of RhB and copper ion (Cu^{2+}) were facilitated *via* hydrogen bonding and the complexation process between the adsorbates and the adsorbent surface, respectively.
4. Meanwhile, the IBP adsorption process which was considered to fail may be caused by the electrostatic repulsion between the IBP molecule and EDTA-FMHC-700 surface, and the aggregation process which decreases the total surface area of the adsorbent.
5. The regeneration processes of EDTA-FMHC-700 on the adsorption of RhB and copper ion (Cu^{2+}) exhibit fast separation process as well as relatively good stability and acid resistance by maintaining of 75-80% performance from the initial conditions after four successive regeneration processes.
6. The use of EDTA-FMHC-700 as a low-cost adsorbent with good separation performance can be developed for industrial applications and environmental remediation.

BIBLIOGRAPHY

Aeenjan F, Javanbakht V (2018) Methylene blue removal from aqueous solution by magnetic clinoptilolite/chitosan/EDTA nanocomposite. Research on Chemical Intermediates 44:1459-1483

Ahmaruzzaman M, Gayatri SL (2010) Activated Tea Waste as a Potential Low-Cost Adsorbent for the Removal of p-Nitrophenol from Wastewater. Journal of Chemical & Engineering Data 55:4614-4623

Asfaram A, Ghaedi M, Hajati S, Goudarzi A, Dil EA (2017) Screening and optimization of highly effective ultrasound-assisted simultaneous adsorption of cationic dyes onto Mn-doped Fe3O4-nanoparticle-loaded activated carbon. Ultrasonics Sonochemistry 34:1-12

Attallah OA, Al-Ghobashy MA, Nebsen M, Salem MY (2016) Removal of cationic and anionic dyes from aqueous solution with magnetite/pectin and magnetite/silica/pectin hybrid nanocomposites: kinetic, isotherm and mechanism analysis. RSC Advances 6:11461-11480

Belachew N, Rama Devi D, Basavaiah K (2017) Green synthesis and characterisation of L-Serine capped magnetite nanoparticles for removal of Rhodamine B from contaminated water. Journal of Experimental Nanoscience 12:114-128

Bilal M, Shah JA, Ashfaq T, Gardazi SMH, Tahir AA, Pervez A, Haroon H, Mahmood Q (2013) Waste biomass adsorbents for copper removal from industrial wastewater—A review. Journal of Hazardous Materials 263:322-333

Boruah A, Rasheed A, Mendhe VA, Ganapathi S (2019) Specific surface area and pore size distribution in gas shales of Raniganj Basin, India. Journal of Petroleum Exploration and Production Technology 9:1041-1050

Burca S, Maicaneanu A, Indolean C (2016) A GREEN APPROACH: MALACHITE GREEN ADSORPTION ONTO WASTE GREEN TEA BIOMASS. ISOTHERM AND KINETIC STUDIES. Rev Roum Chim 61:541-547

Chung H-K, Kim W-H, Park J, Cho J, Jeong T-Y, Park P-K (2015) Application of Langmuir and Freundlich isotherms to predict adsorbate removal efficiency or required amount of adsorbent. Journal of Industrial and Engineering Chemistry 28:241-246

Cui L, Wang Y, Gao L, Hu L, Yan L, Wei Q, Du B (2015) EDTA functionalized magnetic graphene oxide for removal of Pb(II), Hg(II) and Cu(II) in water treatment: Adsorption mechanism and separation property. Chemical Engineering Journal 281:1-10

da Silva Lacerda V, López-Sotelo JB, Correa-Guimarães A, Hernández-Navarro S, Sánchez-Báscones M, Navas-Gracia LM, Martín-Ramos P, Martín-Gil J (2015) Rhodamine B removal with activated carbons obtained from lignocellulosic waste. Journal of Environmental Management 155:67-76

Das TR, Patra S, Madhuri R, Sharma PK (2018) Bismuth oxide decorated graphene oxide nanocomposites synthesized via sonochemical assisted hydrothermal method for adsorption of cationic organic dyes. Journal of Colloid and Interface Science 509:82-93

Deng L, Shi Z, Wang L, Zhou S (2017) Fabrication of a novel NiFe2O4/Zn-Al layered double hydroxide intercalated with EDTA composite and its adsorption behavior for Cr(VI) from aqueous solution. Journal of Physics and Chemistry of Solids 104:79-90

Ding M, Yang Y, Wu B, Li Y, Wang T, Ma L (2015) Study on reduction and carburization behaviors of iron phases for iron-based Fischer–Tropsch synthesis catalyst. Applied Energy 160:982-989

Dubey SP, Dwivedi AD, Sillanpää M, Gopal K (2010) Artemisia vulgaris-derived mesoporous honeycomb-shaped activated carbon for ibuprofen adsorption. Chemical Engineering Journal 165:537-544

Elaigwu SE, Rocher V, Kyriakou G, Greenway GM (2014) Removal of Pb2+ and Cd2+ from aqueous solution using chars from pyrolysis and microwave-assisted hydrothermal carbonization of Prosopis africana shell. Journal of Industrial and Engineering Chemistry 20:3467-3473

Essandoh M, Kunwar B, Pittman CU, Mohan D, Mlsna T (2015) Sorptive removal of salicylic acid and ibuprofen from aqueous solutions using pine wood fast pyrolysis biochar. Chemical Engineering Journal 265:219-227

Ghosal PS, Gupta AK (2017) Determination of thermodynamic parameters from Langmuir isotherm constant-revisited. Journal of Molecular Liquids 225:137-146

Guedidi H, Reinert L, Soneda Y, Bellakhal N, Duclaux L (2017) Adsorption of ibuprofen from aqueous solution on chemically surface-modified activated carbon cloths. Arabian Journal of Chemistry 10:S3584-S3594

Hao Y-M, Man C, Hu Z-B (2010) Effective removal of Cu (II) ions from aqueous solution by amino-functionalized magnetic nanoparticles. Journal of Hazardous Materials 184:392-399

Hayeeye F, Sattar M, Chinpa W, Sirichote O (2017) Kinetics and thermodynamics of Rhodamine B adsorption by gelatin/activated carbon composite beads. Colloids and Surfaces A: Physicochemical and Engineering Aspects 513:259-266

Hou B, Zhang H, Li H, Zhu Q (2012) Study on Kinetics of Iron Oxide Reduction by Hydrogen. Chinese Journal of Chemical Engineering 20:10-17

Hou X, Feng J, Ren Y, Fan Z, Zhang M (2010) Synthesis and adsorption properties of spongelike porous MnFe2O4. Colloids and Surfaces A: Physicochemical and Engineering Aspects 363:1-7

Ibrahim RK, El-Shafie A, Hin LS, Mohd NSB, Aljumaily MM, Ibraim S, AlSaadi MA (2019) A clean approach for functionalized carbon nanotubes by deep eutectic solvents and their performance in the adsorption of methyl orange from aqueous solution. Journal of Environmental Management 235:521-534

Indolean C, Burcă S, Măicăneanu A (2017) Adsorptive Removal of Malachite Green from Model Aqueous Solutions by Chemically Modified Waste Green Tea Biomass. 2017 64:9

Inyang M, Gao B, Yao Y, Xue Y, Zimmerman AR, Pullammanappallil P, Cao X (2012) Removal of heavy metals from aqueous solution by biochars derived from anaerobically digested biomass. Bioresource Technology 110:50-56

Inyinbor AA, Adekola FA, Olatunji GA (2016) Kinetics, isotherms and thermodynamic modeling of liquid phase adsorption of Rhodamine B dye onto Raphia hookerie fruit epicarp. Water Resources and Industry 15:14-27

Iovino P, Canzano S, Capasso S, Erto A, Musmarra D (2015) A modeling analysis for the assessment of ibuprofen adsorption mechanism onto activated carbons. Chemical Engineering Journal 277:360-367

Jiang X, Huang J (2016) Adsorption of Rhodamine B on two novel polar-modified post-cross-linked resins: Equilibrium and kinetics. Journal of Colloid and Interface Science 467:230-238

Jiao X, Liu C, Huang K, Zhang S, He S, Zhao L, Zeng X (2015) Molecular design and synthesis of a pH independent and cell permeant fluorescent dye and its applications. Organic & Biomolecular Chemistry 13:6647-6653

Kambo HS, Dutta A (2015) A comparative review of biochar and hydrochar in terms of production, physico-chemical properties and applications. Renewable and Sustainable Energy Reviews 45:359-378

Keyvani F, Rahpeima S, Javanbakht V (2018) Synthesis of EDTA-modified magnetic activated carbon nanocomposite for removal of permanganate from aqueous solutions. Solid State Sciences 83:31-42

Khamparia S, Jaspal DK (2017) Xanthium strumarium L. seed hull as a zero cost alternative for Rhodamine B dye removal. Journal of Environmental Management 197:498-506

Konicki W, Siber D, Narkiewicz U (2017) Removal of Rhodamine B from aqueous solution by ZnFe2O4 nanocomposite with magnetic separation performance. 19:65

Kooh MRR, Dahri MK, Lim L (2016): The removal of Rhodamine B dye from aqueous solution using Casuarina equisetifolia needles as adsorbent, 2, 1140553 pp

Koottatep T, Fakkaew K, Tajai N, Polprasert C (2017) Isotherm models and kinetics of copper adsorption by using hydrochar produced from hydrothermal carbonization of faecal sludge. Journal of Water Sanitation and Hygiene for Development

Lamdab U, Wetchakun K, Kangwansupamonkon W, Wetchakun N (2018) Effect of a pH-controlled co-precipitation process on rhodamine B adsorption of MnFe2O4 nanoparticles. RSC Advances 8:6709-6718

Lei Y, Su H, Tian R (2016) Morphology evolution, formation mechanism and adsorption properties of hydrochars prepared by hydrothermal carbonization of corn stalk. RSC Advances 6:107829-107835

Li B, Ma J, Zhou L, Qiu Y (2017) Magnetic microsphere to remove tetracycline from water: Adsorption, H2O2 oxidation and regeneration. Chemical Engineering Journal 330:191-201

Li T-t, Liu Y-g, Peng Q-q, Hu X-j, Liao T, Wang H, Lu M (2013) Removal of lead(II) from aqueous solution with ethylenediamine-modified yeast biomass coated with magnetic chitosan microparticles: Kinetic and equilibrium modeling. Chemical Engineering Journal 214:189-197

Li Y, Wu M, Wang B, Wu Y, Ma M, Zhang X (2016) Synthesis of Magnetic Lignin-Based Hollow Microspheres: A Highly Adsorptive and Reusable Adsorbent Derived from Renewable Resources. ACS Sustainable Chemistry & Engineering 4:5523-5532

Lin L, Jiang W, Xu P (2017) Comparative study on pharmaceuticals adsorption in reclaimed water desalination concentrate using biochar: Impact of salts and organic matter. Science of The Total Environment 601-602:857-864

Lindqvist N, Tuhkanen T, Kronberg L (2005) Occurrence of acidic pharmaceuticals in raw and treated sewages and in receiving waters. Water research 39:2219-28

Liu F, Zhang W, Chen W, Wang J, Yang Q, Zhu W, Wang J (2017) One-pot synthesis of NiFe2O4 integrated with EDTA-derived carbon dots for enhanced removal of tetracycline. Chemical Engineering Journal 310:187-196

Liu Y, Chen M, Yongmei H (2013) Study on the adsorption of Cu(II) by EDTA functionalized Fe3O4 magnetic nano-particles. Chemical Engineering Journal 218:46-54

Liu Y, Fu R, Sun Y, Zhou X, Baig SA, Xu X (2016) Multifunctional nanocomposites Fe3O4@SiO2-EDTA for Pb(II) and Cu(II) removal from aqueous solutions. Applied Surface Science 369:267-276

Lv D, Liu Y, Zhou J, Yang K, Lou Z, Baig SA, Xu X (2018) Application of EDTA-functionalized bamboo activated carbon (BAC) for Pb(II) and Cu(II) removal from aqueous solutions. Applied Surface Science 428:648-658

Mahmood T, Ali R, Naeem A, Hamayun M, Aslam M (2017) Potential of used Camellia sinensis leaves as precursor for activated carbon preparation by chemical activation with H3PO4; optimization using response surface methodology. Process Safety and Environmental Protection 109:548-563

Mahmoud ME, Hassan SSM, Kamel AH, Elserw MIA (2018) Development of microwave-assisted functionalized nanosilicas for instantaneous removal of heavy metals. Powder Technology 326:454-466

Maniyazagan M, Chakraborty S, Perez-Sanchez H, Stalin T (2019) Encapsulation of triclosan within 2-hydroxypropyl-beta-cyclodextrin cavity and its application in the chemisorption of rhodamine B dye. Journal of Molecular Liquids 282:235-243

Masoudi A, Honarasa F (2018) C-dots/Fe3O4 magnetic nanocomposite as nanoadsorbent for removal of heavy metal cations. Journal of the Iranian Chemical Society 15:1199-1205

Matsumura Y (2015): Chapter 9 - Hydrothermal Gasification of Biomass. In: Pandey A, Bhaskar T, Stöcker M , Sukumaran RK (Editors), Recent Advances in Thermo-Chemical Conversion of Biomass. Elsevier, Boston, pp. 251-267

Mishra K, Poudel TN, Basavegowda N, Lee YR (2016) Enhanced catalytic performance of magnetic Fe3O4–MnO2 nanocomposites for the decolorization of rhodamine B, reduction of 4-nitroaniline, and sp3 C–H functionalization of 2-methylpyridines to isatins. Journal of Catalysis 344:273-285

Möller M, Nilges P, Harnisch F, Schröder U (2011) Subcritical Water as Reaction Environment: Fundamentals of Hydrothermal Biomass Transformation. ChemSusChem 4:566-579

Mondal S, Aikat K, Halder G (2016) Biosorptive uptake of ibuprofen by chemically modified Parthenium hysterophorus derived biochar: Equilibrium, kinetics, thermodynamics and modeling. Ecological Engineering 92:158-172

Naseem K, Farooqi ZH, Begum R, Ghufran M, Rehman MZU, Najeeb J, Irfan A, Al-Sehemi AG (2018) Poly(N-isopropylmethacrylamide-acrylic acid) microgels as adsorbent for removal of toxic dyes from aqueous medium. Journal of Molecular Liquids 268:229-238

Nawaz F, Xie Y, Xiao J, Cao H, Li Y, Zhang D (2016) Insights into the mechanism of phenolic mixture degradation by catalytic ozonation with a mesoporous Fe3O4/MnO2 composite. RSC Advances 6:29674-29684

Ojemaye MO, Okoh OO, Okoh AI (2017) Adsorption of Cu2+ from aqueous solution by a novel material; azomethine functionalized magnetic nanoparticles. Separation and Purification Technology 183:204-215

Punyapalakul P, Soonglerdsongpha S, Kanlayaprasit C, Ngamcharussrivichai C, Khaodhiar S (2009) Effects of crystalline structures and surface functional groups on the adsorption of haloacetic acids by inorganic materials. Journal of Hazardous Materials 171:491-499

Regmi P, Garcia Moscoso JL, Kumar S, Cao X, Mao J, Schafran G (2012) Removal of copper and cadmium from aqueous solution using switchgrass biochar produced via hydrothermal carbonization process. Journal of Environmental Management 109:61-69

Ren Y, Li N, Feng J, Luan T, Wen Q, Li Z, Zhang M (2012) Adsorption of Pb(II) and Cu(II) from aqueous solution on magnetic porous ferrospinel MnFe2O4. Journal of Colloid and Interface Science 367:415-421

Reza RA, Ahmaruzzaman M, Sil AK, Gupta VK (2014) Comparative Adsorption Behavior of Ibuprofen and Clofibric Acid onto Microwave Assisted Activated Bamboo Waste. Industrial & Engineering Chemistry Research 53:9331-9339

Saleh TA, Ali I (2018) Synthesis of polyamide grafted carbon microspheres for removal of rhodamine B dye and heavy metals. Journal of Environmental Chemical Engineering 6:5361-5368

Semerciöz AS, Göğüş F, Çelekli A, Bozkurt H (2017) Development of carbonaceous material from grapefruit peel with microwave implemented-low temperature hydrothermal carbonization technique for the adsorption of Cu (II). Journal of Cleaner Production 165:599-610

Shao L, Ren Z, Zhang G, Chen L (2012) Facile synthesis, characterization of a MnFe2O4/activated carbon magnetic composite and its effectiveness in tetracycline removal. Materials Chemistry and Physics 135:16-24

Shen H, Pan S, Zhang Y, Huang X, Gong H (2012) A new insight on the adsorption mechanism of amino-functionalized nano-Fe3O4 magnetic polymers in Cu(II), Cr(VI) co-existing water system. Chemical Engineering Journal 183:180-191

Sukriti, Sharma J, Chadha AS, Pruthi V, Anand P, Bhatia J, Kaith BS (2017) Sequestration of dyes from artificially prepared textile effluent using RSM-CCD optimized hybrid backbone based adsorbent-kinetic and equilibrium studies. Journal of Environmental Management 190:176-187

Sultan M, Miyazaki T, Koyama S (2018) Optimization of adsorption isotherm types for desiccant air-conditioning applications. Renewable Energy 121:441-450

Sun H, Cao L, Lu L (2011) Magnetite/reduced graphene oxide nanocomposites: One step solvothermal synthesis and use as a novel platform for removal of dye pollutants. Nano Research 4:550-562

Tzereme A, Christodoulou E, Kyzas GZ, Kostoglou M, Bikiaris DN, Lambropoulou DA (2019) Chitosan Grafted Adsorbents for Diclofenac Pharmaceutical Compound Removal from Single-Component Aqueous Solutions and Mixtures. Polymers 11:24

Wang J, Tang B, Tsuzuki T, Liu Q, Hou X, Sun L (2012) Synthesis, characterization and adsorption properties of superparamagnetic polystyrene/Fe3O4/graphene oxide. Chemical Engineering Journal 204-206:258-263

Wang Z, Shen D, Shen F, Wu C, Gu S (2017) Kinetics, equilibrium and thermodynamics studies on biosorption of Rhodamine B from aqueous solution by earthworm manure derived biochar. International Biodeterioration & Biodegradation 120:104-114

Weng C-H, Lin Y-T, Chen Y-J, Sharma YC (2013) Spent green tea leaves for decolourisation of raw textile industry wastewater. Coloration Technology 129:298-304

Xiong Y, Tong Q, Shan W, Xing Z, Wang Y, Wen S, Lou Z (2017) Arsenic transformation and adsorption by iron hydroxide/manganese dioxide doped straw activated carbon. Applied Surface Science 416:618-627

Xu W, Song Y, Dai K, Sun S, Liu G, Yao J (2018) Novel ternary nanohybrids of tetraethylenepentamine and graphene oxide decorated with MnFe2O4 magnetic nanoparticles for the adsorption of Pb(II). Journal of Hazardous Materials 358:337-345

Yang J, Zhao Y, Liang S, Zhang S, Ma S, Li H, Zhang J, Zheng C (2018a) Magnetic iron–manganese binary oxide supported on carbon nanofiber (Fe3−xMnxO4/CNF) for efficient removal of Hg0 from coal combustion flue gas. Chemical Engineering Journal 334:216-224

Yang Q, Ren S, Zhao Q, Lu R, Hang C, Chen Z, Zheng H (2018b) Selective separation of methyl orange from water using magnetic ZIF-67 composites. Chemical Engineering Journal 333:49-57

Yang S, Wu Y, Aierken A, Zhang M, Fang P, Fan Y, Ming Z (2016) Mono/competitive adsorption of Arsenic(III) and Nickel(II) using modified green tea waste. Journal of the Taiwan Institute of Chemical Engineers 60:213-221

Yi I-G, Kang J-K, Lee S-C, Lee C-G, Kim S-B (2019) Synthesis of an oxidized mesoporous carbon-based magnetic composite and its application for heavy metal removal from aqueous solutions. Microporous and Mesoporous Materials 279:45-52

Yin Y, Guo X, Peng D (2018) Iron and manganese oxides modified maize straw to remove tylosin from aqueous solutions. Chemosphere 205:156-165

Yoon K, Cho D-W, Tsang DCW, Bolan N, Rinklebe J, Song H (2017) Fabrication of engineered biochar from paper mill sludge and its application into removal of arsenic and cadmium in acidic water. Bioresource Technology 246:69-75

Zhang BB, Xu JC, Xin PH, Han YB, Hong B, Jin HX, Jin DF, Peng XL, Li J, Gong J, Ge HL, Zhu ZW, Wang XQ (2015) Magnetic properties and adsorptive performance of manganese–zinc ferrites/activated carbon nanocomposites. Journal of Solid State Chemistry 221:302-305

Zhang Y, Shao D, Yan J, Jia X, Li Y, Yu P, Zhang T (2016) The pore size distribution and its relationship with shale gas capacity in organic-rich mudstone of Wufeng-Longmaxi Formations, Sichuan Basin, China. Journal of Natural Gas Geoscience 1:213-220

Zhao D, Zhang Q, Xuan H, Chen Y, Zhang K, Feng S, Alsaedi A, Hayat T, Chen C (2017) EDTA functionalized Fe3O4/graphene oxide for efficient removal of U(VI) from aqueous solutions. Journal of Colloid and Interface Science 506:300-307

Zhou Q, Liao B, Lin L, Qiu W, Song Z (2018) Adsorption of Cu(II) and Cd(II) from aqueous solutions by ferromanganese binary oxide–biochar composites. Science of The Total Environment 615:115-122

Zhu J, Baig SA, Sheng T, Lou Z, Wang Z, Xu X (2015) Fe3O4 and MnO2 assembled on honeycomb briquette cinders (HBC) for arsenic removal from aqueous solutions. Journal of Hazardous Materials 286:220-228

Zou Z, Shi Z, Deng L (2017) Highly efficient removal of Cu(ii) from aqueous solution using a novel magnetic EDTA functionalized CoFe2O4. RSC Adv 7:5195-5205

Appendix 1 Equipment and Instruments

A1.1. All images of analytical instrument

Fig. A1.1.1 CHNS/O Analyzers Thermo Scientific^{TM} Flash 2000

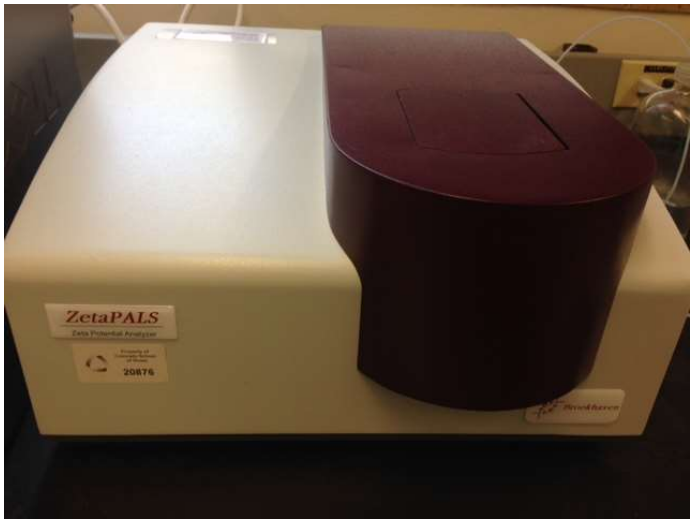

Fig. A1.1.2 PALS Zeta Potential Analyzer

Fig. A1.1.3 FTIR Perkin Elmer Spectrum BX

Fig. A1.1.4 Vibrating sample magnetometer (VSM)

Fig. A1.1.5 Surface Area and Porosity Analyzer, Micromeritic ASAP2460

Fig. A1.1.6 XRD PANalytical X'Pert MPD

Fig. A1.1.7 XPS AXIS Ultra DLD Shimadzu

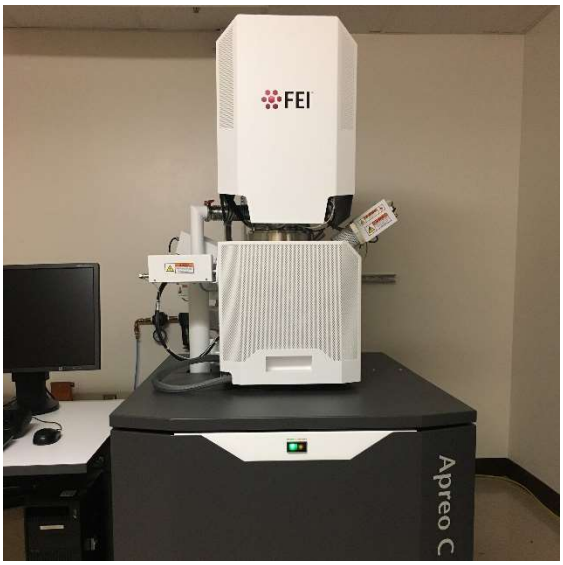

Fig. A1.1.8 SEM-EDX Thermo Scientific™ Apreo

Fig. A1.1.9 UV-Vis Spectrophotometer Shimadzu UV-2600

Fig. A1.1.10 ICP-OES Perkin Elmer AVIO^{TM} 500

A1.2. All images of the used equipment

Fig. A1.2.1 Teflon lined autoclave reactor 400 mL

Fig. A1.2.2 Electric oven (ULP 400 Memmert)

Fig. A1.2.3 pH meter (Delta 320 Mettler Toledo)

Fig. A1.2.4 Laboratory shaker (IKA KS 130)

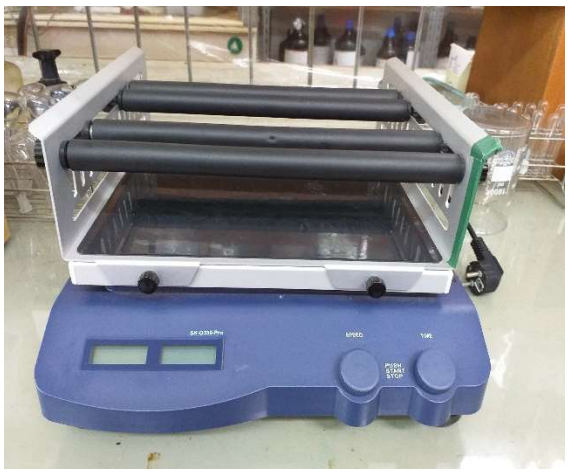

Fig. A1.2.5 Laboratory shaker (Scilogex SK-O330-Pro)

Fig. A1.2.6 Laboratory shaker (Scilogex SK-O330-Pro)

Fig. A1.2.7 Neodymium magnet grade N35 (100 mm x 50 mm x 10 mm)

Appendix 2 Characterization of all the synthesized materials

A2.1. EDX spectrums of FMHC, FMHC-700 and EDTA-FMHC-700

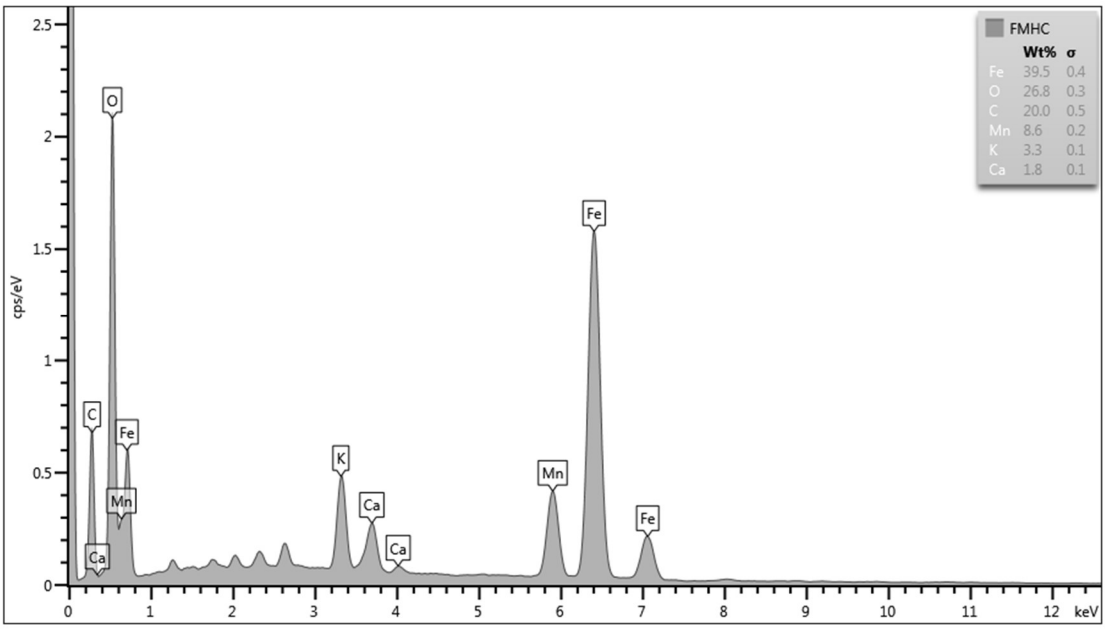

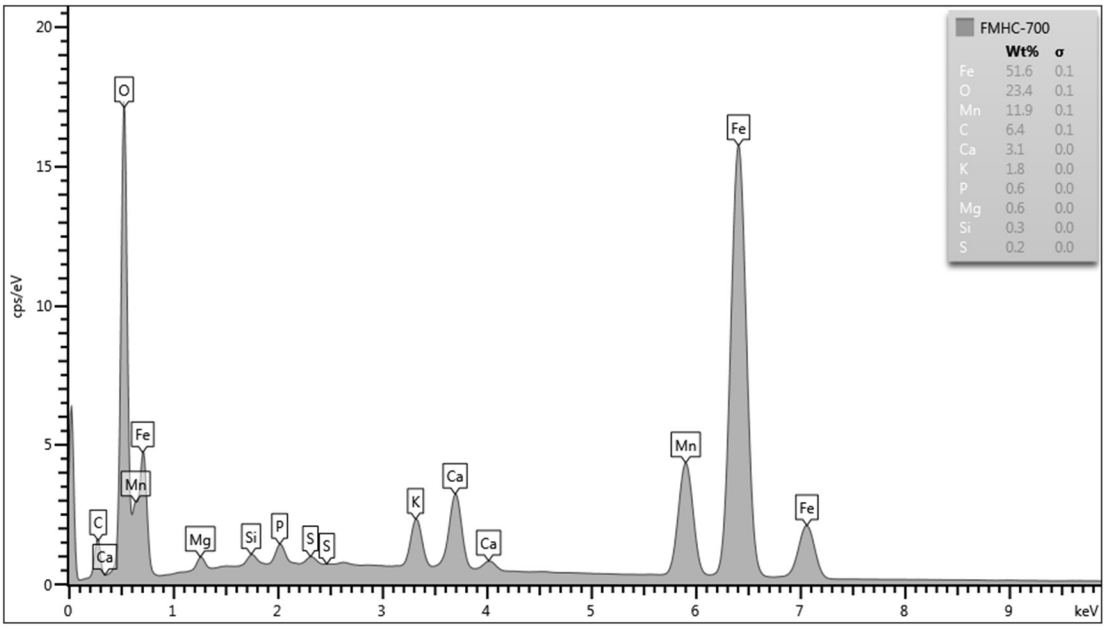

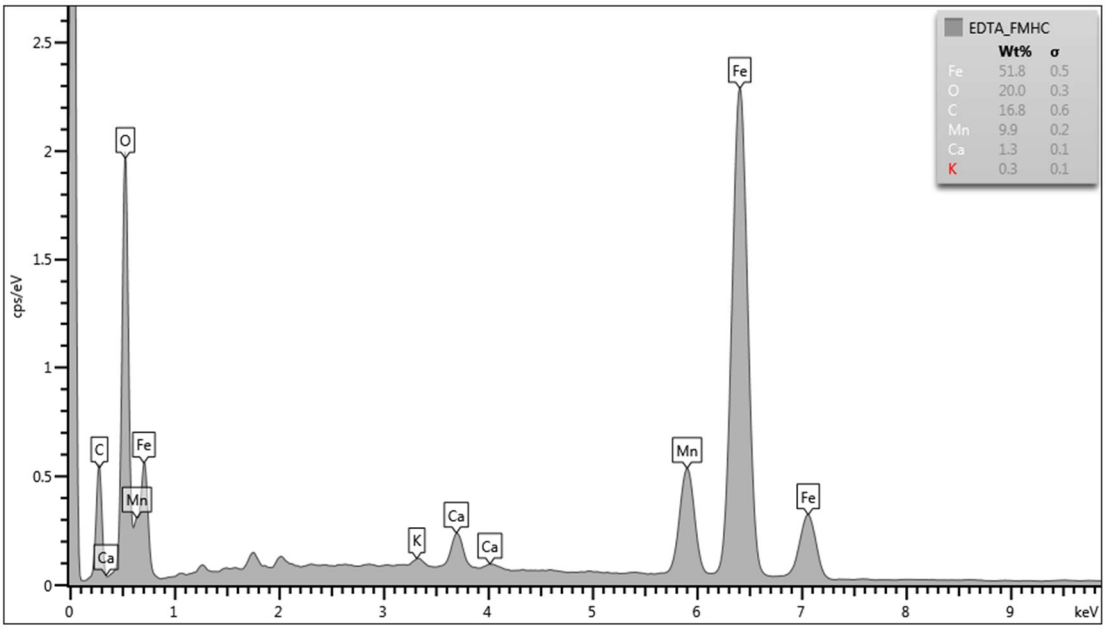
EDTA_FMHC
Wt% σ
Fe 51.8 0.5
O 20.0 0.3
C 16.8 0.6
Mn 9.9 0.2
Ca 1.3 0.1
K 0.3 0.1
cps/eV
keV
O
C
Fe
Mn
Ca
K
Ca
Ca
Mn
Fe
Fe

Appendix 3 Adsorption Study of Rhodamine B (RhB)

Table A3.1. Data of calibration curve of RhB standard solutions

C ($mg.L^{-1}$)	Absorbance (at λ=554 nm)
0.5	0.12
1	0.23
1.5	0.35
2	0.46
2.5	0.57
3	0.67
3.5	0.80
4	0.90

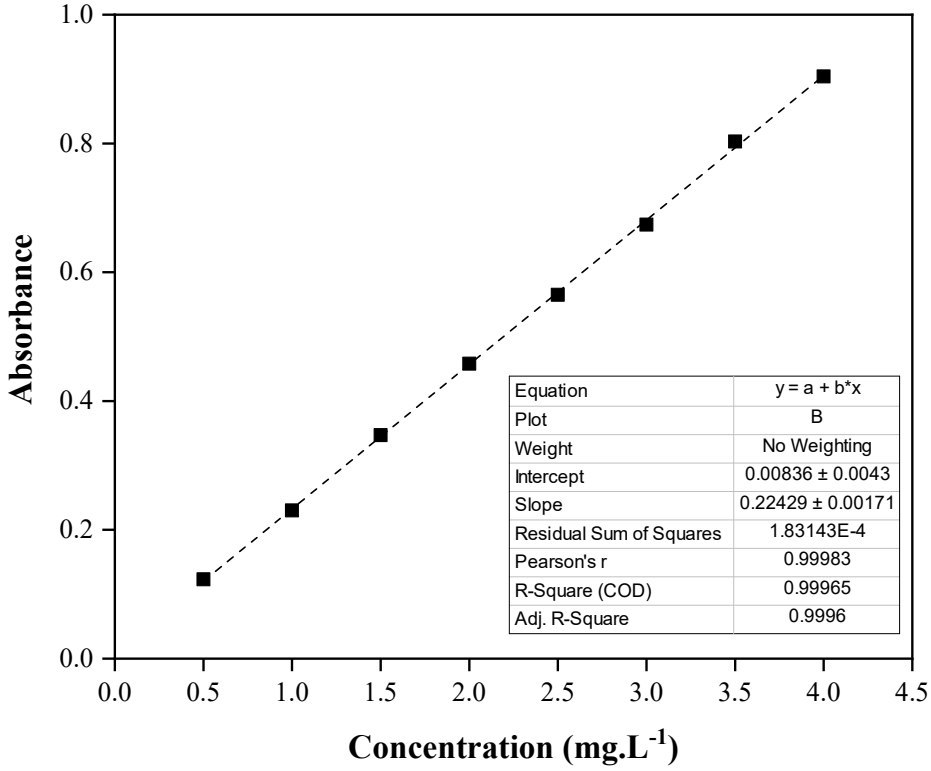

Fig A3.1. Calibration curve of RhB standard solution

Table A3.2. Effect of adsorbent weight on the adsorption capacity of RhB

Weight	q_e (mg.g^{-1})					% Removal				
(g)	I	II	III	Mean	SD	I	II	III	Mean	SD
0.01	6.13	7.24	8.36	7.24	1.11	1.31	1.54	2.02	1.62	0.36
0.02	8.08	8.64	9.47	8.73	0.70	3.44	3.68	4.04	3.72	0.3
0.03	13.37	13.75	13.93	13.68	0.28	8.55	8.78	8.9	8.74	0.18
0.04	15.88	15.74	16.44	16.02	0.36	13.53	13.41	14	13.65	0.31
0.05	14.16	14.27	12.71	13.71	0.86	15.07	15.19	15.66	15.31	0.31
0.06	12.35	12.18	12.91	12.57	0.29	15.78	15.9	16.5	16.06	0.38
0.07	12.1	12.18	12.74	12.34	0.34	18.04	18.16	18.99	18.4	0.52
0.08	11.42	11.49	11.35	11.42	0.06	19.46	19.58	19.34	19.46	0.12

0.09	10.28	10.4	10.22	10.3	0.09	19.7	19.94	19.58	19.74	0.18
0.1	8.97	9.1	9.08	9.08	0.11	19.11	19.58	19.34	19.34	0.24

Table A3.3. Effect of solution pH on the adsorption of RhB

pH	q_e (mg.g^{-1})				
	I	II	III	Mean	SD
2	42.35	42.91	43.19	42.82	0.43
3	16.16	16.72	17.28	16.72	0.56
4	12.82	13.1	12.26	12.72	0.43
5	10.31	9.75	9.2	9.75	0.56
6	6.96	7.52	8.08	7.52	0.56
7	8.92	9.47	8.36	8.92	0.56
8	8.36	9.2	10.87	9.47	1.28
9	11.15	11.42	11.7	11.42	0.28
10	13.65	13.37	13.93	13.65	0.28
11	29.26	29.54	30.93	29.91	0.90

Table A3.4. Data of kinetics studies on the adsorption of RhB ($V_{solution}$ = 50 mL, $W_{adsorbent}$ = 0.04 g, C_0 = 100 mg.L^{-1}, shaking = 320 rpm, natural pH, time = 1-120 mins and T = 30^{o}C)

Time	C_e (mg.L^{-1})					q_e (mg.g^{-1})				
(mins)	I	II	III	Mean	SD	I	II	III	Mean	SD
10	92.41	91.73	90.50	91.55	1.21	11.39	12.25	13.78	12.47	1.21
20	89.65	90.82	89.07	89.85	1.12	14.85	13.38	15.57	14.60	1.12
30	89.29	88.22	86.91	88.14	1.49	15.29	16.64	18.27	16.73	1.49
40	88.20	86.91	90.04	88.39	1.96	16.66	18.27	14.36	16.43	1.96
50	89.66	88.21	86.91	88.26	1.71	14.84	16.65	18.27	16.58	1.71
60	89.27	86.87	88.88	88.34	1.61	15.33	18.32	15.81	16.48	1.61
120	86.79	88.19	89.00	87.99	1.40	18.42	16.67	15.65	16.91	1.40

Table A3.5. Linear plot of pseudo-first-order kinetics model on the adsorption of RhB

Time (mins)	Pseudo-first-order			
	ln ($q_e - q_t$)	**Slope**	**Intercept**	**R^2**
0	2.82	-0.0222	0.9777	0.2752
10	1.45			
20	0.75			
30	#NUM!			
40	-1.19			
50	-1.92			
60	-1.40			
120	#NUM!			

Table A3.6. Linear plot of pseudo-second-order kinetics model on the adsorption of RhB

Time (mins)	Pseudo-second-order			
	t/q_t	**Slope**	**Intercept**	**R^2**
0	#DIV/0!	0.0583	0.1158	0.9989
10	0.80			
20	1.37			
30	1.79			
40	2.44			
50	3.01			
60	3.64			
120	7.09			

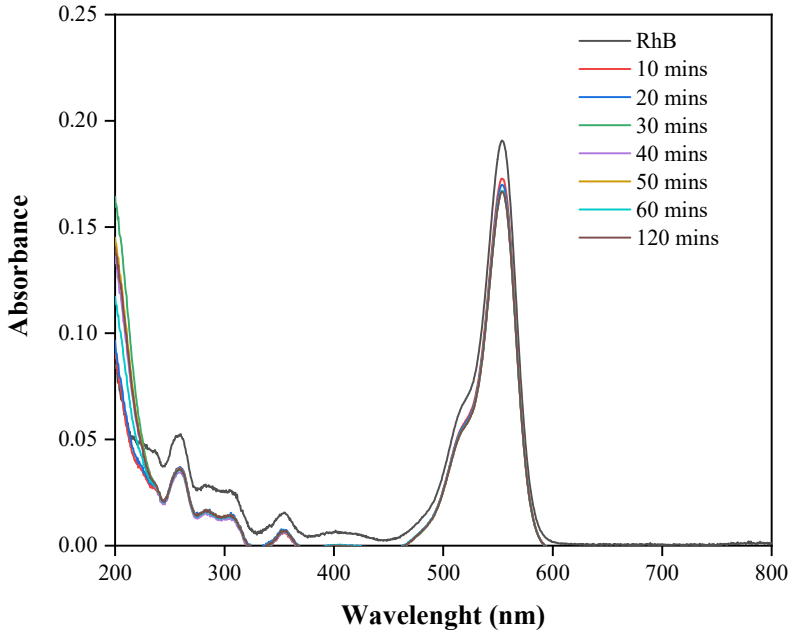

Fig. A3.2. Spectrum of RhB before and after adsorption by EDTA-FMHC-700

Table A3.7. Data of isotherm studies on the adsorption of RhB ($V_{solution}$ = 50 mL, $W_{adsorbent}$ = 0.04 g, C_0 = 10-250 mg.L^{-1}, shaking = 320 rpm, natural pH, time = 24 h and T = 30^{o}C)

C_0	C_e (mg.L^{-1})					q_e (mg.g^{-1})				
(mg.L^{-1})	I	II	III	Mean	SD	I	II	III	Mean	SD
10	10.18	10.06	10.23	10.16	0.09	5.57	5.71	5.50	5.59	0.11
25	23.03	22.69	22.36	22.69	0.33	9.33	9.75	10.17	9.75	0.42
50	36.47	36.25	36.91	36.54	0.34	14.77	15.05	14.21	14.68	0.43
75	69.24	68.79	68.12	6.72	0.56	16.72	17.28	18.11	17.37	0.70
100	96.43	95.99	94.87	95.76	0.80	18.67	19.23	20.62	19.51	1.00
150	133.88	135.22	134.11	134.40	0.72	19.23	17.55	18.95	18.58	0.90
200	179	180.12	176.77	178.63	1.70	18.11	16.72	20.90	18.58	2.13
250	226.93	231.39	229.16	229.16	2.23	22.29	16.72	19.50	19.50	2.79

Table A3.7. Data of isotherm studies on the adsorption of RhB ($V_{solution}$ = 50 mL, $W_{adsorbent}$ = 0.04 g, C_0 = 10-250 mg.L^{-1}, shaking = 320 rpm, natural pH, time = 24 h and T = 30^{o}C) (Continued)

C_0	Log C_e					Log q_e				
(mg.L^{-1})	I	II	III	Mean	SD	I	II	III	Mean	SD
10	1.01	1.00	1.01	1.01	0.00	0.75	0.76	0.74	0.75	0.01
25	1.36	1.36	1.35	1.36	0.01	0.97	0.99	1.01	0.99	0.02
50	1.56	1.56	1.57	1.56	0.00	1.17	1.18	1.15	1.17	0.01
75	1.84	1.84	1.83	1.84	0.00	1.22	1.24	1.26	1.24	0.02
100	1.98	1.98	1.98	1.98	0.00	1.27	1.28	1.31	1.29	0.02
150	2.13	2.13	2.13	2.13	0.00	1.28	1.24	1.28	1.27	0.02
200	2.25	2.26	2.25	2.25	0.00	1.26	1.22	1.32	1.27	0.05
250	2.36	2.36	2.36	2.36	0.00	1.35	1.22	1.29	1.29	0.06

Table A3.8. Data of isotherm studies on the adsorption of RhB ($V_{solution}$ = 50 mL, $W_{adsorbent}$ = 0.04 g, C_0 = 10-250 mg.L^{-1}, shaking = 320 rpm, natural pH, time = 24 h and T = 40^{o}C)

C_0	C_e (mg.L^{-1})					q_e (mg.g^{-1})				
(mg.L^{-1})	I	II	III	Mean	SD	I	II	III	Mean	SD
10	9.23	9.12	9.28	9.21	0.09	6.34	6.48	6.27	6.36	0.11
25	15.78	15.56	15.45	15.60	0.17	9.61	9.89	10.03	9.84	0.21
50	36.91	36.70	37.14	36.91	0.22	17	17.28	16.72	17	0.28
75	60.77	60.32	59.88	60.32	0.45	20.62	21.18	21.73	21.18	0.56
100	85.96	85.51	8.40	85.29	0.80	24.52	25.08	26.47	25.36	1.0
150	132.77	134.11	133.44	133.44	0.67	25.36	23.68	24.52	24.52	0.84
200	184.57	182.35	183.46	183.46	1.11	25.08	27.86	26.47	26.47	1.39
250	226.93	228.04	230.27	228.41	1.70	27.86	26.47	23.68	26	2.13

Table A3.8. Data of isotherm studies on the adsorption of RhB ($V_{solution}$ = 50 mL, $W_{adsorbent}$ = 0.04 g, C_0 = 10-250 mg.L^{-1}, shaking = 320 rpm, natural pH, time = 24 h and T = 40^{o}C) (Continued)

C_0	Log C_e					Log q_e				
(mg.L^{-1})	I	II	III	Mean	SD	I	II	III	Mean	SD
10	0.97	0.96	0.97	0.97	0.00	0.80	0.81	0.80	0.80	0.00
25	1.20	1.19	1.19	1.19	0.00	0.98	1.00	1.00	0.99	0.01
50	1.57	1.56	1.57	1.57	0.00	1.23	1.24	1.22	1.23	0.01
75	1.78	1.78	1.78	1.78	0.00	1.31	1.33	1.34	1.33	0.01
100	1.93	1.93	1.93	1.93	0.00	1.39	1.40	1.42	1.42	0.02
150	2.12	2.13	2.13	2.13	0.00	1.40	1.37	1.39	1.39	0.01
200	2.27	2.26	2.26	2.26	0.00	1.40	1.45	1.42	1.42	0.02
250	2.36	2.36	2.36	2.36	0.00	1.45	1.42	1.37	1.41	0.04

Table A3.9. Data of isotherm studies on the adsorption of RhB ($V_{solution}$ = 50 mL, $W_{adsorbent}$ = 0.04 g, C_0 = 10-250 mg.L^{-1}, shaking = 320 rpm, natural pH, time = 24 h and T = 50^{o}C)

C_0	C_e (mg.L^{-1})					q_e (mg.g^{-1})				
(mg.L^{-1})	I	II	III	Mean	SD	I	II	III	Mean	SD
10	8.23	8.28	8.11	8.21	0.09	7.59	7.52	7.73	7.61	0.11
25	14.56	14.22	14.67	14.48	0.23	13.51	13.93	13.79	13.74	0.21
50	33.35	33.79	32.90	33.35	0.45	21.46	20.9	22.01	21.46	0.56
75	52.52	52.07	52.74	52.44	0.34	26.19	26.75	25.91	26.28	0.43
100	73.03	72.36	73.47	72.95	0.56	32.04	32.88	31.49	32.14	0.70
150	128.53	128.76	129.20	128.83	0.34	33.44	33.16	32.60	33.07	0.43
200	170.08	173.43	171.20	171.57	1.70	34.83	30.65	33.44	32.97	2.13
250	226.93	229.16	228.04	228.04	1.11	36.22	33.44	34.83	34.83	1.39

Table A3.9. Data of isotherm studies on the adsorption of RhB ($V_{solution}$ = 50 mL, $W_{adsorbent}$ = 0.04 g, C_0 = 10-250 mg.L^{-1}, shaking = 320 rpm, natural pH, time = 24 h and T = 50^{o}C) (Continued)

C_0	Log C_e					Log q_e				
(mg.L^{-1})	I	II	III	Mean	SD	I	II	III	Mean	SD
10	0.92	0.92	0.91	0.92	0.00	0.88	0.88	0.89	0.88	0.01
25	1.21	1.20	1.20	1.20	0.00	1.13	1.14	1.14	1.14	0.01
50	1.52	1.53	1.52	1.52	0.01	1.33	1.32	1.34	1.33	0.01
75	1.72	1.72	1.72	1.72	0.00	1.42	1.43	1.41	1.42	0.01
100	1.86	1.86	1.87	1.86	0.00	1.51	1.52	1.50	1.51	0.01
150	2.11	2.11	2.11	2.11	0.00	1.52	1.52	1.51	1.52	0.01
200	2.23	2.24	2.23	2.23	0.00	1.54	1.50	1.52	1.52	0.03
250	2.36	2.36	2.36	2.36	0.00	1.56	1.52	1.54	1.54	0.02

Appendix 4 Adsorption Study of copper ion (Cu^{2+})

Table A4.1. Effect of adsorbent weight on the adsorption capacity of copper ion (Cu^{2+})

Weight (g)	q_e (mg.g^{-1})					% Removal				
	I	II	III	Mean	SD	I	II	III	Mean	SD
0.01	7.15	6.65	7.75	7.18	0.55	1.44	1.35	1.52	1.44	0.09
0.03	13.25	9.07	6.25	9.52	3.52	7.7	5.5	3.79	5.66	1.96
0.05	12.59	8.87	9.36	10.27	2.02	12.2	8.96	9.46	10.21	1.74
0.08	10.45	9.58	9.78	9.94	0.46	16.2	15.48	19.23	16.97	1.99
0.1	11.48	8.25	9.2	9.64	1.66	22.24	16.67	18.59	19.17	2.83

Table A4.2. Effect of solution pH on the adsorption of copper ion (Cu^{2+})

pH	q_e (mg.g^{-1})				
	I	II	III	Mean	SD
2	0.70	0.40	0.30	0.47	0.21
3	1.70	1.40	2.00	1.70	0.45
4	4.90	3.90	4.10	4.30	0.53
5	6.00	5.80	6.40	6.07	0.31

Table A4.3. Effect of solution pH on iron (Fe) leaching

pH	C_e (mg.L^{-1})				
	I	II	III	Mean	SD
2	7.15	5.87	6.37	6.46	0.65
3	3.71	3.80	3.25	3.59	0.30
4	1.24	2.03	1.81	1.69	0.41
5	0.95	1.36	1.45	1.25	0.27

Table A4.4. Data of kinetics studies on the adsorption of copper ion (Cu^{2+}) ($V_{solution}$ = 50 mL, $W_{adsorbent}$ = 0.05 g, C_0 = 100 mg.L^{-1}, shaking = 320 rpm, natural pH, time = 1-120 mins and T = 30°C)

Time (mins)	C_e (mg.L^{-1})					q_e (mg.g^{-1})				
	I	II	III	Mean	SD	I	II	III	Mean	SD
10	95.73	98.64	99.74	98.04	2.07	9.59	8.83	6.45	8.29	1.64
20	98.46	99.18	99.70	99.11	0.62	6.18	8.15	6.50	6.94	1.06
30	97.35	99.78	99.77	98.97	1.40	7.56	7.40	6.41	7.12	0.62
40	98.77	99.44	99.98	99.40	0.61	5.79	7.83	6.15	6.59	1.09
50	98.36	99.40	99.41	99.06	0.60	6.30	7.88	6.86	7.01	0.80
60	97.94	100.2	99.53	99.22	1.16	6.83	6.88	6.71	6.81	0.09
120	97.46	98.65	99.36	98.49	0.96	7.43	8.81	6.93	7.72	0.97

Table A4.5. Linear plot of pseudo-first-order kinetics model on the adsorption of copper ion (Cu^{2+})

Time (mins)	Pseudo-first-order			
	ln ($q_e - q_t$)	Slope	Intercept	R^2
0	2.12	-0.008	0.7743	0.3811
10	#NUM!			
20	0.30			
30	0.15			
40	0.53			
50	0.24			
60	0.40			
120	-5.70			
180	-0.30			

Table A4.6. Linear plot of pseudo-second-order kinetics model on the adsorption of copper ion (Cu^{2+})

Time (mins)	Pseudo-second-order			
	t/q_t	Slope	Intercept	R^2
0	#DIV/0!	0.1312	0.3187	0.9926
10	1.21			
20	2.88			
30	4.21			
40	6.07			
50	7.13			
60	8.81			
120	15.54			

Table A4.7. Data of isotherm studies on the adsorption of copper ion (Cu^{2+}) ($V_{solution}$ = 50 mL, $W_{adsorbent}$ = 0.05 g, C_0 = 10-250 mg.L^{-1}, shaking = 320 rpm, natural pH, time = 24 h and T = 30°C)

C_0	C_e (mg.L^{-1})					q_e (mg.g^{-1})				
(mg.L^{-1})	I	II	III	Mean	SD	I	II	III	Mean	SD
10	6.61	6.71	6.51	6.61	0.10	3.90	3.80	4.0	3.90	0.10
25	24.61	25.34	24.21	24.72	0.57	6.71	5.98	7.11	6.60	0.57
50	41.33	41.53	40.99	41.28	0.27	8.71	8.51	9.05	8.76	0.27
75	68.73	69.12	69.02	68.96	0.2	8.90	8.51	8.61	8.67	0.20
100	91.03	91.52	92.63	91.73	0.82	9.37	9.18	8.07	8.87	0.70
150	146.0	146.4	147.7	146.7	0.89	9.80	9.40	8.1	9.10	0.89
200	193.9	194.5	194.3	194.2	0.31	9.30	8.70	8.90	8.97	0.31

Table A4.7. Data of isotherm studies on the adsorption of copper ion (Cu^{2+}) ($V_{solution}$ = 50 mL, $W_{adsorbent}$ = 0.05 g, C_0 = 10-250 mg.L^{-1}, shaking = 320 rpm, natural pH, time = 24 h and T = 30°C) (Continued)

C_0	Log C_e					Log q_e				
(mg.L^{-1})	I	II	III	Mean	SD	I	II	III	Mean	SD
10	0.82	0.83	0.81	0.82	0.01	0.59	0.58	0.60	0.59	0.01
25	1.39	1.40	1.38	1.39	0.01	0.83	0.78	0.85	0.82	0.04
50	1.62	1.62	1.61	1.62	0.00	0.94	0.93	0.96	0.94	0.01
75	1.84	1.84	1.84	1.84	0.00	0.95	0.93	0.94	0.94	0.01
100	1.96	1.96	1.97	1.96	0.00	0.97	0.96	0.91	0.95	0.04
150	2.16	2.17	2.17	2.17	0.00	0.99	0.97	0.91	0.96	0.04
200	2.29	2.29	2.29	2.29	0.00	0.97	0.94	0.95	0.95	0.01

Table A4.8. Data of isotherm studies on the adsorption of copper ion (Cu^{2+}) ($V_{solution}$ = 50 mL, $W_{adsorbent}$ = 0.04 g, C_0 = 10-250 mg.L^{-1}, shaking = 320 rpm, natural pH, time = 24 h and T = 40°C)

C_0	C_e (mg.L^{-1})					q_e (mg.g^{-1})				
(mg.L^{-1})	I	II	III	Mean	SD	I	II	III	Mean	SD
10	5.05	5.07	5.02	5.05	0.03	4.86	4,84	4.89	4.86	0.03
25	17.90	18.40	17.70	18.00	0.36	8.83	8.33	9.03	8.73	0.36
50	43.64	43.71	43.55	43.63	0.08	12.02	11.95	12.11	12.03	0.08
75	63.62	63.32	63.92	63.62	0.30	12.50	12.80	12.20	12.50	0.30
100	87.42	87.60	88.31	87.78	0.47	12.98	12.80	12.09	12.62	0.47
150	141.9	141.5	142.6	142	0.56	13.00	13.40	12.30	12.90	0.56
200	189.8	190.4	190.6	190.3	0.42	13.10	12.50	12.30	12.63	0.42

Table A4.8. Data of isotherm studies on the adsorption of copper ion (Cu^{2+}) ($V_{solution}$ = 50 mL, $W_{adsorbent}$ = 0.04 g, C_0 = 10-250 mg.L^{-1}, shaking = 320 rpm, natural pH, time = 24 h and T = 40°C) (Continued)

C_0	Log C_e					Log q_e				
(mg.L^{-1})	I	II	III	Mean	SD	I	II	III	Mean	SD
10	0.70	0.71	0.70	0.70	0.00	0.69	0.68	0.69	0.69	0.00
25	1.25	1.26	1.25	1.26	0.01	0.95	0.92	0.96	0.94	0.02
50	1.64	1.64	1.64	1.64	0.00	1.08	1.08	1.08	1.08	0.00
75	1.80	1.80	1.81	1.80	0.00	1.10	1.11	1.09	1.10	0.01
100	1.94	1.94	1.95	1.94	0.00	1.11	1.11	1.08	1.10	0.02
150	2.15	2.15	2.15	2.15	0.00	1.11	1.13	1.09	1.11	0.02
200	2.28	2.28	2.28	2.28	0.00	1.11	1.11	1.09	1.10	0.01

Table A4.9. Data of isotherm studies on the adsorption of copper ion (Cu^{2+}) ($V_{solution}$ = 50 mL, $W_{adsorbent}$ = 0.04 g, C_0 = 10-250 mg.L^{-1}, shaking = 320 rpm, natural pH, time = 24 h and T = 50°C)

C_0	C_e (mg.L^{-1})					q_e (mg.g^{-1})				
(mg.L^{-1})	I	II	III	Mean	SD	I	II	III	Mean	SD
10	4.41	4.11	3.81	4.11	0.30	6.31	6.61	6.91	6.61	0.30
25	14.68	15.19	14.48	14.78	0.37	12.75	12.24	12.95	12.65	0.37
50	35.79	36.07	35.70	35.85	0.19	18.21	17.93	18.30	18.15	0.19
75	57.78	57.83	57.75	57.79	0.04	18.93	18.88	18.96	18.92	0.04
100	86.30	85.50	86.94	86.25	0.72	19.20	20.00	18.56	19.25	0.72
150	135.5	135.8	136.6	136.0	0.57	19.80	19.50	18.70	19.33	0.57
200	183.1	183.9	183.8	183.6	0.44	19.60	18.80	18.00	19.10	0.44

Table A4.9. Data of isotherm studies on the adsorption of copper ion (Cu^{2+}) ($V_{solution}$ = 50 mL, $W_{adsorbent}$ = 0.04 g, C_0 = 10-250 $mg.L^{-1}$, shaking = 320 rpm, natural pH, time = 24 h and T = 50°C) (Continued)

C_0	Log C_e					Log q_e				
($mg.L^{-1}$)	I	II	III	Mean	SD	I	II	III	Mean	SD
10	0.64	0.61	0.58	0.61	0.03	0.80	0.82	0.83	0.82	0.02
25	1.17	1.18	1.16	1.17	0.01	1.10	1.09	1.11	1.10	0.01
50	1.55	1.56	1.55	1.55	0.00	1.26	1.25	1.26	1.26	0.00
75	1.76	1.76	1.76	1.76	0.00	1.28	1.28	1.28	1.28	0.00
100	1.94	1.93	1.94	1.94	0.00	1.28	1.30	1.27	1.28	0.02
150	2.13	2.13	21.4	2.13	0.00	1.30	1.29	1.27	1.29	0.01
200	2.26	2.26	2.26	2.26	0.00	1.29	1.27	1.28	1.28	0.01

VITAE

Name Mr. Septian Perwira Yudha

Student ID 6010220021

Educational Attainment

Degree	Name of Institution	Year of Graduation
Bachelor of Science (Chemistry)	Islamic University of Indonesia	2015

Scholarship Awards during Enrolment

1. The Higher Education Research Promotion and The Thailand's Education Hub for Southern Region of ASEAN Countries Project Office of The Higher Education Commission.
2. The PSU Graduate School Financial Support.